Microfluidic Platform to Study the Transport Properties of Model Cell Membranes

Dissertation

zur
Erlangung des Grades
des Doktors der Naturwissenschaften
der Naturwissenschaftlich-Technischen Fakultät
der Universität des Saarlandes

von

Navid Khangholi

Saarbrücken

May 2024

Declaration

I hereby declare that the dissertation entitled "**Microfluidic Platform to Study the Transport Properties of Model Cell Membranes**" which I have submitted for the degree of Doctor of Natural Science at Saarland University is a record of work carried out by me under the supervision of Prof. Dr. Seemann. I further declare that the work reported in this dissertation has not been submitted and will not be submitted, either in part or in full, for the award of any other degree or diploma in this institute or any other institute or university. This is to certify that the printed version is equivalent to the submitted electronic one. I am aware of the fact that a misstatement may have serious legal consequences. I also agree that my thesis can be sent and stored anonymously for plagiarism purposes. I know that my thesis may not be corrected if the declaration is not issued.

Place: Saarbrücken **Navid Khangholi**

Date: 16.05.2024

Tag des Kolloquiums: 22. April 2024

Dekan: Prof. Dr.-Ing. Michael Vielhaber

Mitglieder des Prufungsausschusses

Vorsitzender: Prof. Dr. Peter Orth
Gutacher:
Prof. Dr. Ralf Seemann
Prof. Dr. Albrecht Ott

Akademischer Mitarbeiter: Dr. Alexis Darras

Kurzzusammenfassung

Freistehende Lipid-Doppelschichten ermöglichen es biologische Zellmembranen zu imitieren. Um diese freistehenden Lipid-Doppelschichten in einem Mikrofluidik-Chip herzustellen, werden zwei wässrige Fingern, umgeben von einer öligen lipidgefüllten Phase, in Kontakt gebracht. Die Lipid-Doppelschicht bildet sich an der Berührstelle der lipiddekorierten wässrigen Finger. Im Ramen meiner Untersuchungen wird eine druckkontrollierte Methode zur Manipulation der wässrigen Finger vorgestellt, die es ermöglicht die Lebensdauer der gebildeten Doppelschicht von ursprünglich wenigen Minuten auf Stunden zu verlängern. Durch variierende Druckunterschiede zwischen den wässrigen Fingern lässt sich der Doppelschicht eine gewünschte Krümmung aufprägen. Außerdem kann damit die Oberflächenspannung einer lipiddekorierten Öl-Wasser Grenzfläche, sowie die Membranspannung und die elektrischen Eigenschaften der Doppelschicht in einem einzelnen Experiment bestimmt werden. Die beachtliche Stabilität und Lebensdauer der Lipid-Doppelschicht ermöglicht es darüber hinaus Proteine in diese Doppelschichten einzubinden. In der vorliegenden Arbeit wurde die druckkontrollierte Stabilisierung verwendet, um die Synthese einer GFP markierten Variante von Arch-3 und ihre Integration in eine Doppelschicht unter blauer Lichtanregung zu verfolgen. Elektrophysiologische Eigenschaften von Arch-3 wurden unter grüner Laserbeleuchtung untersucht, wobei eine stufenweise Zunahme des Ionenstroms beobachtet wurde, was auf eine entsprechende Porendynamik hindeuten. Damit ermöglicht diese Methode die Untersuchung modifizierter transmembraner Proteinstrukturen, die aus zellfreien Extrakten durch DNA-Modifikation erzeugt werden, was einen fundamentalen Schritt zur Untersuchung von Signal-Kaskaden mit gekoppelten Rezeptorproteinen darstellt. In einem laufenden Projekt wende ich diese Technik an, um die Fototransduktion von in Lipid-Doppelschichten eingebetteter Schweineretina zu untersuchen. Vorläufige Ergebnisse deuten auf eine erhöhte Transducin-Stromintensität in Dunkelheit hin, gefolgt von einem Abfall bei Lichteinwirkung.

Abstract

Freestanding lipid bilayers are a possibility to mimic biological cell membranes. Forming those free standing bilayer in a microfluidic chip, two aqueous fingers surrounded by an oily lipid-containing phase are brought in contact. At the point where the two lipid decorated fingers touch, a bilayer is eventually formed. My study introduces a pressure-controlled method to manipulate the aqueous fingers, which extends the lifespan of the formed lipid bilayer from minutes to hours. Varying pressures differences across the chip's aqueous fingers further allows for bending the bilayer to a desired curvature that allows to extract monolayer and bilayer tension in as single experiment as well as measuring the electrical properties of the lipid bilayer. The great stability and long lifetime of the lipid bilayer further enabled exploring proteins incorporated into lipid bilayers. In the current thesis, the microfluidic scheme was used to create a GFP-labelled variant of Arch-3 for tracking its synthesis and incorporation into the bilayer under blue light excitation. Electrophysiological characteristics of Arch-3 were explored using a green laser, revealing distinct current steps indicative of pore dynamics. Thus, this approach facilitates the study of modified transmembrane protein constructs, generated from cell-free extracts by DNA modification, which is a foundational step in exploring signalling cascades with coupled receptor proteins. In ongoing work, I apply this technique to study phototransduction in porcine retinas incorporated into lipid bilayers. Preliminary results suggest increased transducin current intensity in dark conditions, followed by a decrease upon light exposure. And confirm the great possibility of this method to explore complex processes in and across bilayer.

Acknowledgment

I am deeply grateful to Prof. Dr. Ralf Seemann for providing me with the opportunity to pursue my Ph.D. under his guidance. I appreciate his support in granting me the freedom to explore my ideas and follow my passion throughout this academic journey. I'm grateful to Prof. Albrecht Ott for the collaboration and the chance to expand my research with his group. Of course without the help of Dr. Marc Finkler this collaboration wouldn't have been possible, and I truly appreciate that. I'd also like to thank all my colleagues, especially my office mates, Shima and Mahsa. Working with both of you made every day a joy.

Above all, my heartfelt thanks go to my entire family, especially to my mom and dad. I can never repay the debt of gratitude I owe them. Hamid, my cousin, without your support and help back in 2013, I could never achieve what I have now and I would never forget that. Behnam and Sepehr, thank you guys for being my best friends for the past 15 years. Shady, my dear sister, you know that when the whole world around me is falling apart, you are the only person who can calm me. Omid, my older brother, you're the true definition of a friend, and you're always there for me no matter what. And last but definitely not least, I would like to thank my lovely wife. There is not a single moment that I do not appreciate having you by my side. I truly believe that I am the luckiest person alive having you.

Table of contents

1. Introduction 11

2. Background 13

2.1. Biological and biomimetic membranes 13

2.1.1. Cellular membrane structure 14

2.1.2. Mechanical properties of cell membranes 15

2.2. Membrane proteins 17

2.2.1. Protein-protein interactions 17

2.2.2. Sensitive membrane proteins 18

2.2.3. Signalling cascade 19

2.2.4. Bacteriarhodopsin and Archaeorhodopsin 20

2.3. Model cell membranes 23

2.3.1. Supported lipid bilayers 23

2.3.2. Vesicles 24

2.3.3. Free standing lipid bilayer 25

2.3.3.1. Droplet-interface bilayers (DIBs) 25

2.3.3.2. Free-standing lipid bilayer in microfluidics 26

3. Materials and Methods 29

3.1. Introduction to Microfluidics 30

3.2. Experimental setup 33

3.3. Patch-clamp 36

3.4. Surface and membrane tension measurement 38

4. Results and Discussions 41

4.1. Surface lipid monolayer tension and lipid bilayer tension 42

4.2. Photoactivation of Arch-3-EGFP 46

4.3. Porcine outer segment photoactivation 49

5. Summary and Outlooks 51

6. References 53

7. List of publications 64

Appendix (I) Simultaneous measurement of surface and bilayer tension in a microfluidic chip 66

Appendix (II) Photoactivation of Cell-Free Expressed Archaerhodopsin-3 in a Model Cell Membrane 74

Appendix (III) An in vitro microfluidic assay for studying G-protein coupled photoreceptor signalling as derived from the retinal photo activated outer segment 83

Appendix (IV) Mechanics of biomimetic free-standing lipid membranes: Insights on lipid chemistry and bilayer elasticity 92

1. Introduction

The plasma membrane is a complex structure of two phospholipid bilayers that surrounds the cell nucleus and is the main barrier between the interior and exterior of a cell. The plasma membrane controls many biological processes such as endocytosis and exocytosis, which prevent or allow the passage of molecules across the plasma membrane [1,2]. Understanding the physical, chemical, and mechanical or physiological properties of the plasma membrane is very important because any disruption in the plasma membrane can lead to dysfunctional biological processes and cause many diseases [3]. Therefore, the plasma membrane is of interest to many biologists and biophysicists. However, the complex plasma membrane is far from fully understood. To further analyse such a complex system and develop methods to study its properties, a simplified model membrane was created. Over the decades, researchers have thus developed numerous methods to replicate and mimic parts of cell membranes [4-6]. The most common techniques are Giant unilamellar vesicles (GUV) and Black lipid bilayers (BLM). These techniques are the closest to the architecture of a real cell in terms of structure and function that can be easily manipulated and visualized under the light microscope [7–10].

In this work, the design of black lipid membranes (BLMs) was adapted to microfluidics, which is the field of science concerned with the manipulation and control of fluids on a small scale. The goal of this work is to first develop a microfluidic device to form and control stable BLMs as biomimetic membranes that allow long observation times. The goal is thus to overcome the limitations of traditional microfluidic techniques, such as short lifetimes or difficulties in measuring electrical properties, by developing a microfluidic scheme to easily fabricate BLMs with superior stability where electrical measurements can be easily implemented. In my work, a microfluidic platform is developed to create free-standing lipid bilayers using hydrostatic pressure system. Using this microfluidic scheme, the surrounding phase of the lipid bilayer can be exchanged without disrupting the lipid bilayer. The usage of a hydrostatic pressure system grants the excellent stability of the lipid bilayer in a way that even the bending of the lipid bilayer can be controlled and manipulated resulting in determination of some mechanical properties of the lipid bilayer such as bilayer tension. This microfluidic system can also allow for electrophysiological measurement and optical

microscopy at the same time. As an application of this microfluidic scheme, taking advantage of the long lifetime of a model cell membrane and the accessibility for electrical measurements, the interaction of Archaeorhodopsin as a photosensitive protein with lipid bilayers has been studied in collaboration with AG Ott, i.e., project C1 within the CRC 1027. The contribution of AG Ott was to produce photosensitive transmembrane proteins using a cell-free expression system. The proteins were incorporated into the lipid bilayer and analysed by optical fluorescence microscopy using blue and green laser illumination. Simultaneously, electrophysiological measurements were used to record the electrical behaviour of the photoactivation of the transmembrane proteins that are incorporated into the lipid bilayer. In summary, it could be demonstrated that artificially made membranes are powerful tools for basic biophysical studies of membrane proteins and can be used in sensing and separation applications.

2. Background

A cell is the basic unit of life. The different structure and elements that constitute it are grouped in separate compartments which interact with each other and form complex networks and molecular machinery on scales ranging from nanometres to micrometres. A cell's role is to produce energy through respiration, initiate metabolic reactions, assist in reproduction, and transport nutrients used in chemical processes within the cell [11]. The cell is composed mainly of water, with 70% of its structure consisting of it. Additionally, proteins make up 18% of the cell, while phospholipids and other lipids make up 5%. The remaining components of the cell include various substances, among which are RNA and DNA, which contain the genetic information necessary for the cell to function properly. The cellular membrane is the barrier between the interior of the cell and the outside environment [12].

2.1. Biological and biomimetic membranes

In mammalian cells, a cellular membrane, also called plasma membrane, is made of a bilayer of mostly phospholipids with embedded proteins, which due to their characteristics, avoid any leakage from inside and outside the cell and vice-versa and therefore maintaining different concentrations of solutes on the two sides (Figure 1) [13]. The plasma membrane performs several functions, such as controlling solute permeability and recognition processes. In addition to their primary functions, membranes also play a crucial role in regulating the movement of ions, water, and other molecules into and out of cells [11-13]. The plasma membrane contains specific biomolecules that act as gatekeepers, controlling the flow of information between cells by receiving chemical or electrical signals and transmitting them to other cells through signal transduction pathways. The intricate nature of the plasma membrane has posed challenges in fully comprehending its mechanism. As a result, biomimetic membranes provide superior opportunities to investigate specific aspects of membrane function and properties, allowing for a better understanding of these complex systems [14].

The term biomimetic membranes denote a membrane that artificially mimics a real cell membrane. Artificial cell models can be defined as those cell-like counterparts bounded by bilayers constructed of either lipid molecules or block copolymers. Compared with complex biological membranes with integrated membrane proteins, these model membranes are simply designed and produced only with

building blocks, which retain key features of bio-membranes, and allow investigations performed in relatively simple environments. However, due to the simplicity of such a model system the interpretation of a result is often clearer. There are many different model membranes, with free-standing lipid bilayers and vesicles being the most commonly used models because they are easy to manipulate and visualize. This section will describe the structure of the biological plasma membrane, including the various types of lipids and membrane proteins present [15]. To better comprehend the intricacies of these systems, artificial models of the cell membrane have been developed that will be presented and discussed in view of their pros and cons.

2.1.1. Cellular membrane structure

The membranes have a thickness of approximately 5-6 nm and are primarily made up of a diverse range of lipids that form the structural basis of the membrane and create a barrier for hydrophilic molecules [14-16]. Specifically, the plasma membrane is comprised of a phospholipid bilayer, consisting of amphiphilic molecules with hydrophilic polar heads and hydrophobic acyl chains (Figure 2a). The lipid bilayer in the plasma membrane is formed due to the properties of these amphiphilic molecules in such a way that the polar parts are directed to the aqueous phase outside and inside the cell [16-17]. The forces that hold these structures together are weak Van der Waals, hydrophobic, hydrogen-bonding, and electrostatic interactions [18]. The function of the plasma membrane is dependent on the predominant lipid compositions present, which can vary in terms of different types of cells. Most membranes contain phospholipid molecules and cholesterols as their major structural components, which impact the membrane's permeability and contribute to its structural functions. Phospholipids consist of two fatty acid chains esterified to a glycerol molecule, with a phosphate group associated with a hydrophilic moiety, such as phosphatidylcholine (PC), phosphatidylethanolamine (PE), phosphatidylserine (PS), phosphatidylinositol (PI), and cardiolipin (Figure 2b). Phospholipid bilayer of the membranes also contain cholesterol which is a small polycyclic amphipathic molecule that its polar section is restricted to a single hydroxyl (OH) group and its apolar section has an asymmetric structure (Figure 2c) [11,12,16,17]. Cholesterol cannot form a membrane by itself but

inserts into a bilayer of phospholipids with its hydroxyl group close to the head group of phospholipids. Other lipids such as sphingolipids and glycolipids containing sugars are responsible for protecting the membrane from extreme conditions, i.e., low pH and degrading enzymes [16,17,19].

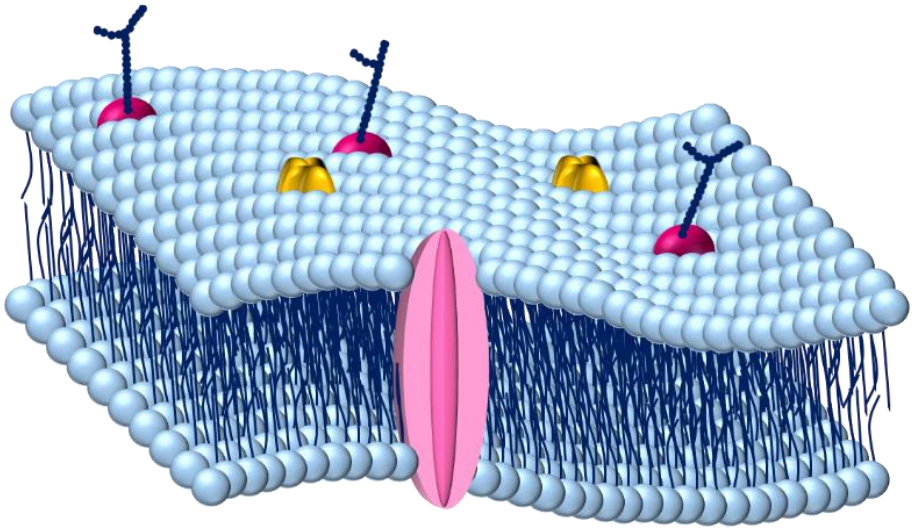

Figure 1. Sketch of a plasma membrane. The major components of the plasma membrane are lipids (phospholipids and cholesterol), proteins, and carbohydrate groups attached to some of the lipids and proteins.

2.1.2. Mechanical properties of cell membranes

The mechanical properties of cellular membranes are determined through different types of phospholipids in the membrane which displays various material characteristics that are influenced by the phospholipids and how they respond to physical factors such as temperature, pressure, pH, or surface tension tension [20-23]. A significant temperature increase of lipid bilayers leads to an energetic reorganization of lipids by chain melting, i.e., a phase transition from gel to liquid crystal caused by a huge entropic change [24]. Each phospholipid mixture exhibits different thermotropic phase behaviour and intrinsic bending and compressibility [25]. Moreover, the temperature for the phase transition can be lowered with increasing surface tension at constant pressure, which can be explained by thermodynamics. This phenomenon is known as the Gibbs-Thomson effect, and it is due to the increase in the free energy of small lipid aggregates at the interface [26]. As the packing density of the lipids increases, resulting in a more ordered

membrane structure, and potentially increasing surface tension, the temperature required to achieve a higher degree of order in the lipid tails is lowered. This phenomenon highlights the significance of surface tension in cell membranes, as it grants the lipid bilayer of the membrane the necessary rigidity and stability [27]. While the lipid bilayer determines the basic structure of plasma membranes, most of the cellular and physiological processes are carried out by membrane proteins [28].

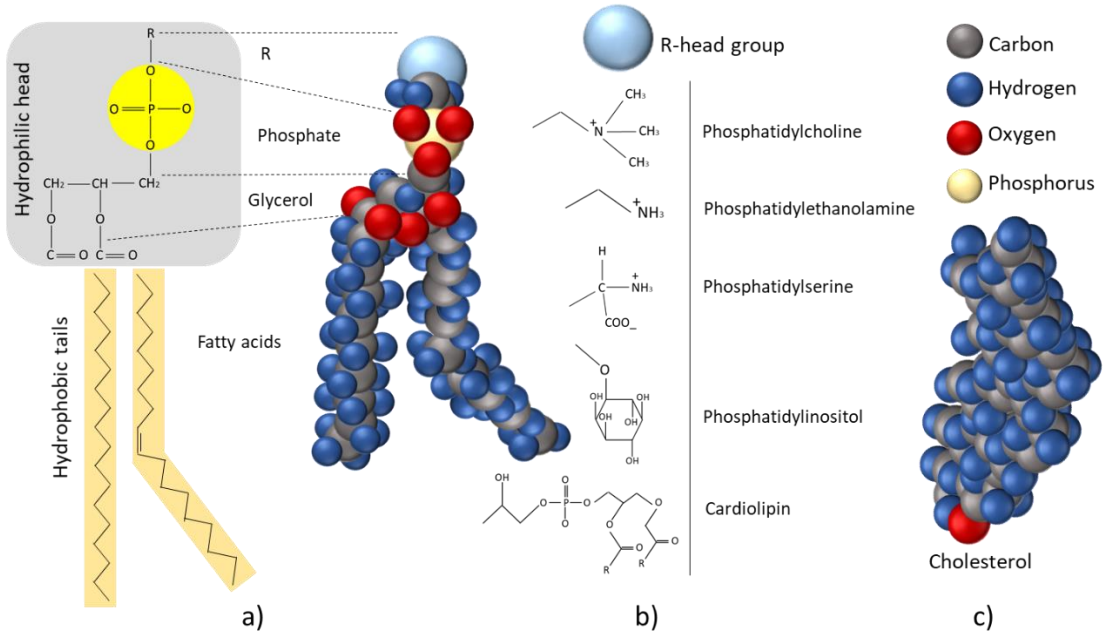

Figure 2. Molecular structure of phospholipids a) A phospholipid is a lipid composed of glycerol, two fatty acid tails, and a phosphate-linked head group. b) lipid head group types: phosphatidylcholine (PC), phosphatidylethanolamine (PE), phosphatidylserine (PS), phosphatidylinositol (PI), and cardiolipin. c) Molecular structure of cholesterol which is one of several types of lipids that play an important role in the cell membrane.

2.2. Membrane proteins

The plasma membrane is usually composed of 30% membrane proteins, either incorporated into the membrane or bound only to the surface of the membrane on one or both sides. Membrane proteins are classified based on their interaction with the plasma membrane [29,30]. They are divided into two major groups: Peripheral and Integral proteins. Peripheral membrane proteins are those that temporarily adhere to the biological membrane through weak interactions such as electrostatic or hydrogen bonding with lipid head groups or other membrane proteins. Detachment of these proteins from membrane surface can be done easily by mild treatment such as changes in pH or ionic strength [31,32]. This property is in contrast to integral membrane proteins, which penetrate the phospholipid bilayer of the plasma membrane and permanently attach to it via hydrophobic interactions. For this reason, detergents can be used to remove integral proteins that nearly destroy the hydrophobic interaction of the entire lipid bilayer [33]. Transmembrane proteins are a type of integral proteins that span the entire biological membrane. These proteins typically have hydrophobic regions that interact with the hydrophobic fatty acid chains of the lipid bilayer, anchoring the protein in place. A transmembrane protein may also have hydrophilic regions that interact with the aqueous environment on either side of the membrane. These proteins play key roles in numerous biological processes, such as cell signalling and the transport of ions and nutrients [34-37]. Membrane proteins generally can act as receptors, transporters, and channels, or converters (Figure 3a). They have numerous functionalities and responsibilities, such as cell developments, cell-cell interactions, energy conversions, neural transmissions, and muscle contractions that can be conducted via protein-protein interaction [29,30].

2.2.1. Protein-protein interactions

Protein-protein interactions involve the binding of two or more membrane protein molecules through specific regions on their surfaces, known as binding sites [38]. Membrane proteins can interact with other proteins within the membrane, as well as with proteins outside of the membrane [39]. One possibility of protein-protein interactions is the formation of complexes. In this process, two or more proteins bind together to form a larger, multi-subunit complex. The individual proteins within the complex often work together to carry out specific functions, such as

enzymatic reactions or molecular signalling [40]. Another way that protein-protein interactions occur is through allosteric regulation. In this process, binding of one protein to another causes a conformational change in the target protein, leading to a change in its activity or function. Allosteric regulation is often used in signalling pathways to control the activity of enzymes and other proteins [41,42]. Protein-protein interactions can also occur through the formation of transient complexes. In this process, proteins interact with each other for a short period of time, allowing them to carry out specific functions before dissociating. Transient interactions are often used in signalling pathways to amplify signals and to ensure that the correct proteins are activated in response to specific stimuli [43].

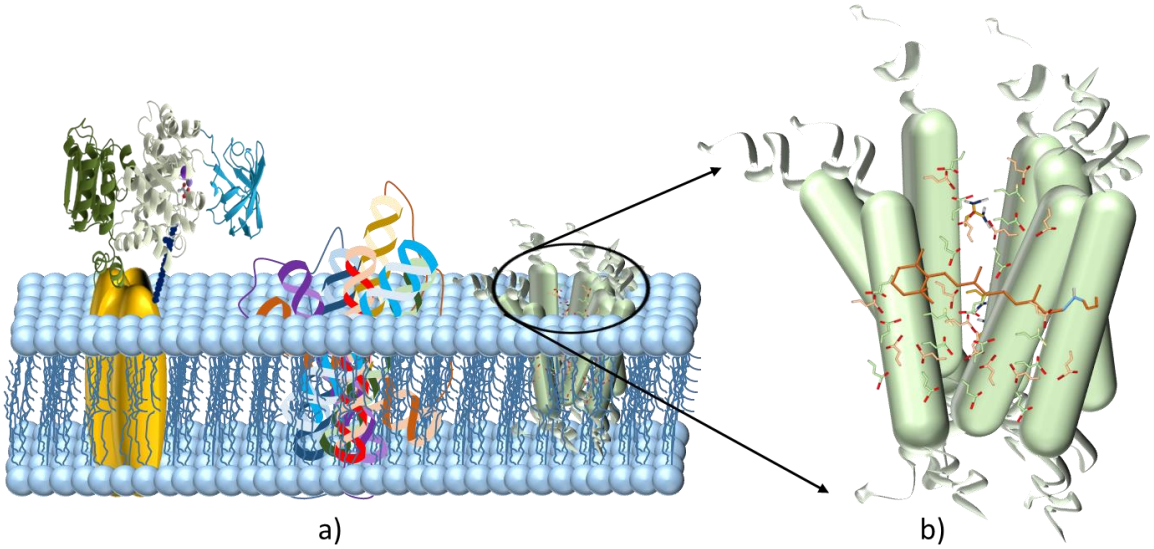

Figure 3. Schematic representation of membrane proteins incorporated into a cell membrane. a) Peripheral and integral membrane proteins: Peripheral proteins are proteins that bind temporarily to the membrane through weak interactions on outer side of the membrane as shown above. Integral proteins, on the other hand, are those that penetrate the cell membrane and bind permanently to the membrane through strong interactions. b) G protein-coupled receptors are integral membrane proteins that are inserted in the cell membrane and transmit signals from the extracellular region to the interior of the cell membrane.

2.2.2. Sensitive membrane proteins

Membrane proteins, in addition to their role in protein-protein interactions, can also play a key role in membrane structure and function [34]. They can act as channels or transporters, allowing specific molecules to pass through the membrane [44]. They can also act as enzymes, catalysing biochemical reactions

within the membrane, and they can act as receptors that transmit signals between the inside and outside of the cell [45,46]. Some of these membrane proteins are considered as sensitive proteins that undergo changes in their properties or functions in response to certain stimuli such as voltage, chemicals or light. The voltage-gated ion channel proteins are sensitive proteins that respond to changes in the electrical potential across the membrane to open or close and allow ions to flow across the membrane [47-51]. Another type of sensitive membrane proteins is the chemically sensitive protein which is include G-protein coupled receptors (GPCR) that involved in signalling pathways that regulate a wide range of cellular processes, including hormone and neurotransmitter signalling (Figure 3b). These receptors respond to ligands such as hormones or neurotransmitters, which bind to the receptor and cause a conformational change that activates intracellular signalling pathways [52]. Another type of sensitive membrane protein is the light-sensitive rhodopsin family of proteins, which includes opsins found in the retina of the eye. Upon illumination these proteins change their conformation and initiate a signalling cascade that leads to the perception of light [53-55].

2.2.3. Signalling cascade

Signalling cascade is a type of intracellular signalling pathway that involves a series of biochemical reactions, typically triggered by the binding of a ligand to a cell surface receptor. The ligand binding to the receptor induces a conformational change that activates the receptor, leading to the recruitment and activation of downstream signalling proteins [56]. For example, in GPCR signalling pathways, the cascade signalling is initiated by a light-sensitive membrane protein such as rhodopsin which is the G-protein coupled receptor [57]. The rhodopsin has a unique chromophore molecule called retinal. The retinal is covalently attached to a lysine residue in the protein. When retinal absorbs a photon of light, it undergoes a conformational change activating the rhodopsin. The conformational change in the rhodopsin-receptor causes an opening in the molecule for the G-protein known as transducin, which has three subunits: alpha, beta, and gamma, to bind to the rhodopsin. The binding of the transducin to the rhodopsin cause the alpha subunit of the transducin to exchange its GDP molecule for a GTP molecule, leading to the dissociation of the alpha subunit from the beta-gamma subunits. The alpha subunit can then activate a downstream effector protein, such as an enzyme called

phosphodiesterase (PDE), which degrade the hydrolysis of cyclic GMP (cGMP) to GMP (Figure 4). The hyperpolarization of the photoreceptor cell leads to a decrease in neurotransmitter release from the cell, which is then transmitted to the downstream neurons of the visual pathway. This ultimately leads to the perception of light by the brain. This mechanism of light sensitive proteins such as Rhodopsin as GPCR is essential for vision and other light-dependent physiological processes in many organisms [58,59].

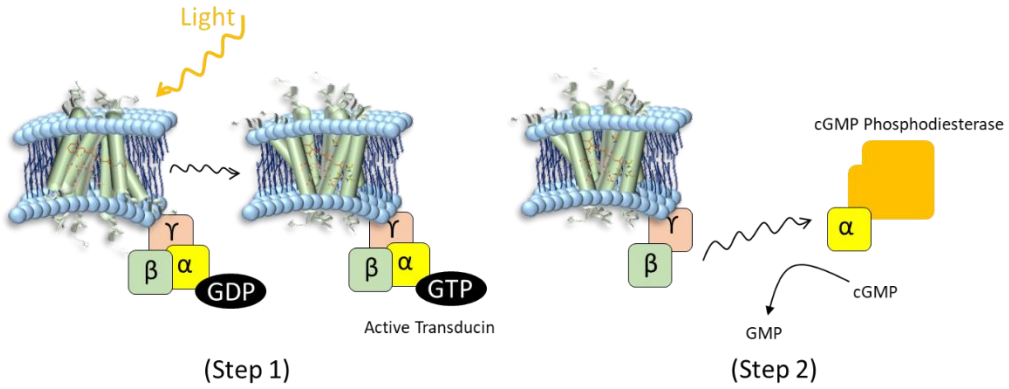

Figure 4. Schematic illustration of GPCR photoactivation.

2.2.4. Bacteriarhodopsin and Archaeorhodopsin

There are different types of rhodopsin proteins apart from human and bovine rhodopsin known as the receptor for G-protein that can be found in various organism having unique properties. For instance, bacteriarhodopsin is a rhodopsin found in Archaea specifically in a species of halobacteria [60]. Bacteriarhodopsin can function as a light-driven proton pump [61]. It has a similar structure to other rhodopsins as well as human and bovine rhodopsin with a retinal chromophore covalently bound to the protein [62]. Bacteriarhodopsin is the only protein in the purple membrane covering 80 % of the total membrane surface. The purple colour of the bacteriorhodopsin-containing membrane is due to the presence of the protein, while the ability to absorb light is due to the retinal chromophore that is covalently bound to the protein through a Schiff base linkage [60].

When bacteriorhodopsin absorbs a photon of light, the retinal chromophore undergoes an isomerization to the 13-cis retinal configuration. This triggers a series of events, including proton transfer from the Schiff base to an acceptor residue (Asp85) located on the extracellular side of the protein. The Schiff base

then switches its orientation to face Asp96, a donor residue located on the intracellular side of the proton channel within the protein. Asp96 accepts a proton from the cytoplasm and transfers it to the Schiff base, causing the retinal chromophore to isomerize back to its all-trans state. The photocycle returns bacteriorhodopsin back to its ground state, with the release of a proton from the proton-release complex into the extracellular environment. This completes the proton pumping process and sets the stage for another round of proton pumping upon light absorption [63,64]. Archaeorhodopsin is another microbial rhodopsin that has the similar structure to bacteriarhodopsin functioning in capturing light energy [65,66]. Like bacteriorhodopsin, archaeorhodopsin undergoes a photocycle when it absorbs light. The retinal chromophore undergoes isomerization to the all-trans retinal configuration, which triggers a conformational change leading to the transfer of a proton from an acidic amino acid residue (Asp85) to the Schiff base linkage between the retinal and a lysine residue [67]. This transfer results in the translocation of a chloride ion across the cell membrane from the extracellular to the cytoplasmic side. After the chloride ion is released into the cytoplasm, a conformational change occurs, returning the protein to its initial state, ready for another photocycle [68]. Despite the bacteriarhosopsin and archaeorhodopsin, the human and bovine rhodopsin is not capable of functioning as proton pump. Instead, they are only involved in the detection of light and the transduction signalling pathways [69].

Understanding the behaviour of rhodopsin proteins and their role in GPCR signalling is very crucial in many areas. It provides valuable information about how GPCR transmit signals to the cells. It helps to comprehend the basic and fundamental mechanism of vision and sensory perception [52-59]. Studying the structure and behaviour of rhodopsin and other GPCRs can provide insights into designing drugs that specifically target these receptors, potentially leading to new treatments for various diseases [70]. However, in real cellular membrane in vivo, the understanding of the mechanism of the GPCR signalling can be challenging and may involve certain limitations that could affect the accuracy and relevance of the obtained results. The main limitation is the complexity of in vivo systems, which can make it difficult to study and require many characterisation techniques such as fluorescence, EPR and NMR spectroscopy to interpret the data [71].

Therefore, in vitro studies can provide a more controlled and predictable environment, allowing for a better understanding of the molecular mechanisms underlying the functions of membrane proteins. Additionally, in vitro studies can use purified synthesized proteins, eliminating the complexity and variability of whole cell systems. Therefore, scientist have been developing biomimetic membrane over the last few decades, aiming at modelling cellular membranes for simulating the signals occurring across the membrane [72-74].

2.3. Model cell membranes

Artificial cell models have proven to be an important tool for studying various membrane properties, e.g., lipid structures and functions, processes in the membrane, curvature effect, ion channels, and interaction of lipids with drugs or nanoparticles, as well as for studying the membrane activity of various natural or synthetic compounds such as peptides [72-75]. In contrast to complex biological membranes with integrated membrane proteins, these artificial cell models are simple structured and consist only of building blocks that retain the main features of the plasma membrane and allow studies in relatively simple environments, and thus enable a clear interpretation of the results [75,76]. The application of model cell membranes is determined by the format of the membranes, which generally include bilayers in the form of vesicles, supported lipid bilayer or free-standing lipid bilayer [77].

2.3.1. Supported lipid bilayers

Supported lipid bilayers (SLBs) are stable flat lipid bilayers supported on a solid substrate such as glass or silicon and are usually formed by adsorption and fusion of vesicles (Figure 5a). In such an artificial membrane system, the hydrophilic head groups of the lower lipid monolayer face the substrate, while the hydrophobic acyl chains are in contact with the lipid tails of the upper monolayer. Due to the structure of SLBs, the top surface of the membrane is exposed to the aqueous solution, so SLBs can not only be used to characterize the chemical interactions between two monolayers, but also provide various tools for surface-specific analyses. SLBs are also capable of preserving the asymmetric aspect of a biological membrane [78-80]. They are used to predict the phase behaviour and organization of molecules in the plasma membrane. Characterization and visualization of SLM membranes is as simple as it is compatible with surface sensing techniques such as atomic force microscopy (AFM), secondary ion mass spectroscopy (SIMS), or X-ray and fluorescence microscopy [81]. However, one of the main drawbacks of the SLB model system is the proximity of the bilayer to the substrate, which directly affects membrane mobility or protein incorporation, making it difficult to characterize the functions of target membrane proteins and all kinetic aspects.

2.3.2. Vesicles

Lipid vesicles or liposomes are simple model systems of a closed cellular membrane for studying membrane phase behaviour and membrane processes, including membrane fusion and molecular recognition. Vesicles are fluid-filled spherical architectures formed spontaneously by self-assembly of phospholipids [82]. Initially, vesicles have been introduced using gentle hydration method discovered by Bangham in 1964. In this method, the phospholipids are first dissolved in an organic solvent and then dried by evaporating the solvent under vacuum until lipid films form on the container surface. After the lipids have dried at temperatures above the phase transition, the dried phospholipid films are hydrated by adding an aqueous solution [83]. This standard method to produce vesicles has limitations in terms of producing vesicles with high encapsulation efficiency and controlling the lamellarity properties. Lamellarity property refers to the organization of lipid layers in vesicles or liposomes. It describes the way in which the layers are stacked together and the uniformity of their size and shape. Unilamellar vesicles consist of a single spherical lipid bilayer are formed by sonication of the multilamellar vesicle solution in a classical ultrasound device. However, this method produces a broad range of size distributions, which is from 10 nm to 1 μm considered as small and large unilamellar vesicles (SUV and LUV) and extrusion into narrow size distribution is demanded [84]. Larger vesicles so-called giant vesicles (GUV) between 1 μm to 1 mm are the closest in size to actual cells and can be used as a model cell membrane (Figure 5b). GUVs can easily be visualised and characterised using AFM or optical (fluorescent or confocal) microscopy. GUVs can either be formed using hydrating a dried lipid film or electro-formation method. Lipid vesicles are not only considered to be very powerful artificial membranes for biological studies but can also encapsulate biomolecules to transport and incorporate them into the bilayer [85,86]. However, they have drawbacks when it comes to electrophysiological measurements of lipid bilayers. To characterize the electrical properties of the lipid bilayer using vesicles, two electrodes must be inserted inside and outside a single vesicle after a vesicle is detected, which can be challenging. It would be even more difficult to immobilize the vesicles for optical observation and simultaneously perform electrophysiological measurements.

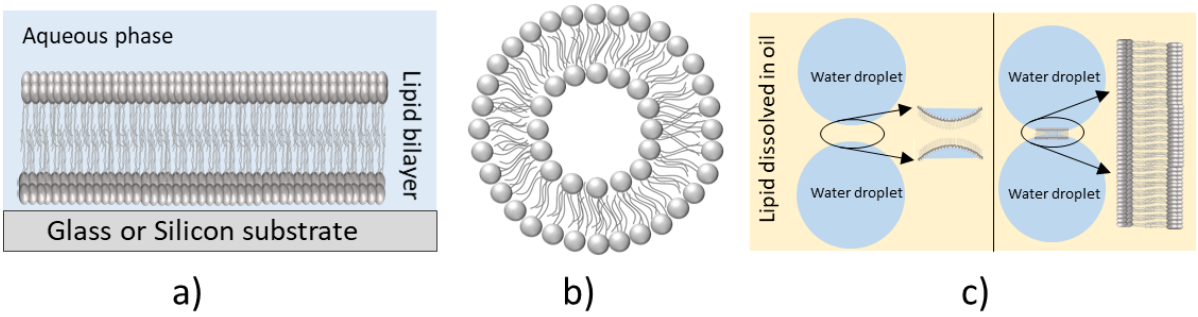

Figure 5. Conceptual illustration of a) a supported planar lipid bilayer (SLB) b) GUVs as model cell membranes c) Droplet interface bilayers (DIBs).

2.3.3. Free standing lipid bilayer

Black lipid membrane (BLM), known as free-standing lipid bilayers, is actually the first biomimetic membrane that can be used for electrochemistry measurements. The main advantage of free-standing lipid bilayers over supported lipid bilayers and vesicles is the fact that both sides of the lipid bilayer can be under control in terms of changing the aqueous phase [87,88]. However, the challenge in this technique is the formation of the free-standing lipid bilayer due to its lack of great stability. Recent studies have proven that using two water droplets in an oily phase containing lipids can lead to formation of a large area free-standing lipid bilayer [89], which are called DIBs.

2.3.3.1. Droplet-interface bilayers (DIBs)

DIBs are other artificial model membranes formed by assembling aqueous droplets covered by a lipid monolayer immersed in an oil-lipid mixture. When two lipid coated droplets carefully approach each other, the two lipid monolayers arrange at the interface of the droplets to form a robust bilayer (Figure 5c) [90-92]. The lipid-out technique uses lipids dissolved in the oil phase, while the lipid-in method involves lipid vesicles entrapped in the internal aqueous phase. Most often, the lipid-in approach is used to form asymmetric lipid bilayers. In the lipid-in approach, when two vesicles with different types of lipid composition in separate water droplets are in contact, two lipid monolayers with different composition are created resulting in forming an asymmetric lipid bilayer [95]. The DIB technique offers a number of advantages, such as its high stability, resulting in an extended

lifetime of days to weeks, and easy-to-control electrical measurements by inserting hydrophilic electrodes into the droplets to measure capacitance and to record ion currents passing ion channels [93,94]. In general, there are two different approaches for the formation of DIB model membranes, lipid-in and lipid-out DIB. This depends on how the phospholipids are assembled into monolayers at the water-oil interfaces.

The DIB technique has been employed for incorporating various membrane proteins, for electrophysiological characterization [96]. With the continuous electrical measurement on the lipid bilayer, DIBs can have a lifetime ranging from days to weeks, making them a potential method as biomimetic model cell membrane for measuring the electrical properties of membrane proteins. Thus, the DIB technique was considered in conjunction with in vitro transcription and translation to generate cell-free expressed membrane proteins inside the droplets [97]. However, the traditional DIBs technology also comprises some limitations. In general, optical, and mechanical characterisation is difficult due to the stability of the droplets in the solvent. Some recent studies have shown that using 3D printing structures of droplets connected by interface lipid bilayers can enhance the precision and stabilities of the droplets to be immobilised [98,99], however changing the surrounding phase of the lipid bilayer is not feasible using DIB technique for membrane analysis which is the main drawback of the DIB technique. In order to minimize the impact of poor electrical background noise in DIB technique and achieve greater optical tracking in lipid bilayer formation, another strategy should be considered for the formation of a free-standing lipid bilayer. Recent studies have shown that a microfluidic system combined with DIB technique is a powerful tool for forming a free-standing lipid bilayer. This method, as a subcategory, overcomes the drawbacks of some previous techniques and provides excellent stability and significantly reduces background noise for electrical measurements [99, 100].

2.3.3.2. Free-standing lipid bilayer in microfluidics

To form lipid bilayer in microfluidic, first the cross-geometry channels in microfluidics consisting of four intersecting channels were introduced in 2006 by Funakoshi et al. [101] to create a free-standing lipid bilayer. Initially, the channels

in the microfluidic device were filled with a mixture of oil and lipids for one hour. Subsequently, aqueous fingers were injected using syringe pumps and the oil water interface decorates with a lipid monolayer. When the two aqueous phases are gently brought in contact at the cross section, the lipid monolayers at the water oil interfaces form a free-standing lipid bilayer. With this geometry, lipid bilayers with diameters of up to 500 µm could be produced in a highly controllable manner. This technique allows for a decent formation stability and electrical measurement (Figure 6a) [101]. The drawbacks of this techniques is that both sides of the free-standing lipid bilayer remain immobile which prevents for changing or adding any compounds to the aqueous phase. To overcome this issue and be able to change the surrounding phase of the free-standing lipid bilayer, the parallel microchannel shape was designed. As shown in the Figure 6b, this technique not only allows for the great stability, it allows for the exchanging the surrounding aqueous phase of the free-standing lipid bilayer, which subsequently allows for inserting different molecules such as proteins, antibiotics, vesicles and so on at different stages of an experiment. This microfluidic geometry allows to explore the interaction of a plethora of molecules with free-standing lipid bilayer, using both optical and electrical monitored [102].

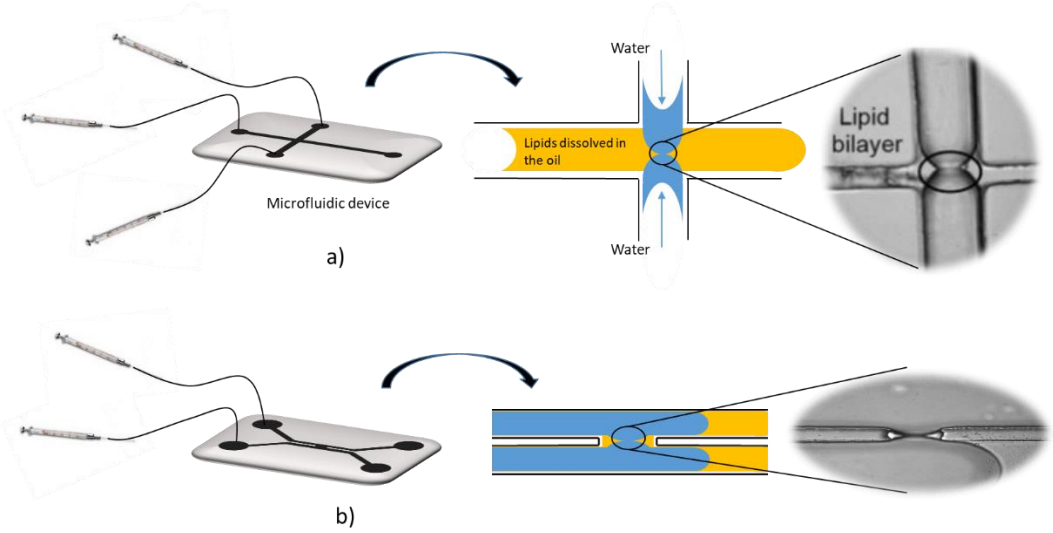

Figure 6. Schematic representation of the microfluidic system for the formation of a free-standing lipid bilayer. In this technique, the objective lens of the microscope is directed to the side view of the formed lipid bilayer, which is seen as a black line. a) The lipid bilayer forms when two aqueous fingers separated by mixture of oil and lipids gently contact each other at the intersection of the cross channels. b) The lipid bilayer forms when aqueous phase in the parallel channels meet at the intersection separated by mixture of oil and lipids.

3. Materials and Methods

This chapter is divided into three main parts. The first part discusses the microfluidics, the device fabrications, and the experimental running setup for lipid bilayer formation. The second part describes the use of patch-clamp technique for the electrophysiological measurement of the lipid bilayer. Lastly, the third part explains how surface and bilayer tension can be driven from curvature of the lipid bilayer using hydrostatic pressure system.

Materials

DOPC (1,2-dioleoyl-sn-glycero-3-phosphocholine), DPhPC (1,2-diphytanoyl-sn-glycero-3-phosphocholine), and Monoolein (1-Oleoyl-rac-glycerol) were used as test lipids. DOPC is one of the most common lipids in the human cell membrane. DPhPC is a less biological relevant lipid, but known to produce a very stable bilayer. DOPC and DPhPC lipids were purchased from Avanti Polar Lipids, and Monoolein was purchased from Sigma Aldrich. To prepare oil–lipid solutions, 5 mg of lipids were dissolved in 1 mL of pure squalene oil (Sigma-Aldrich, St. Louis, Missouri, USA) at 45 °C while undergoing continuous stirring for 3 h.

The Archaeorhodopsin-3-EGFP protein is produced using a cell-free expression system. Specifically, the commercially available E. coli T7 S30 Extract System for Circular DNA (Promega, Madison, Wisconsin, USA) served as the chosen expression system. The Plasmid used, WT Arch-3-EGFP in pET28b, is obtained from Adgene. The expression is performed in the presence of vesicles. The vesicles (SUV) were produced by adding 1 mg of DOPC and DPhPC to the NaCl buffer in two different vials and sonicate three times, applying the continuous cycle of 4 s pulse and 4 s break for 4 min, and 2 min rest in between [112]. The solution containing SUVs is mixed with 400 µl of S30 Premix without Amino Acids, 50 µL of Amino Acid Mixture Minus Cysteine at 1 mM, 50 µL of Amino Acid Mixture Minus Leucine at 1 mM and 500 µL of ultrapure water. Expression reactions were conducted as follows: The components of the cell-free expression system are combined to create a "mastermix" consisting of 40 µL S30 Premix without Amino Acids, 5 µL of Amino Acid Mixture Minus Cysteine at 1 mM, 5 µL of Amino Acid Mixture Minus Leucine at 1 mM, and 30 µL T7 S30 Extract System for Circular DNA. To this mastermix, 10 nM of plasmid DNA is added, and the

mixture is filled up with the vesicle solution to reach a total reaction volume of 100 µL. The expression reaction is subsequently incubated at 37 °C for 48 hours. It's important to note that each reaction solution is directly introduced into the microfluidic device post-expression and could not be utilized beyond 24 hours [121].

For the production of porcine photoreceptor outer segment (POS) for the project of photoactivation of GPCR signalling cascade, 80 fresh pig eyes were obtained from slaughter and are kept in the dark. The extraction of the porcine outer segment from retina cells in the pig eyes is quite lengthy and was conducted strictly following the protocol published in [122]. The end result provided the POS aliquoting with and without labelling.

3.1. Introduction to Microfluidics

Microfluidics is the science of manipulating and controlling fluids with small volumes of less than one picoliter (10^{-12} L) geometrically confined in chips of one microliter (10^{-6} L) that are composed of networks of channels with dimensions ranging from tens to hundreds of micrometers. In the microworld, the laminar behaviour of flows and diffusion become dominant, and the miniaturization of channel dimensions provides the opportunity to manipulate and control fluids much more precisely than in the macroworld. The concept of microfluidics first emerged in the 1970s (Terrry et al.) when he introduced a gas chromatograph based on etched microchannels in a silicon wafer [103] In the 1990s (Manz et al.), the application of microfluidic systems in molecular analysis evolved tremendously [104]. The benefits of using microfluidics for applications such as cell culturing and bioprinting in biology, emulsions and formulations in cosmetics, drug discovery and diagnosis in pharmaceuticals, flow synthesis and screening assays in chemistry, and micromodelling to improve petroleum production are innumerable [105,106]. Down-scaling to micro range in microfluidic has thus enabled many researchers to consume less samples and control fluids much more precisely compared to larger scales. In micro scales, flows become laminar which allows for more precise environment and control over shear forces. The small volume provides the ability to analyse and characterize models much faster and with higher sensitivity [107]. Conventional microfluidic systems were all made of silicon and glass, which are produced in the MEMS industry [108]. However, as microfluidic techniques evolved, a new concept called a lap-on-chip system using

soft lithography was introduced. This technique allows a microstructure to be replicated from a master mold into silicon rubber or polymer surfaces produced in bio-chemical laboratories. In this work PDMS (Polydimethylsiloxane) was used as a polymer for the soft lithography due to its fast and cheap fabrication, and very low background fluorescence [109,110].

Device fabrication

For the fabrication of a master mold structure, I used standard photolithography technique that is replicated in PDMS for form the microfluidic device. Before conducting photolithography, first a photomask was fabricated. For that, the mask design is drawn in 2D using AutoCAD software and printed on an opaque polyester film with transparent structures. To produce a master consisting of a photoresist structure on top of a silicon wafer by photolithography, the silicon wafers are rinsed with isopropanol and acetone to remove possible contaminants. In my technique, a UV-light photosensitive resist is used and spin coated on a cleaned silicon wafer. The thickness of the applied photoresist is determined by the viscosity of the photoresist and the acceleration, spinning speed and spinning time applied to the photoresist, respectively to the silicon wafer. The used SU8-100 negative photoresist was used to achieve homogeneous resist thicknesses of about 100 µm height; the used parameters are shown in the table I. After spin coating, the silicon wafer is placed on a hot plate to soft bake at 65°C and 95°C (table (I)) (pre-exposure baking). The heat ensures that the photoresist dries out and adheres better to the surface. Immediately after soft baking, the photomask is placed on the resist coating of the silicon wafer and placed under the UV-exposure machine. After exposure through the transparency mask, the wafer is again placed on a hot plate for post-baking at 65°C and 95°C to increase the degree of cross-linking (Table (I)). Finally, the wafer is rinsed with SU8 developer (1-methoxy-2- propyl acetate) for 5 minutes. The SU8 remaining on the silicon wafer is the one that was exposed to the light and was cross linked, which is the master used to mold the microfluidic chip by soft lithography. For fabricating the microfluidic device using soft-lithography, the commercially available PDMS rubber kid Sylgard 184 (Dow Corning) was used. After mixing the PDMS molecules and the curing agent in a ration 10:1, the PDMS mixture is allowed to stand at room temperature for about 15 minutes to remove air bubbles. Then, the PDMS mixture is poured onto the

master that is placed in a Petri dish. The Petri dish with the PDMS mixture is placed in an oven at 65 °C for two and a half hours to crosslink and solidify the PDMS mixture. After cooling, the PDMS is removed from the master. The microfluidic channels patterned on the exfoliated PDMS have a height of 100 µm. The PDMS is then attached to a glass substrate by plasma bonding and then baked at a high temperature (100° C) to create a strong bond between PDMS and glass substrate. This process allows for the creation of a stable, leak-free seal between the PDMS and the glass, besides it ensures restoring the hydrophobicity of the PDMS. The same protocol was used in all experiments in this work for fabricating the microfluidic chip (Figure 7b).

Table (1). Microfabrication parameters in cleanroom for the SU8-100 negative photoresist. The parameters were adjusted to achieve 100 µm height [111].

Channel height	µm	80	120
Spin velocity	RPM	2000	1700
Pre-bake (65° C)	Min	10	13
Pre-bake (95° C)	Min	30	37
Exposure	Sec	30	30
Post-bake (65° C)	Min	1	1
Post-bake (95° C)	Min	5	7
Development	Min	5	8
Clean room temperature	25° C		

The microfluidic geometry on the photomask is designed as a transparent X-shape with two side-by-side channels that are both 300 µm wide and that meet at an intersection with an extension of 150 µm (Figure 7a).

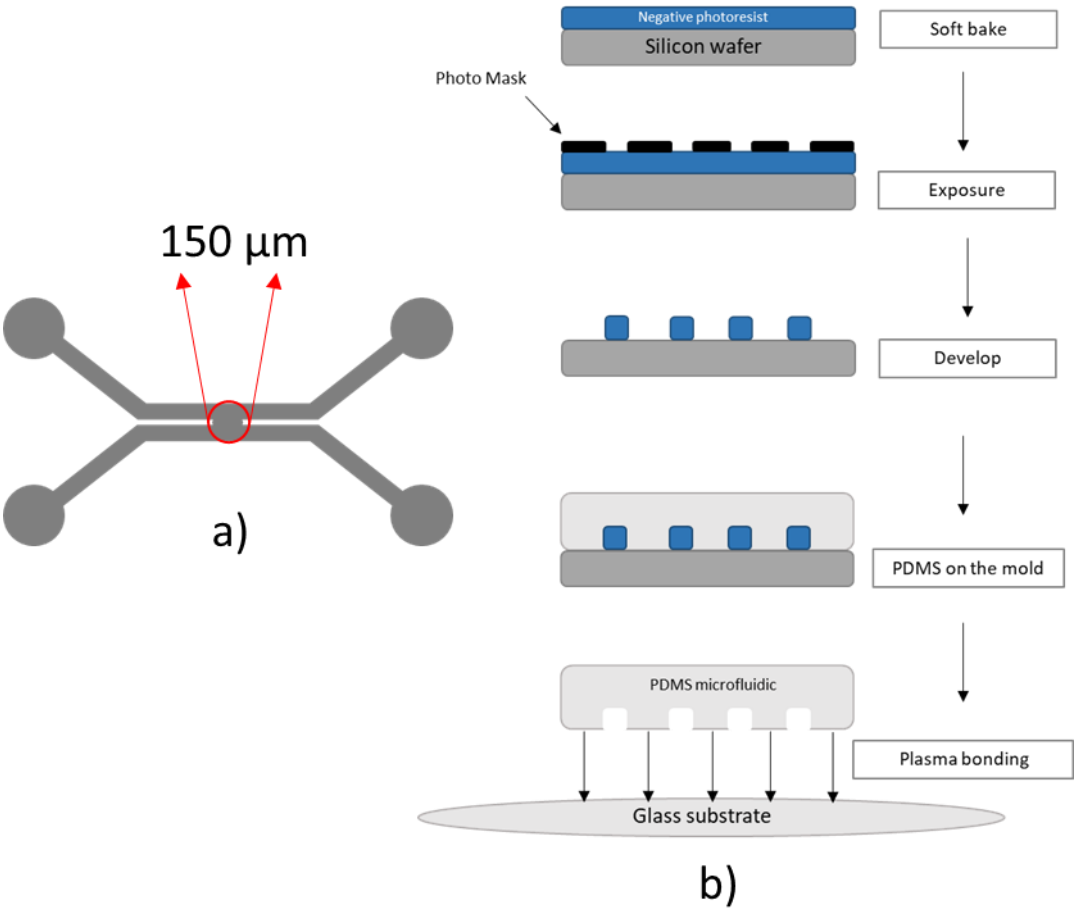

Figure 7. a) The X geometry of the microfluidic structure with 2 side-by-side channels having 300 µm channel width and an intersection space with 150 µm. b) The cartoon de of photolithography process. Microfabrication process of an SU-8 master for soft lithography. A silicon wafer is carefully cleaned with solvents to remove dust particles and the photoresist is coated on the silicon wafer using spin coating. The coated wafer is irradiated with UV light through a photomask, and finally the non-crosslinked photoresist is removed from the wafer, leaving only the designed microchannel.

3.2. Experimental setup

Generally, the formation of bilayers in microfluidic devices can be achieved through either volumetric control or pressure control. Bilayers can be easily formed using volumetric control, which, in our laboratory, is facilitated by computer-controlled syringe pumps. These pumps are well-suited for delivering constant flow rates, but they have limitations in stopping flow as needed to effectively form and stabilize a free-standing phospholipid bilayer. This is due to the occurrence of a persistent 'creeping flow' caused by dilation of the tubing system once a certain volume of fluid is injected. Consequently, producing long-

lasting bilayers remains challenging due to the restricted flow control offered by the currently utilized volumetric control method. In contrast, a pressure pulse propagates at the speed of sound, allowing for an immediate stoppage of flow in a pressure-controlled system.

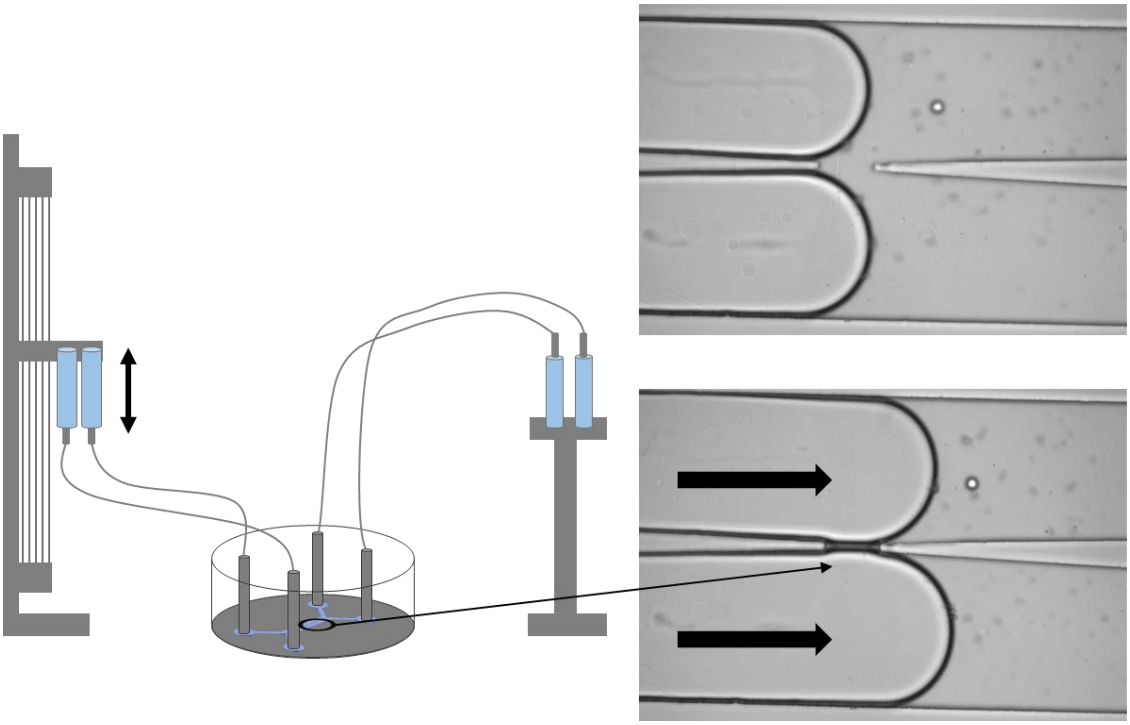

Figure 8. Schematic of hydrostatic pressure control system. The two inlets of the microfluidic device are connected to the two hydrostatic reservoir that are fixed on a motorized stage, and the outlets are connected to two reservoirs at a fixed height position. By applying a pressure difference which is the difference of the inlets and outlets, the aqueous fingers are pushed forward to meet at the intersection area of the microfluidic chip.

Thus, I have developed a technique using hydrostatic pressure system to control the flow of the liquid in the microfluidic channels. The hydrostatic pressure setup is sketched in the Figure 8, where both inlets of the channels are connected individually to 50 ml syringes via Teflon tubes and the outlets are also connected to two separate reservoirs that serves as a dump. The vials are sufficiently large and open to the ambient so that the liquid level lowers insignificantly when liquid is flowing through the channels, which guarantees a constant pressure difference from inlets and outlets in the microfluidic channels during operation. By adjusting the different height of the reservoirs from inlets and outlets, the flow of the aqueous phase in the channels is precisely controlled. By increasing or decreasing the height of the reservoir connected to the inlets with respect to the reservoir connected to the outlets, positive or negative pressure difference between inlets and outlets can be applied to the channels to guide

the liquid fingers to move forward or backward. The approximate pressure difference to induce 0.001 µl/s flow is calculated to about 0.5 Pascal.

To produce a symmetric lipid bilayer, the microfluidic channels are first filled with squalene oil containing dissolved lipids with 5 mg/ml of DPhPC and DOPC in a molar ratio of 2:1. After flushing the channels with the oil, two aqueous fingers are slowly injected into the channels. During the injection, the water-oil interface of each aqueous finger is decorated with a phospholipid monolayer. Eventually, the two aqueous fingers gently meet and when they get close enough to each other, the rearrangement of the lipid starts in a way that the hydrophilic heads of the lipids are oriented towards the water aqueous phase and hydrophobic parts are oriented towards the oil phase. When contacting the two phospholipid monolayers they form a lipid bilayer. The formation of the bilayer is called zipping (Figure 9).

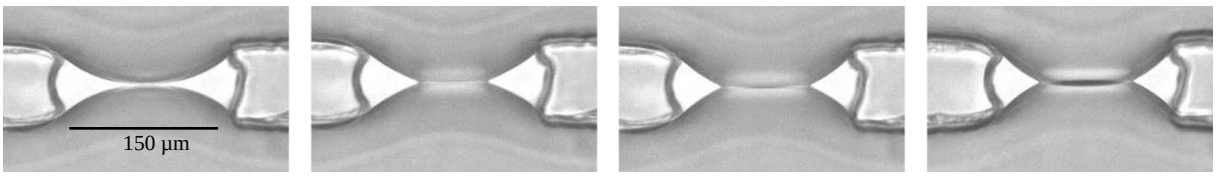

Figure 9. Top view of the intersection in the microfluidic device, where two phospholipid monolayers are gently brought into contact with each other and form a lipid bilayer by zipping after a few seconds.

To produce an asymmetric lipid bilayer, initially, only pure squalene oil is injected into the microfluidic device. Subsequently, two buffer fingers containing distinct lipid vesicles are introduced into each channel inlet. The vesicles composed of different lipids open up and self-arrange at the interfaces of each leaflet between water and oil. Once the aqueous fingers of both leaflets gently make contact, the asymmetric lipid bilayer, featuring two distinct lipid monolayers on each side, will form.

In collaboration with Alessandra Griffo within Prof. Jacobs' team in the SFB 1027 project B1, this platform was used to create a stable, free-standing lipid bilayer. The great stability of the lipid bilayer allowed to study the mechanical characteristics of the membrane using atomic force microscopy (AFM). For the formation of the lipid bilayer, she used another mixture of phospholipids which she explored how the presence of cholesterol and sphingomyelin influenced the elasticity of the lipid bilayer.

3.3. Patch-clamp

The patch clamp technique is a versatile electrophysiological tool for determining the electrical properties of real or model cell membranes and ion channels [113]. The information about electrical properties of the lipid bilayer allows us to obtain various parameters such as membrane area, membrane thickness, or ion currents through Arch-3. To realize those measurements, two Ag/AgCl electrodes are positioned on each side of the cell membrane in the aqueous solution. In contrast to the conventional whole cell mode, the electrode arrays in my case does not touch the actual membrane but is positioned at a certain distance from the artificial model membrane [114]. In my work, the electrodes were attached to the tubing and inserted into the PDMS device.

The electrical behaviour of model cell membranes can be described by an equivalent circuit consisting of a resistor in parallel with a capacitor. From an electrical point of view, capacitance is the amount of charge stored in two parallel plates separated by an insulator. Therefore, a phospholipid bilayer can be considered as an insulator separating two conducting (aqueous) phases and subsequently as capacitors [115]. Thus, for obtaining the membrane thickness, the capacitance of the membrane can be measured by applying AC voltage to the artificial model membrane [114], and subsequently by knowing the area of the membrane the thickness of the membrane can be obtained. The formula below shows that the amount of charge stored in a membrane is proportional to the area (A), the dielectric constant (K), the permittivity of free space (ε_0), and disproportional to the distance between phospholipid layers (d):

$$C = \frac{\varepsilon_0 \,.\, K \,.\, A}{d} \tag{1}$$

As the lipid composition of many biological membranes is similar, also the dielectric constant, permittivity, and the thickness of the bilayer are almost the same for other biological membranes. Thus, the capacitance of most model cell membranes is only proportional to its area (A), and its specific capacitance (C_s) having the unit of F/m^2. The specific capacitance was determined for similar solvent-containing lipid membrane to be around 4 mF/m^2 [112]:

$$C = C_s \cdot A \tag{2}$$

A capacitance measurement recorded during the formation of a lipid bilayer in a microfluidic device is shown in the Figure 10. The experiment is implemented with a positive continuous pressure applied to the inlets moving the aqueous fingers slowly forward to meet each other at the intersection of the channels, where eventually the bilayer is formed. The resulting first huge jump in the capacitance from the time t_0 to t_1 shown in the Figure 10d, is related to sudden formation of the lipid bilayer, so-called zipping. While the bilayer is already formed, small positive pressure difference between inlets and outlets continues to apply and the two aqueous fingers continue to move forward at very low speed. After formation of a certain bilayer area, the bilayer further extends at a slower speed to the edge of the microfluidic structure, as shown in the Figure 10d (t_2). During that process, the remaining oil is pushed out of the Plateau borders that act as oil reservoir and the oil is drained to the PDMS over the time, Figure 10c. After more than one hour, the lipid bilayer finally ruptures.

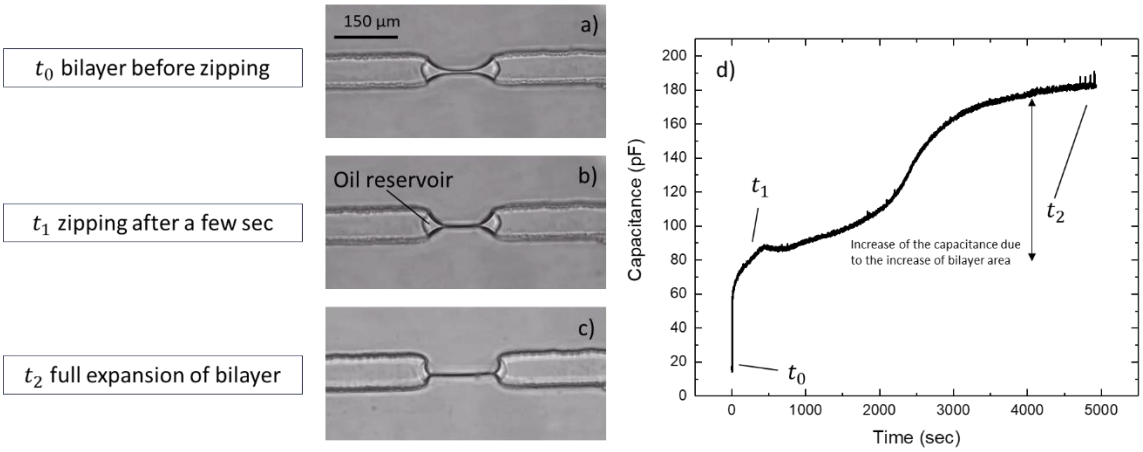

Figure 10. Optical microscopy view of the lipid bilayer formation that is simultaneously measured by patch-clamp to confirm the visual zipping is referred to the actual lipid bilayer formation. a) Liquid fingers contact at the cross section before zipping, t_0. b) Formation of the lipid bilayer at the t_1, so-called zipping. c) The full expansion of the lipid bilayer toward the edge of the boarder at the intersection after more than 1 hour, t_2. d) Capacitance measurement of the lipid bilayer. Over the time, the oil reservoir at the plateau boarder vanishes and drains to the PDMS causing the lipid bilayer expands and subsequently increasing its area. This leads to increase of the capacitance indicated at the t_2 in the graph.

3.4. Surface and membrane tension measurement

The surface and membrane tension is measured using the Young-Laplace equation, which relates the pressure difference across a lipid mono- or bilayer to the curvature and tension of the respective parts of a membrane [116-120].

The image in the Figure 11 shows a lipid bilayer that is bend by applying difference pressures to the channels in the microfluidic device. Using circle fittings to the curved lipid monolayer (Figure 11a) and bilayer (Figure 11b), we can determine the radius of curvature for each interface. As the vertical principal curvature of the bilayer (perpendicular to the image plane) is very small, the fitted circle in vertical direction would be almost infinite ($\frac{1}{R_{vertical} \approx \infty} \sim 0$), it can be neglected in relation to the principal curvature in horizontal direction. The horizontal (in plane) radius of curvature of the free parts of the upper and lower monolayer are R_{up} and R_{down}, respectively as shown in Figure 11a where there is an unequal pressure difference between leaflets. In case of a symmetric bilayer, i.e. identical surface tension σ of the considered water/oil interfaces decorated with a lipid monolayer, the externally applied pressure ΔP can be related to the optically measurable radii of curvature, via the Young-Laplace equation:

$$\Delta P = \sigma \left(\frac{1}{R_{up}} + \frac{1}{R_{down}} \right) \tag{3}$$

Note that the sign of the radii is different as the curvature of the monolayer is negative.

Using the radius of curvature of the lipid bilayer, $R_{bilayer}$, shown Figure 11b, also the bilayer tension $\Gamma_{bilayer}$ can be directly calculated to the externally applied pressure ΔP:

$$\Delta P = \frac{\Gamma_{bilayer}}{R_{bilayer}} \tag{4}$$

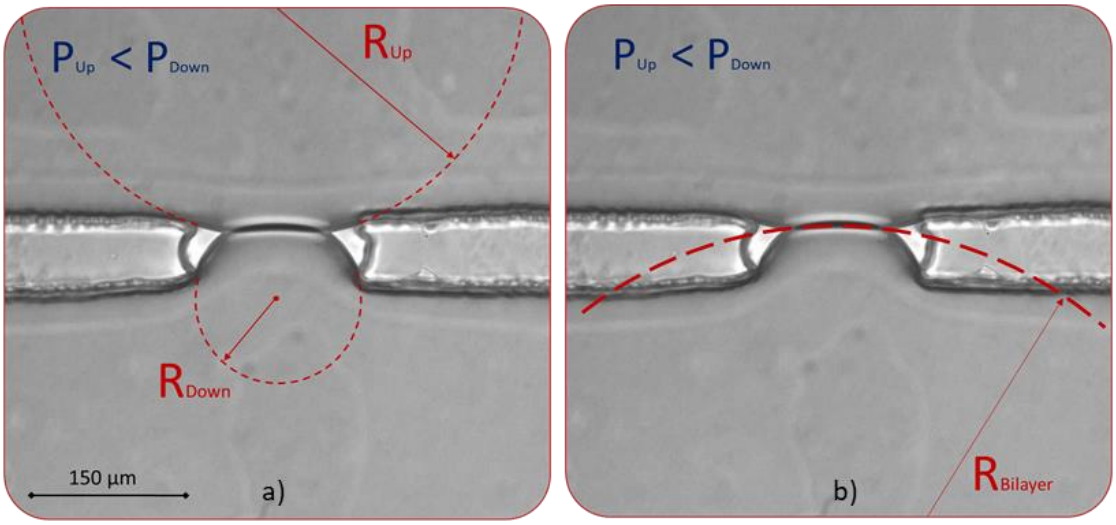

Figure 11. Micrograph of a lipid bilayer formed at the intersection of the microfluidic device with a positive applied pressure from downside causing bending the lipid bilayer upward. a) Shows the radius of curvature for the lipid monolayer of the upper and lower channel. b) Shows the radius of curvature for the bent lipid bilayer.

4. Results and Discussions

This chapter is based on four projects. Two of them have been published as peer reviewed articles, one exists as a pre-printed paper, and one has been submitted. The primary motivation driving these investigations was to introduce a novel method for regulating the creation of a free-standing lipid bilayer within a microfluidic system, aiming to facilitate membrane analysis. This analysis encompasses the exploration of protein-membrane interactions and the examination of membrane mechanical properties.

The publication by **Khangholi et al. in *Biomicrofluidics* 2020** [124] presents a new approach for creating free-standing lipid bilayers as model cell membranes in microfluidics using a hydrostatic pressure system. It was demonstrated that controlling the pressure in the microfluidic device results in increased lifetime of the lipid bilayer. Besides, the pressure control enables applying well defined pressure difference across the lipid bilayer. Using this control option, the surface tension of the lipid decorated oil-water interface and the bilayer tension could be extracted using Young-Laplace equation. This microfluidic scheme was also used in the publication submitted by **Griffo et al. in *bioRxiv* 2023** [126] to study the effect of cholesterol and sphingomyelin on the elasticity of the bilayer.

Having such a platform to form stable free-standing lipid bilayers with the ability to change the surrounding phase of the lipid bilayer, membrane-protein interaction was studied in the publication by **Khangholi et al in MDPI *Molecular Science* 2021** [125]. In this study, Archaeorhodopsin as a light-driven proton pump was used to study the light-induced opening of individual Arch-3 ion channels. The results showed the current signal obtained during excitation and revealed distinct steps upwards and downwards which indicates opening and closing of the ion channels. This study paved the way for a follow up project, studying signalling cascade using this platform; the preliminary results are available as a pre-print. In the project, the photoavtivation of G-protein coupled receptors (GPCRs) in Porcine Outer Segment (POS) from pig eyes is investigated. The results presents the electrical behaviour of gated ion channels in GPCR in the presence or absence of light. Due to the complexity of the cascade machinery in the lipid bilayer, the project is still ongoing and needs some final tests.

4.1. Surface lipid monolayer tension and lipid bilayer tension

Microfluidics is a highly adaptable and potent technique for model cell membrane analysis, which are categorized into three different methods, namely liposome-based, supported and suspended model cell membranes. In this chapter, I demonstrate a new approach using a microfluidic system to form suspended lipid bilayer as model cell membrane to overcome the potential difficulties of other methods such as having a long-life lipid bilayer with the ability of changing the surrounding phase of the bilayer, and having microscopic optical view, as well as measuring electrophysiological properties. In the followings, the achievements in the publication by **Khangholi et al. in *Biomicrofluidics* 2020** [124] are briefly discussed.

In this project, the lipid bilayers formed in microfluidic devices were manipulated using hydrostatic pressure system, which enables the great control over the liquid leaflets. Provided that the lipid bilayer is symmetric, i.e., both leaflets are composed of the same type of lipid and that the lipid coverage of both leaflets is identical, the bilayer remains optically flat when the pressure difference applied to each of the two aqueous fingers is the same, i.e. when the applied differential pressure across the bilayer is zero. If the pressure applied to both aqueous fingers is reduced to almost zero, the lipid bilayer remains still, and the area of the lipid bilayer will not increase. This results in an excellent stability of the lipid bilayer, which can last for more than 6 hours.

Once an unequal pressure is applied to the two aqueous fingers, the pressure difference between the two fingers causes a symmetrical bilayer to bend towards the lower pressure. The bending of the lipid bilayer also leads to an increase in the bilayer area and consequently to an increase in the capacitance signal.

The following experiment shows the series images of the lipid bilayer at different applied pressure differences between the upper and the lower aqueous finger for about 40 sec each and given about 10 sec time in between to relax (Figure 12a). It should be mentioned that the overall increase in the “base line” of the capacitance signal (or lipid bilayer area shown in the Figure 12c) from t = 100 s to t = 600 s is due to the drainage of the oil into the PDMS, since there was not given enough relaxation time between the different pressure steps, because the pressure differences were applied automatically, and the drainage of the oil was unavoidable.

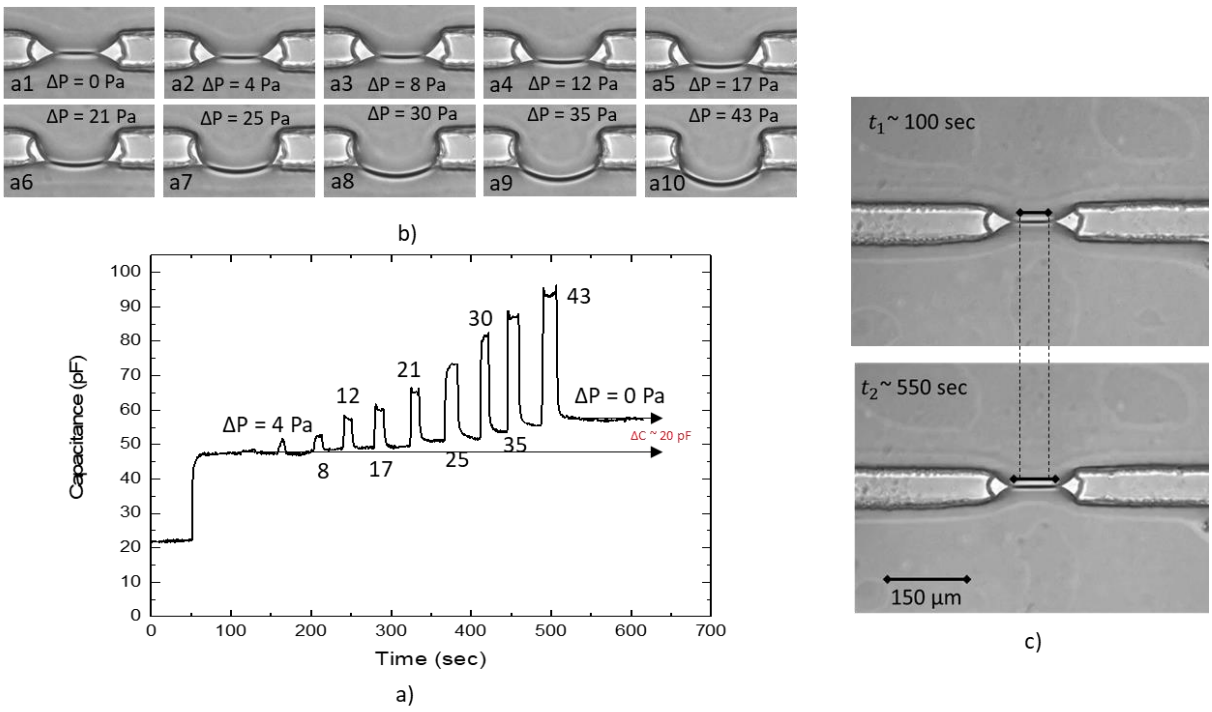

Figure 12. A series of microscopic images of the lipid bilayer under electrophysiological measurements. a) Various Laplace pressure differences were applied to the lipid bilayer for 40 seconds and 10 seconds rest time, respectively. The lipid bilayer remains curved for 40 seconds and the 10 seconds rest period is used to restore the flat state (equilibrium). b) Corresponding capacitance measurements of the curved lipid bilayer. c) The increase of the lipid bilayer area from the t_1 and t_2 due to the drainage of the oil in the oil reservoir during the experiment, which causes the over increase of the capacitance of 20 pF in total.

The radius of curvature of the bent lipid bilayer for each pressure difference step is obtained as described in the method part (Figure 11a). For the experimental situation of symmetric leaflets, the surface tension σ of the lipid monolayer were calculated using the Young-Laplace equation (eq. 3). The experiment was implemented for DOPC, DPhPC, and monoolein. The thus obtained surface tensions were compared to surface tension values obtained by standard pendant droplet measurements. Using the radius of curvature of the lipid bilayer (Figure 11b), the bilayer tension was calculated directly for DOPC, DPhPC, and Monoolein bilayer; the values are indicated in table II.

Table II. Surface tension of the lipid monolayer σ obtained from (a) the radius of the curvature of the free interfaces with respect to pressure difference using the Eq. 3 and (b) from the pendant droplet measurement. (c) The bilayer tension Γ obtained from the radius of the curvature of the bilayer using Eq. 4.

Lipid monolayer	DOPC (mN/m)	DPhPC (mN/m)	Monoolein (mN/m)
a) σ using eq. 3	8.2 ± 0.2	5.8 ± 0.2	2.5 ± 0.1
b) σ using pendant drop method	7.3 ± 1.7	6.1 ± 1.6	1.9 ± 0.3
c) Γ using eq. 4	12.6 ± 0.7	10.3 ± 0.6	4.8 ± 0.4

For an asymmetric DPhPC/DOPC lipid bilayer, the monolayer tension could not be extracted in this way, but the bilayer tension was calculated using six different applied pressure differences. The results are plotted in Figure 13 as a function of the curvature of the lipid bilayer. Fitting a linear dependence to the experimental data gives an value of the bilayer tension of (12.4 ± 0.5) mN/m for this asymmetric lipid bilayer averaged over all measurements.

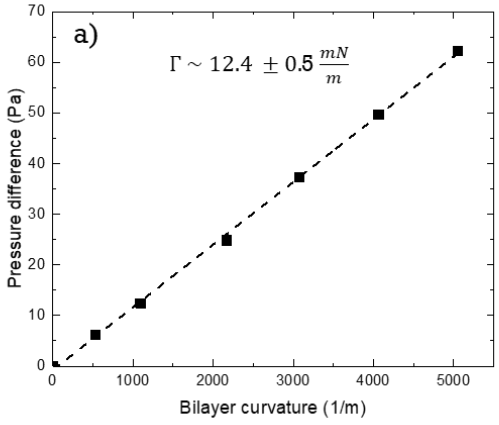

Figure 13. Applied six different pressure difference plotted against the corresponding curvature ($\frac{1}{R_{bilayer}}$) for an asymmetric DOPC/DPhPC lipid bilayer. The slope yields the bilayer tension (Γ).

In a side-project within Prof. Jacobs' team as part of the SFB 1027 project B1, Alessandra Griffo employed Atomic Force Microscopy (AFM) and microfluidics to examine the mechanical properties, including bilayer tension, elasticity, and morphological features. The objective was to replicate the plasma membrane using

pore-spanning membrane with its natural lipid compositions and delve into its intricate characteristics, with a specific emphasis on the roles of cholesterol and sphingomyelin. The findings in the publication by **Griffo et al. in *bioRxiv* 2023** [126] revealed that cholesterol and sphingomyelin contribute to increased membrane tension and rigidity, even within more complex plasma membrane compositions. In order to support her outcomes, she also used the microfluidic system particularly used in this thesis to form free standing lipid bilayers and obtain the lipid bilayer tension.

With all the above results, I have demonstrated that this microfluidic system enables the simultaneous measurement of surface tensions at lipid-decorated oil-water interfaces and the tension within a bilayer, all within a single experiment. This method significantly reduces experimental error compared to established standard measurements, as shown in Table I. In addition, this approach was extended to assess both surface and bilayer tensions in asymmetric lipid bilayers. The thus established microfluidic control scheme sets the foundation for the following studies of protein-bilayer interactions.

4.2. Photoactivation of Arch-3-EGFP

The great stability of the lipid bilayer generated by using the technique described above enabled me to further expand my research to study the interaction of proteins (Archaeuorhodopsin-3-EGFP) with a free-standing lipid bilayer. In this project, we took again advantage of the great optically and electrophysiologically access provided by the microfluidic scheme. The results are published in **Khangholi et al in MDPI *Molecular Science* 2021** [125] and are briefly summarized here. The formation of Arch-3 containing lipid bilayer and the activation of Arch-3-EGFP is sketched in the figure 14. Activation of Arch-3 was obtained by green laser illumination and detected using current intensity recording.

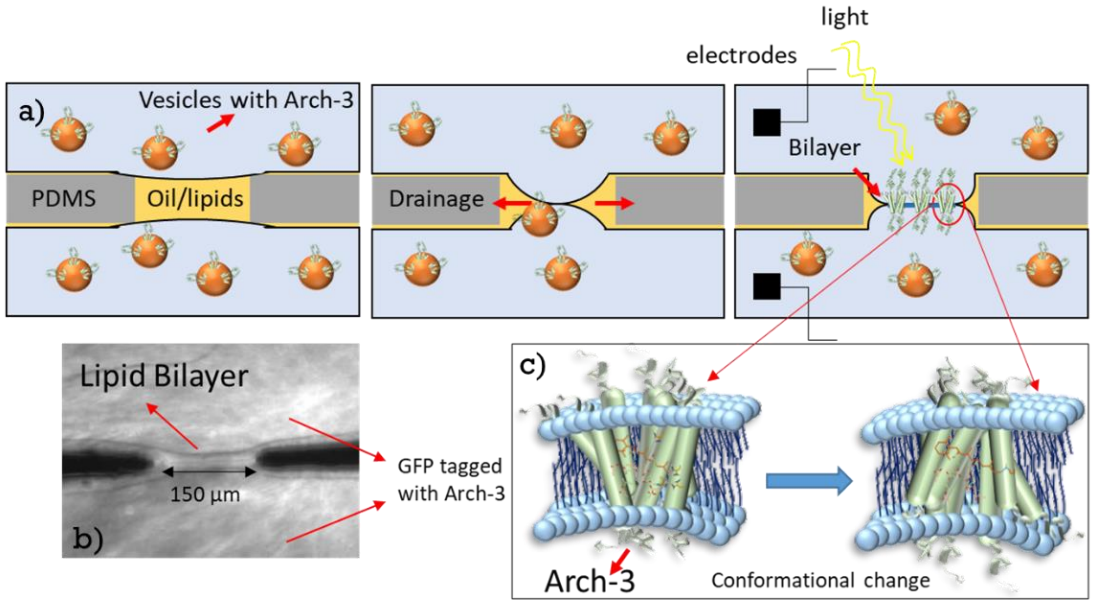

Figure 14. (a) A schematic of the formation of a lipid bilayer at the intersection of two microfluidic channels. b) The fluorescent signal of the EGFP tag from Arch-3 at the site of the suspended bilayer; PDMS elements remain. c) The conformational changes of Arch-3 upon light exposure mediated by the deprotonation of retinal.

The current recording shown in the figure 15a reveals no activity in the absence of light, i.e. in the first 40 second of the measurement. Subsequently, the lipid bilayer was exposed to green laser light ($\lambda = 532$ nm) for 10 sec. The electrical current spike at this time results from ions passing through the activated Arch-3. The signal decays after a several minutes to the initial value. The observation shows that as light-induced activation and deactivation of Arch-3. The activation of the Arch-3 opens the protein channel open, which according to the types of rhodopsin protein can occur within

picoseconds. The recovery of the Schiff base, however, requires milliseconds to several seconds in different cases. For the Arch-3 used in our experiment, ~84 sec is needed for the recovery of the Schiff base and to close the channel in the protein.

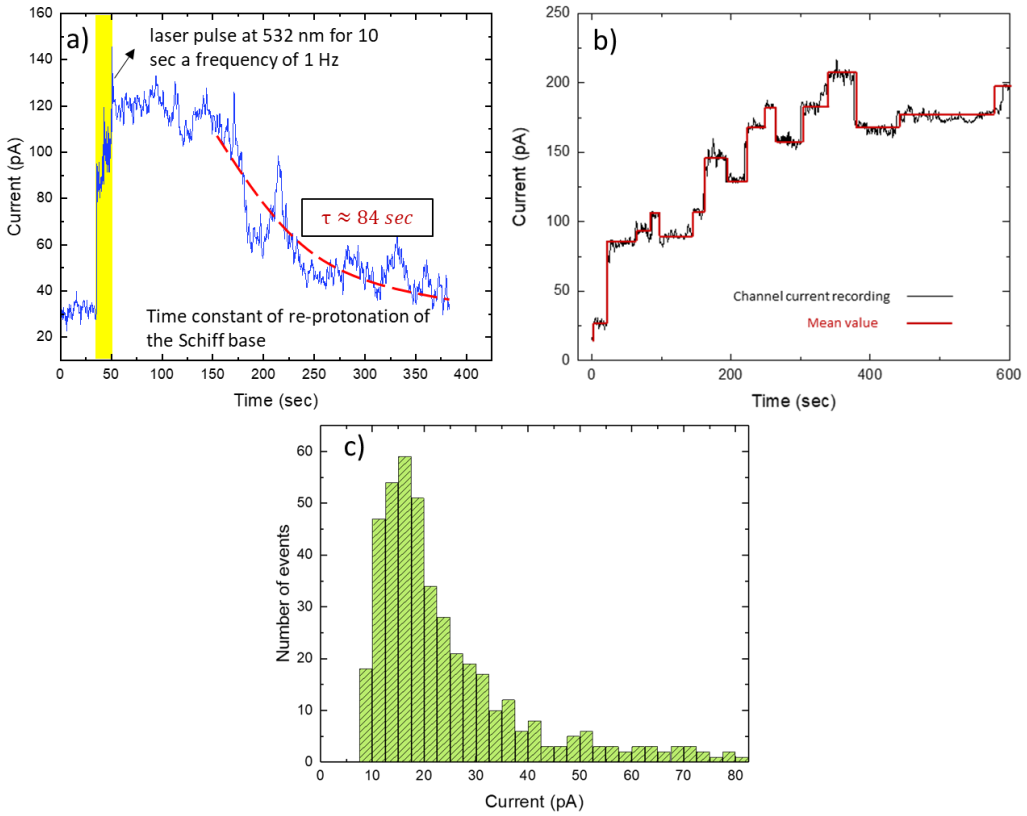

Figure 15. a) A real-time current recording of the bilayer containing Arch-3-EGFP. In the absence of light, we observe a current signal fluctuating around a constant value. The sudden jump in the current signal demonstrates the activation of Arch-3 caused by a green laser pulse applied to the bilayer at ~ 40 s < t < 50 s. The signal decays with a time constant of ~ 84 s, to its initial value in dark. b) Current signal as a function of time for an Arch-3-containing bilayer under continuous 532 nm laser illumination. c) The histogram shows the frequency of certain current steps grouped in intervals of 2.5 pA.

Here the result of over 300 individual current steps ΔI was recorded upon continuous illumination of the Arch-3 containing lipid bilayer by green laser light. It was found that most common current step is in the range of 16.25 ± 6.25 pA, which is in excellent agreement with the value found for the Bacteriorhodopsin [123]. This typical current step corresponds to a pore radius of the protein channels of (0.31 ± 0.02) nm. The radius pore of the Arch-3 protein is thus in agreement with the pore radius of Bacteriorhodopsin (0.4 – 1.19) nm and of rhodopsin (0.45 – 0.7) nm.

These results demonstrate a successful microfluidic strategy to monitor the electrical behaviour of light sensitive proteins in the lipid bilayer. Using Arch-3 as an example for light-responsive protein, it was proven that this strategy has the potential to further expand the research in the activation of light-responsive proteins in the lipid bilayer as only the protein can be changed instead of Arch-3 and incorporated into the lipid bilayer.

4.3. Porcine outer segment photoactivation

To go beyond a single light sensitive protein, we further used the microfluidic scheme to exploring signal cascading of G-protein coupled receptors (GPCRs). The project is ongoing and a preprint attached to this thesis. The project focused on studying the photoactivation of proteins incorporated into a lipid bilayer. In this work, utilizing porcine outer segments for GPCR photoactivation, we conducted the experiments both in the presence and absence of UV-light. Figure 16 presents the current recordings for these two separate experiments, exemplifying the reaction when light is switch on or off. In Figure 16a, the recording signal depicts the experiment commencing in the absence of light and subsequently switching the light on. Figure 16b, shows the experiment repeating the same process, however the light is subsequently switched off again. The electrical behaviour shown in both graphs demonstrates the corresponding opening and closure of gated channels in the porcine outer segments, influenced by changes in light conditions.

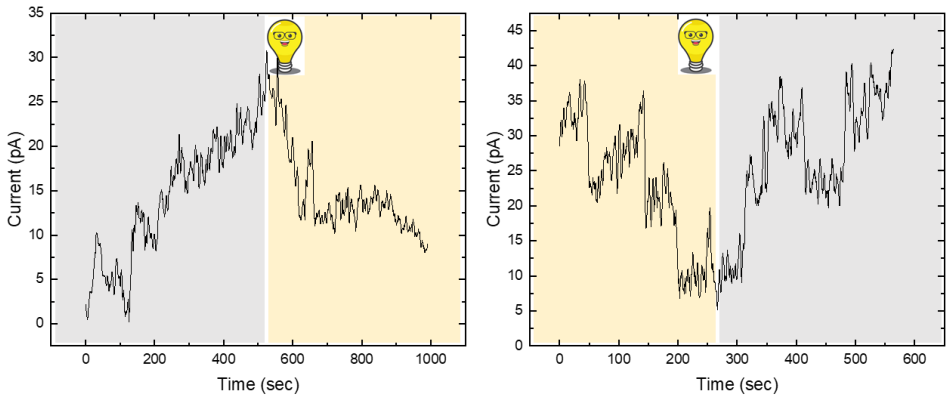

Figure 16. The current intensity as a function of time. The lipid bilayer is formed containing POS stock solution, and the current measurement is implemented in the absence and presence of light. a) The lipid bilayer is first formed in the presence of light. The current recording measurement starts once the light is switched off to monitor the activation of GPCR signalling in the dark. After a while, the light is switched on. b) The lipid bilayer is formed in the absence of light. The current recording measurement starts once the light is switched on to monitor the deactivation of GPCR signalling. After a while, the light is switched off again

In the detailed explanation of GPCR photoactivation provided in section 2.2.3, it was elucidated that the degradation of cGMP directly influences the opening and closure of gated channels, particularly in response to light. To emphasise this effect, two analogues were introduced, maintaining the gated channel consistently either open or closed, irrespective of light sensitivity. Figure 17 illustrates these results, elucidating

the crucial role played by the degradation of the cGMP enzyme in GPCR photoactivation.

This straightforward strategy demonstrates that the signalling cascade of GPCR in porcine outer segments (POS) can be effectively monitored within a lipid bilayer by observing the impact of the cGMP enzyme.

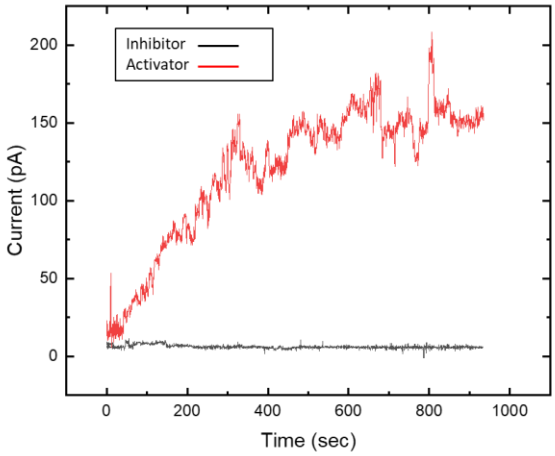

Figure 17. Recording the current over time in a lipid bilayer with POS containing both activator and inhibitor cGMP analogues reveals electrical behaviour unaffected by changes in light. The black line represents the recording with inhibitory cGMP analogues, indicating that the gated channel remains closed. In contrast, the red line illustrates an increase in current when using activatory cGMP analogues, signifying the consistent openness of the gated channel.

5. Summary and Outlooks

A microfluidic scheme was successfully developed to create a freestanding lipid bilayer in microfluidics. This approach offers advantages such as excellent optical and electrophysiological accessibility, as well as accurate monitoring of ongoing processes, making it an ideal tool for studying model membranes. By implementing a pressure-controlled system, the lifetime of the bilayer was significantly prolonged (up to approximately 6 hours) by effectively managing oil refilling the oil reservoir at the Plateau boarder. Through externally application of controlled pressure differences across the bilayer, in conjunction with its extended lifetime, I demonstrated the system's capability to simultaneously measure the surface tensions of lipid-decorated oil-water interfaces and the tension of the bilayer itself in a single experiment. Furthermore, I expanded the application of this technique to measure the surface and bilayer tensions of asymmetric lipid bilayers. It is expected that my method can be employed in the future to analyse asymmetric lipid bilayers with gel/fluid compositions, provided they exhibit sufficient stability during bending. Besides the great possibilities to explore the fundamental aspects of bilayer, this approach opens new possibilities of application such as investigation of biological process in the model cell membrane as protein-membrane interactions.

Having developed such a platform for studying the lipid bilayer properties, I further expanded my research to investigate the electrophysiological properties of the recombinantly produced transmembrane protein Arch-3 incorporated into lipid vesicles inserted into the lipid bilayer. By applying a voltage across the lipid bilayer containing Arch-3, the light-induced opening of individual Arch-3 ion channels could be observed, and the corresponding pore radius of the Arch-3 ion channel was determined to be (0.31 ± 0.02) nm, which is in excellent agreement with values found for similar protein pores. The in vitro system outlined in this description offers the advantage of swift testing and prototyping for modified Arch-3, as only DNA adaptation is required.

Additionally, it provides a platform for further investigating GPCR signalling as a signalling cascade. I utilized a stock solution of porcine outer segments derived from retinal tissue to observe the photoactivation signalling of GPCR. The preliminary results demonstrate that switching the light on and off leads to changes in current intensity. Specifically, current intensity rises in the absence of light, which is assumed to be due to the opening of gated channels, and it decreases in the presence of light possibly as a result of gated channels closing due to the degradation of cGMP to GMP. These initial results show that the entire cascade machinery could be inserted into a bilayer, but more test need to be done to ensure

that the recorded current intensity is from degradation of the cGMP to GMP. As part of an ongoing project, the cGMP inhibitor and activator was used to actively control the gated channels in the lipid bilayer, either keeping them closed or open, as the degradation of cGMP is the key factor in the entire process.

Overall, the developed microfluidic platform opens up new types of precise study of lipid bilayer properties and facilitates investigations into the electrophysiological characteristics of transmembrane proteins.

6. References

1. Antebi, Y. E.; Nandagopal, N.; Elowitz, M. B. An Operational View of Intercellular Signaling Pathways. *Current Opinion in Systems Biology* **2017**, *1*, 16–24. https://doi.org/10.1016/j.coisb.2016.12.003.
2. Voet, D.; Voet, J. G. *Biochemistry. Hauptbd.*, 2. rev. ed.; Wiley: New York, 1995.
3. Demonbreun, A. R.; McNally, E. M. Plasma Membrane Repair in Health and Disease. In *Current Topics in Membranes*; Elsevier, 2016; Vol. 77, pp 67–96. https://doi.org/10.1016/bs.ctm.2015.10.006.
4. Osaki, T.; Takeuchi, S. Artificial Cell Membrane Systems for Biosensing Applications. *Anal. Chem.* **2017**, *89* (1), 216–231. https://doi.org/10.1021/acs.analchem.6b04744.
5. Liu, L.; Yang, C.; Zhao, K.; Li, J.; Wu, H.-C. Ultrashort Single-Walled Carbon Nanotubes in a Lipid Bilayer as a New Nanopore Sensor. *Nat Commun* **2013**, *4* (1), 2989. https://doi.org/10.1038/ncomms3989.
6. Ashley, C. E.; Carnes, E. C.; Phillips, G. K.; Padilla, D.; Durfee, P. N.; Brown, P. A.; Hanna, T. N.; Liu, J.; Phillips, B.; Carter, M. B.; Carroll, N. J.; Jiang, X.; Dunphy, D. R.; Willman, C. L.; Petsev, D. N.; Evans, D. G.; Parikh, A. N.; Chackerian, B.; Wharton, W.; Peabody, D. S.; Brinker, C. J. The Targeted Delivery of Multicomponent Cargos to Cancer Cells by Nanoporous Particle-Supported Lipid Bilayers. *Nature Mater* **2011**, *10* (5), 389–397. https://doi.org/10.1038/nmat2992.
7. Montes, L.-R.; Alonso, A.; Goñi, F. M.; Bagatolli, L. A. Giant Unilamellar Vesicles Electroformed from Native Membranes and Organic Lipid Mixtures under Physiological Conditions. *Biophysical Journal* **2007**, *93* (10), 3548–3554. https://doi.org/10.1529/biophysj.107.116228.
8. Simões, S.; Filipe, A.; Faneca, H.; Mano, M.; Penacho, N.; Düzgünes, N.; Pedroso De Lima, M. Cationic Liposomes for Gene Delivery. *Expert Opinion on Drug Delivery* **2005**, *2* (2), 237–254. https://doi.org/10.1517/17425247.2.2.237.
9. Ries, R. S.; Choi, H.; Blunck, R.; Bezanilla, F.; Heath, J. R. Black Lipid Membranes: Visualizing the Structure, Dynamics, and Substrate Dependence of Membranes. *J. Phys. Chem. B* **2004**, *108* (41), 16040–16049. https://doi.org/10.1021/jp048098h.
10. Peetla, C.; Stine, A.; Labhasetwar, V. Biophysical Interactions with Model Lipid Membranes: Applications in Drug Discovery and Drug Delivery. *Mol. Pharmaceutics* **2009**, *6* (5), 1264–1276. https://doi.org/10.1021/mp9000662.
11. Singer, S. J.; Nicolson, G. L. The Fluid Mosaic Model of the Structure of Cell Membranes: Cell Membranes Are Viewed as Two-Dimensional Solutions of Oriented Globular Proteins and Lipids. *Science* **1972**, *175* (4023), 720–731. https://doi.org/10.1126/science.175.4023.720.

12. Patton, K. T.; Thibodeau, G. A. *The Human Body in Health & Disease*, Seventh edition.; Elsevier: St Louis, Missouri, 2018.

13. Xu, Y.; Tillman, T. S.; Tang, P. Membranes and Drug Action. In *Pharmacology*; Elsevier, 2009; pp 31–61. https://doi.org/10.1016/B978-0-12-369521-5.00003-8.

14. Simons, K.; Ikonen, E. Functional Rafts in Cell Membranes. *Nature* **1997**, *387* (6633), 569–572. https://doi.org/10.1038/42408.

15. Siontorou, C.; Nikoleli, G.-P.; Nikolelis, D.; Karapetis, S. Artificial Lipid Membranes: Past, Present, and Future. *Membranes* **2017**, *7* (3), 38. https://doi.org/10.3390/membranes7030038.

16. Harrison, R.; Lunt, G. G. *Biological Membranes: Their Structure and Function*, 2. ed.; Tertiary level biology; Blackie: Glasgow, 1980.

17. *Structure and Properties of Cell Membranes. Volume II, Molecular Basis of Selected Transport Systems*; Benga, G., Ed.; CRC Press: Boca Raton, 2018.

18. Seddon, A. M.; Casey, D.; Law, R. V.; Gee, A.; Templer, R. H.; Ces, O. Drug Interactions with Lipid Membranes. *Chem. Soc. Rev.* **2009**, *38* (9), 2509. https://doi.org/10.1039/b813853m.

19. Janmey, P. A.; Lindberg, U. Cytoskeletal Regulation: Rich in Lipids. *Nat Rev Mol Cell Biol* **2004**, *5* (8), 658–666. https://doi.org/10.1038/nrm1434.

20. Söderlund, T.; Alakoskela, J.-M. I.; Pakkanen, A. L.; Kinnunen, P. K. J. Comparison of the Effects of Surface Tension and Osmotic Pressure on the Interfacial Hydration of a Fluid Phospholipid Bilayer. *Biophysical Journal* **2003**, *85* (4), 2333–2341. https://doi.org/10.1016/S0006-3495(03)74657-8.

21. Deplazes, E.; Poger, D.; Cornell, B.; Cranfield, C. G. The Effect of Hydronium Ions on the Structure of Phospholipid Membranes. *Phys. Chem. Chem. Phys.* **2018**, *20* (1), 357–366. https://doi.org/10.1039/C7CP06776C.

22. Saeedimasine, M.; Montanino, A.; Kleiven, S.; Villa, A. Role of Lipid Composition on the Structural and Mechanical Features of Axonal Membranes: A Molecular Simulation Study. *Sci Rep* **2019**, *9* (1), 8000. https://doi.org/10.1038/s41598-019-44318-9.

23. Petelska, A. D.; Figaszewski, Z. A. Effect of pH on the Interfacial Tension of Lipid Bilayer Membrane. *Biophysical Journal* **2000**, *78* (2), 812–817. https://doi.org/10.1016/S0006-3495(00)76638-0.

24. Garcia-Manyes, S.; Oncins, G.; Sanz, F. Effect of Temperature on the Nanomechanics of Lipid Bilayers Studied by Force Spectroscopy. *Biophysical Journal* **2005**, *89* (6), 4261–4274. https://doi.org/10.1529/biophysj.105.065581.

25. Redondo-Morata, L.; Losada-Pérez, P.; Giannotti, M. I. Lipid Bilayers: Phase Behavior and Nanomechanics. In *Current Topics in Membranes*; Elsevier, 2020; Vol. 86, pp 1–55. https://doi.org/10.1016/bs.ctm.2020.08.005.

26. Cui, Z.; Chen, J.; Xue, Y.; Gan, J.; Chen, X.; Duan, H.; Zhang, R.; Liu, J.; Hao, J. Determination of Surface Tension and Surface Thermodynamic Properties of Nano-Ceria by

Low Temperature Heat Capacity. *Fluid Phase Equilibria* **2020**, *518*, 112627. https://doi.org/10.1016/j.fluid.2020.112627.

27. Shardt, N.; Wang, Y.; Jin, Z.; Elliott, J. A. W. Surface Tension as a Function of Temperature and Composition for a Broad Range of Mixtures. *Chemical Engineering Science* **2021**, *230*, 116095. https://doi.org/10.1016/j.ces.2020.116095.

28. Kyogoku, Y.; Fujiyoshi, Y.; Shimada, I.; Nakamura, H.; Tsukihara, T.; Akutsu, H.; Odahara, T.; Okada, T.; Nomura, N. Structural Genomics of Membrane Proteins. *Acc. Chem. Res.* **2003**, *36* (3), 199–206. https://doi.org/10.1021/ar0101279.

29. Wallin, E.; Heijne, G. V. Genome-wide Analysis of Integral Membrane Proteins from Eubacterial, Archaean, and Eukaryotic Organisms. *Protein Science* **1998**, *7* (4), 1029–1038. https://doi.org/10.1002/pro.5560070420.

30. Levental, I.; Lyman, E. Regulation of Membrane Protein Structure and Function by Their Lipid Nano-Environment. *Nat Rev Mol Cell Biol* **2023**, *24* (2), 107–122. https://doi.org/10.1038/s41580-022-00524-4.

31. Whited, A. M.; Johs, A. The Interactions of Peripheral Membrane Proteins with Biological Membranes. *Chemistry and Physics of Lipids* **2015**, *192*, 51–59. https://doi.org/10.1016/j.chemphyslip.2015.07.015.

32. Whited, A. M.; Johs, A. The Interactions of Peripheral Membrane Proteins with Biological Membranes. *Chemistry and Physics of Lipids* **2015**, *192*, 51–59. https://doi.org/10.1016/j.chemphyslip.2015.07.015.

33. Lee, A. G. How Lipids Affect the Activities of Integral Membrane Proteins. *Biochimica et Biophysica Acta (BBA) - Biomembranes* **2004**, *1666* (1–2), 62–87. https://doi.org/10.1016/j.bbamem.2004.05.012.

34. *Molecular Biology of the Cell*, 4th ed.; Alberts, B., Ed.; Garland Science: New York, 2002.

35. Orwick-Rydmark, M.; Lovett, J. E.; Graziadei, A.; Lindholm, L.; Hicks, M. R.; Watts, A. Detergent-Free Incorporation of a Seven-Transmembrane Receptor Protein into Nanosized Bilayer Lipodisq Particles for Functional and Biophysical Studies. *Nano Lett.* **2012**, *12* (9), 4687–4692. https://doi.org/10.1021/nl3020395.

36. Nürnberg, B.; Gudermann, T.; Schultz, G. Receptors and G Proteins as Primary Components of Transmembrane Signal Transduction: Part 2. G Proteins: Structure and Function. *J Mol Med* **1995**, *73* (3), 123–132. https://doi.org/10.1007/BF00198240.

37. Lefkowitz, R. J. Seven Transmembrane Receptors: Something Old, Something New. *Acta Physiologica* **2007**, *190* (1), 9–19. https://doi.org/10.1111/j.1365-201X.2007.01693.x.

38. Titeca, K.; Lemmens, I.; Tavernier, J.; Eyckerman, S. Discovering Cellular Protein-protein Interactions: Technological Strategies and Opportunities. *Mass Spectrometry Reviews* **2019**, *38* (1), 79–111. https://doi.org/10.1002/mas.21574.

39. Moore, D. T.; Berger, B. W.; DeGrado, W. F. Protein-Protein Interactions in the Membrane: Sequence, Structural, and Biological Motifs. *Structure* **2008**, *16* (7), 991–1001. https://doi.org/10.1016/j.str.2008.05.007.

40. Daley, D. The Assembly of Membrane Proteins into Complexes. *Current Opinion in Structural Biology* **2008**, *18* (4), 420–424. https://doi.org/10.1016/j.sbi.2008.04.006.

41. Del Sol, A.; Tsai, C.-J.; Ma, B.; Nussinov, R. The Origin of Allosteric Functional Modulation: Multiple Pre-Existing Pathways. *Structure* **2009**, *17* (8), 1042–1050. https://doi.org/10.1016/j.str.2009.06.008.

42. Del Sol, A.; Tsai, C.-J.; Ma, B.; Nussinov, R. The Origin of Allosteric Functional Modulation: Multiple Pre-Existing Pathways. *Structure* **2009**, *17* (8), 1042–1050. https://doi.org/10.1016/j.str.2009.06.008.

43. Perkins, J. R.; Diboun, I.; Dessailly, B. H.; Lees, J. G.; Orengo, C. Transient Protein-Protein Interactions: Structural, Functional, and Network Properties. *Structure* **2010**, *18* (10), 1233–1243. https://doi.org/10.1016/j.str.2010.08.007.

44. Le Coutre, J.; Kaback, H. R. Structure-Function Relationships of Integral Membrane Proteins: Membrane Transporters vs Channels. *Biopolymers* **2000**, *55* (4), 297–307. https://doi.org/10.1002/1097-0282(2000)55:4<297::AID-BIP1003>3.0.CO;2-H.

45. Tate, C. G. Overexpression of Mammalian Integral Membrane Proteins for Structural Studies. *FEBS Letters* **2001**, *504* (3), 94–98. https://doi.org/10.1016/S0014-5793(01)02711-9.

46. Levental, I.; Lyman, E. Regulation of Membrane Protein Structure and Function by Their Lipid Nano-Environment. *Nat Rev Mol Cell Biol* **2023**, *24* (2), 107–122. https://doi.org/10.1038/s41580-022-00524-4.

47. Baenziger, N. L.; Brodie, G. N.; Majerus, P. W. A Thrombin-Sensitive Protein of Human Platelet Membranes. *Proc. Natl. Acad. Sci. U.S.A.* **1971**, *68* (1), 240–243. https://doi.org/10.1073/pnas.68.1.240.

48. Bechinger, B. Towards Membrane Protein Design: pH-Sensitive Topology of Histidine-Containing Polypeptides. *Journal of Molecular Biology* **1996**, *263* (5), 768–775. https://doi.org/10.1006/jmbi.1996.0614.

49. Xu, C.; Ren, H.; Wang, S.; Peng, X. Proteomic Analysis of Salt-Sensitive Outer Membrane Proteins of Vibrio Parahaemolyticus. *Research in Microbiology* **2004**, *155* (10), 835–842. https://doi.org/10.1016/j.resmic.2004.07.001.

50. Bezanilla, F. How Membrane Proteins Sense Voltage. *Nat Rev Mol Cell Biol* **2008**, *9* (4), 323–332. https://doi.org/10.1038/nrm2376.

51. Ebbensgaard, A.; Mordhorst, H.; Aarestrup, F. M.; Hansen, E. B. The Role of Outer Membrane Proteins and Lipopolysaccharides for the Sensitivity of Escherichia Coli to Antimicrobial Peptides. *Front. Microbiol.* **2018**, *9*, 2153. https://doi.org/10.3389/fmicb.2018.02153.

52. Hilger, D.; Masureel, M.; Kobilka, B. K. Structure and Dynamics of GPCR Signaling Complexes. *Nat Struct Mol Biol* **2018**, *25* (1), 4–12. https://doi.org/10.1038/s41594-017-0011-7.

53. Hofmann, K. P.; Lamb, T. D. Rhodopsin, Light-Sensor of Vision. *Progress in Retinal and Eye Research* **2023**, *93*, 101116. https://doi.org/10.1016/j.preteyeres.2022.101116.

54. Simon, M. I.; Strathmann, M. P.; Gautam, N. Diversity of G Proteins in Signal Transduction. *Science* **1991**, *252* (5007), 802–808. https://doi.org/10.1126/science.1902986.

55. Arimont, M.; Van Der Woude, M.; Leurs, R.; Vischer, H. F.; De Graaf, C.; Nijmeijer, S. Identification of Key Structural Motifs Involved in 7 Transmembrane Signaling of Adhesion GPCRs. *ACS Pharmacol. Transl. Sci.* **2019**, *2* (2), 101–113. https://doi.org/10.1021/acsptsci.8b00051.

56. Antebi, Y. E.; Nandagopal, N.; Elowitz, M. B. An Operational View of Intercellular Signaling Pathways. *Current Opinion in Systems Biology* **2017**, *1*, 16–24. https://doi.org/10.1016/j.coisb.2016.12.003.

57. Bethani, I.; Skånland, S. S.; Dikic, I.; Acker-Palmer, A. Spatial Organization of Transmembrane Receptor Signalling. *EMBO J* **2010**, *29* (16), 2677–2688. https://doi.org/10.1038/emboj.2010.175.

58. Martemyanov, K. A. G Protein Signaling in the Retina and Beyond: The Cogan Lecture. *Investigative Ophthalmology & Visual Science* **2014**, *55* (12), 8201–8207. https://doi.org/10.1167/iovs.14-15928.

59. Smith, S. O. Mechanism of Activation of the Visual Receptor Rhodopsin. *Annu. Rev. Biophys.* **2023**, *52* (1), 301–317. https://doi.org/10.1146/annurev-biophys-083122-094909.

60. Seyedkarimi, M.-S.; Aramvash, A.; Ramezani, R. High Production of Bacteriorhodopsin from Wild Type Halobacterium Salinarum. *Extremophiles* **2015**, *19* (5), 1021–1028. https://doi.org/10.1007/s00792-015-0778-6.

61. Kataoka, M.; Kamikubo, H. Mechanism of the Light-Driven Proton Pump of Bacteriorhodopsin Based on the Consistency Principle. *BIOPHYSICS* **2019**, *16* (0), 274–279. https://doi.org/10.2142/biophysico.16.0_274.

62. Sapra, K. T.; Park, P. S.-H.; Palczewski, K.; Muller, D. J. Mechanical Properties of Bovine Rhodopsin and Bacteriorhodopsin: Possible Roles in Folding and Function. *Langmuir* **2008**, *24* (4), 1330–1337. https://doi.org/10.1021/la702299z.

63. Subramaniam, S.; Lindahl, M.; Bullough, P.; Faruqi, A. R.; Tittor, J.; Oesterhelt, D.; Brown, L.; Lanyi, J.; Henderson, R. Protein Conformational Changes in the Bacteriorhodopsin Photocycle 1 1Edited by B. Honig. *Journal of Molecular Biology* **1999**, *287* (1), 145–161. https://doi.org/10.1006/jmbi.1999.2589.

64. Das, I.; Pushkarev, A.; Sheves, M. Light-Induced Conformational Alterations in Heliorhodopsin Triggered by the Retinal Excited State. *J. Phys. Chem. B* **2021**, *125* (31), 8797–8804. https://doi.org/10.1021/acs.jpcb.1c04551.

65. Mukohata, Y.; Sugiyama, Y.; Ihara, K.; Yoshida, M. An Australian Halobacterium Contains a Novel Proton Pump Retinal Protein: Archaerhodopsin. *Biochemical and Biophysical Research Communications* **1988**, *151* (3), 1339–1345. https://doi.org/10.1016/S0006-291X(88)80509-6.

66. Ganapathy, S.; Kratz, S.; Chen, Q.; Hellingwerf, K. J.; De Groot, H. J. M.; Rothschild, K. J.; De Grip, W. J. Redshifted and Near-infrared Active Analog Pigments Based upon Archaerhodopsin-3. *Photochem & Photobiology* **2019**, *95* (4), 959–968. https://doi.org/10.1111/php.13093.

67. Bada Juarez, J. F.; Judge, P. J.; Adam, S.; Axford, D.; Vinals, J.; Birch, J.; Kwan, T. O. C.; Hoi, K. K.; Yen, H.-Y.; Vial, A.; Milhiet, P.-E.; Robinson, C. V.; Schapiro, I.; Moraes, I.; Watts, A. Structures of the Archaerhodopsin-3 Transporter Reveal That Disordering of Internal Water Networks Underpins Receptor Sensitization. *Nat Commun* **2021**, *12* (1), 629. https://doi.org/10.1038/s41467-020-20596-0.

68. Besaw, J. E.; Ou, W.-L.; Morizumi, T.; Eger, B. T.; Sanchez Vasquez, J. D.; Chu, J. H. Y.; Harris, A.; Brown, L. S.; Miller, R. J. D.; Ernst, O. P. The Crystal Structures of a Chloride-Pumping Microbial Rhodopsin and Its Proton-Pumping Mutant Illuminate Proton Transfer Determinants. *Journal of Biological Chemistry* **2020**, *295* (44), 14793–14804. https://doi.org/10.1074/jbc.RA120.014118.

69. Kazmin, R.; Rose, A.; Szczepek, M.; Elgeti, M.; Ritter, E.; Piechnick, R.; Hofmann, K. P.; Scheerer, P.; Hildebrand, P. W.; Bartl, F. J. The Activation Pathway of Human Rhodopsin in Comparison to Bovine Rhodopsin. *Journal of Biological Chemistry* **2015**, *290* (33), 20117–20127. https://doi.org/10.1074/jbc.M115.652172.

70. Fasciani, I.; Carli, M.; Petragnano, F.; Colaianni, F.; Aloisi, G.; Maggio, R.; Scarselli, M.; Rossi, M. GPCRs in Intracellular Compartments: New Targets for Drug Discovery. *Biomolecules* **2022**, *12* (10), 1343. https://doi.org/10.3390/biom12101343.

71. Hilger, D. The Role of Structural Dynamics in GPCR-mediated Signaling. *The FEBS Journal* **2021**, *288* (8), 2461–2489. https://doi.org/10.1111/febs.15841.

72. Mazé, A.; Benenson, Y. Artificial Signaling in Mammalian Cells Enabled by Prokaryotic Two-Component System. *Nat Chem Biol* **2020**, *16* (2), 179–187. https://doi.org/10.1038/s41589-019-0429-9.

73. Shi, K.; Song, C.; Wang, Y.; Chandrawati, R.; Lin, Y. Engineering Receptor-Mediated Transmembrane Signaling in Artificial and Living Cells. *Commun Mater* **2023**, *4* (1), 65. https://doi.org/10.1038/s43246-023-00394-z.

74. Serebryany, E.; Zhu, G. A.; Yan, E. C. Y. Artificial Membrane-like Environments for in Vitro Studies of Purified G-Protein Coupled Receptors. *Biochimica et Biophysica Acta (BBA) - Biomembranes* **2012**, *1818* (2), 225–233. https://doi.org/10.1016/j.bbamem.2011.07.047.

75. Jelinek, R.; Silbert, L. Biomimetic Approaches for Studying Membrane Processes. *Mol. BioSyst.* **2009**, *5* (8), 811. https://doi.org/10.1039/b907223n.

76. Knoll, W.; Köper, I.; Naumann, R.; Sinner, E.-K. Tethered Bimolecular Lipid Membranes—A Novel Model Membrane Platform. *Electrochimica Acta* **2008**, *53* (23), 6680–6689. https://doi.org/10.1016/j.electacta.2008.02.121.

77. Bally, M.; Bailey, K.; Sugihara, K.; Grieshaber, D.; Vörös, J.; Städler, B. Liposome and Lipid Bilayer Arrays Towards Biosensing Applications. *Small* **2010**, *6* (22), 2481–2497. https://doi.org/10.1002/smll.201000644.

78. Kiessling, V.; Yang, S.-T.; Tamm, L. K. Supported Lipid Bilayers as Models for Studying Membrane Domains. In *Current Topics in Membranes*; Elsevier, 2015; Vol. 75, pp 1–23. https://doi.org/10.1016/bs.ctm.2015.03.001.

79. Lin, W.-C.; Blanchette, C. D.; Ratto, T. V.; Longo, M. L. Lipid Asymmetry in DLPC/DSPC-Supported Lipid Bilayers: A Combined AFM and Fluorescence Microscopy Study. *Biophysical Journal* **2006**, *90* (1), 228–237. https://doi.org/10.1529/biophysj.105.067066.

80. Castellana, E. T.; Cremer, P. S. Solid Supported Lipid Bilayers: From Biophysical Studies to Sensor Design. *Surface Science Reports* **2006**, *61* (10), 429–444. https://doi.org/10.1016/j.surfrep.2006.06.001.

81. Andersson, J.; Bilotto, P.; Mears, L. L. E.; Fossati, S.; Ramach, U.; Köper, I.; Valtiner, M.; Knoll, W. Solid-Supported Lipid Bilayers – A Versatile Tool for the Structural and Functional Characterization of Membrane Proteins. *Methods* **2020**, *180*, 56–68. https://doi.org/10.1016/j.ymeth.2020.09.005.

82. Cevc, G.; Richardsen, H. Lipid Vesicles and Membrane Fusion. Advanced Drug *Delivery Reviews* **1999**, *38* (3), 207–232. https://doi.org/10.1016/S0169-409X(99)00030-7.

83. Bangham, A. D.; Horne, R. W. Negative Staining of Phospholipids and Their Structural Modification by Surface-Active Agents as Observed in the Electron Microscope. *Journal of Molecular Biology* **1964**, *8* (5), 660-IN10. https://doi.org/10.1016/S0022-2836(64)80115-7.

84. Mayer, L. D.; Hope, M. J.; Cullis, P. R. Vesicles of Variable Sizes Produced by a Rapid Extrusion Procedure. *Biochimica et Biophysica Acta (BBA) - Biomembranes* **1986**, *858* (1), 161–168. https://doi.org/10.1016/0005-2736(86)90302-0.

85. Breton, M.; Amirkavei, M.; Mir, L. M. Optimization of the Electroformation of Giant Unilamellar Vesicles (GUVs) with Unsaturated Phospholipids. *J Membrane Biol* **2015**, *248* (5), 827–835. https://doi.org/10.1007/s00232-015-9828-3.

86. Montes, L.-R.; Alonso, A.; Goñi, F. M.; Bagatolli, L. A. Giant Unilamellar Vesicles Electroformed from Native Membranes and Organic Lipid Mixtures under Physiological

Conditions. *Biophysical Journal* **2007**, *93* (10), 3548–3554. https://doi.org/10.1529/biophysj.107.116228.

87. Ries, R. S.; Choi, H.; Blunck, R.; Bezanilla, F.; Heath, J. R. Black Lipid Membranes: Visualizing the Structure, Dynamics, and Substrate Dependence of Membranes. *J. Phys. Chem. B* **2004**, *108* (41), 16040–16049. https://doi.org/10.1021/jp048098h.

88. Zeineldin, R.; Last, J. A.; Slade, A. L.; Ista, L. K.; Bisong, P.; O'Brien, M. J.; Brueck, S. R. J.; Sasaki, D. Y.; Lopez, G. P. Using Bicellar Mixtures To Form Supported and Suspended Lipid Bilayers on Silicon Chips. *Langmuir* **2006**, *22* (19), 8163–8168. https://doi.org/10.1021/la060817r.

89. Pautot, S.; Frisken, B. J.; Cheng, J.-X.; Xie, X. S.; Weitz, D. A. Spontaneous Formation of Lipid Structures at Oil/Water/Lipid Interfaces. *Langmuir* **2003**, *19* (24), 10281–10287. https://doi.org/10.1021/la034532f.

90. Bayley, H.; Cronin, B.; Heron, A.; Holden, M. A.; Hwang, W. L.; Syeda, R.; Thompson, J.; Wallace, M. Droplet Interface Bilayers. *Mol. BioSyst.* **2008**, *4* (12), 1191. https://doi.org/10.1039/b808893d.

91. Nguyen, M.-A.; Srijanto, B.; Collier, C. P.; Retterer, S. T.; Sarles, S. A. Hydrodynamic Trapping for Rapid Assembly and in Situ Electrical Characterization of Droplet Interface Bilayer Arrays. *Lab Chip* **2016**, *16* (18), 3576–3588. https://doi.org/10.1039/C6LC00810K.

92. Barlow, N. E.; Bolognesi, G.; Haylock, S.; Flemming, A. J.; Brooks, N. J.; Barter, L. M. C.; Ces, O. Rheological Droplet Interface Bilayers (Rheo-DIBs): Probing the Unstirred Water Layer Effect on Membrane Permeability via Spinning Disk Induced Shear Stress. *Sci Rep* **2017**, *7* (1), 17551. https://doi.org/10.1038/s41598-017-17883-0.

93. Allen-Benton, M.; Findlay, H. E.; Booth, P. J. Probing Membrane Protein Properties Using Droplet Interface Bilayers. *Exp Biol Med (Maywood)* **2019**, *244* (8), 709–720. https://doi.org/10.1177/1535370219847939.

94. Mruetusatorn, P.; Polizos, G.; Datskos, P. G.; Taylor, G.; Sarles, S. A.; Boreyko, J. B.; Hayes, D. G.; Collier, C. P. Control of Membrane Permeability in Air-Stable Droplet Interface Bilayers. *Langmuir* **2015**, *31* (14), 4224–4231. https://doi.org/10.1021/la504712g.

95. Venkatesan, G. A.; Lee, J.; Farimani, A. B.; Heiranian, M.; Collier, C. P.; Aluru, N. R.; Sarles, S. A. Adsorption Kinetics Dictate Monolayer Self-Assembly for Both Lipid-In and Lipid-Out Approaches to Droplet Interface Bilayer Formation. *Langmuir* **2015**, *31* (47), 12883–12893. https://doi.org/10.1021/acs.langmuir.5b02293.

96. Haylock, S.; Friddin, M. S.; Hindley, J. W.; Rodriguez, E.; Charalambous, K.; Booth, P. J.; Barter, L. M. C.; Ces, O. Membrane Protein Mediated Bilayer Communication in Networks of Droplet Interface Bilayers. *Commun Chem* **2020**, *3* (1), 77. https://doi.org/10.1038/s42004-020-0322-1.

97. Elfaramawy, M. A.; Fujii, S.; Uyeda, A.; Osaki, T.; Takeuchi, S.; Kato, Y.; Watanabe, H.; Matsuura, T. Quantitative Analysis of Cell-Free Synthesized Membrane Proteins at the Stabilized Droplet Interface Bilayer. *Chem. Commun.* **2018**, *54* (86), 12226–12229. https://doi.org/10.1039/C8CC06804F.

98. Alcinesio, A.; Krishna Kumar, R.; Bayley, H. Functional Multivesicular Structures with Controlled Architecture from 3D-Printed Droplet Networks. *ChemSystemsChem* **2022**, *4* (1), e202100036. https://doi.org/10.1002/syst.202100036.

99. Ogishi, K.; Osaki, T.; Morimoto, Y.; Takeuchi, S. 3D Printed Microfluidic Devices for Lipid Bilayer Recordings. *Lab Chip* **2022**, *22* (5), 890–898. https://doi.org/10.1039/D1LC01077H.

100. Stanley, C. E.; Elvira, K. S.; Niu, X. Z.; Gee, A. D.; Ces, O.; Edel, J. B.; deMello, A. J. A Microfluidic Approach for High-Throughput Droplet Interface Bilayer (DIB) Formation. *Chem. Commun.* **2010**, *46* (10), 1620. https://doi.org/10.1039/b924897h.

101. Funakoshi, K.; Suzuki, H.; Takeuchi, S. Lipid Bilayer Formation by Contacting Monolayers in a Microfluidic Device for Membrane Protein Analysis. *Anal. Chem.* **2006**, *78* (24), 8169–8174. https://doi.org/10.1021/ac0613479.

102. Tawfik, H.; Puza, S.; Seemann, R.; Fleury, J.-B. Transport Properties of Gramicidin A Ion Channel in a Free-Standing Lipid Bilayer Filled With Oil Inclusions. *Front. Cell Dev. Biol.* **2020**, *8*, 531229. https://doi.org/10.3389/fcell.2020.531229.

103. Terry, S. C.; Jerman, J. H.; Angell, J. B. A Gas Chromatographic Air Analyzer Fabricated on a Silicon Wafer. *IEEE Trans. Electron Devices* **1979**, *26* (12), 1880–1886. https://doi.org/10.1109/T-ED.1979.19791.

104. Manz, A.; Graber, N.; Widmer, H. M. Miniaturized Total Chemical Analysis Systems: A Novel Concept for Chemical Sensing. *Sensors and Actuators B: Chemical* **1990**, *1* (1–6), 244–248. https://doi.org/10.1016/0925-4005(90)80209-I.

105. Cui, P.; Wang, S. Application of Microfluidic Chip Technology in Pharmaceutical Analysis: A Review. *Journal of Pharmaceutical Analysis* **2019**, *9* (4), 238–247. https://doi.org/10.1016/j.jpha.2018.12.001.

106. Niculescu, A.-G.; Chircov, C.; Bîrcă, A. C.; Grumezescu, A. M. Fabrication and Applications of Microfluidic Devices: A Review. *IJMS* **2021**, *22* (4), 2011. https://doi.org/10.3390/ijms22042011.

107. Squires, T. M.; Quake, S. R. Microfluidics: Fluid Physics at the Nanoliter Scale. *Rev. Mod. Phys.* **2005**, *77* (3), 977–1026. https://doi.org/10.1103/RevModPhys.77.977.

108. Ashraf, M. W.; Tayyaba, S.; Afzulpurkar, N. Micro Electromechanical Systems (MEMS) Based Microfluidic Devices for Biomedical Applications. *IJMS* **2011**, *12* (6), 3648–3704. https://doi.org/10.3390/ijms12063648.

109. Whitesides, G. M.; Ostuni, E.; Takayama, S.; Jiang, X.; Ingber, D. E. Soft Lithography in Biology and Biochemistry. *Annu. Rev. Biomed. Eng.* **2001**, *3* (1), 335–373. https://doi.org/10.1146/annurev.bioeng.3.1.335.

110. Kane, R. S.; Stroock, A. D.; Li Jeon, N.; Ingber, D. E.; Whitesides, G. M. Soft Lithography and Microfluidics. In *Optical Biosensors*; Elsevier, 2002; pp 571–595. https://doi.org/10.1016/B978-044450974-1/50018-5.

111. Pinto, V.; Sousa, P.; Cardoso, V.; Minas, G. Optimized SU-8 Processing for Low-Cost Microstructures Fabrication without Cleanroom Facilities. *Micromachines* **2014**, *5* (3), 738–755. https://doi.org/10.3390/mi5030738.

112. Heo, P.; Ramakrishnan, S.; Coleman, J.; Rothman, J. E.; Fleury, J.; Pincet, F. Highly Reproducible Physiological Asymmetric Membrane with Freely Diffusing Embedded Proteins in a 3D-Printed Microfluidic Setup. *Small* **2019**, *15* (21), 1900725. https://doi.org/10.1002/smll.201900725.

113. Walker, V.; Vuister, G. W. Biochemistry and Pathophysiology of the Transient Potential Receptor Vanilloid 6 (TRPV6) Calcium Channel. In *Advances in Clinical Chemistry*; Elsevier, 2023; Vol. 113, pp 43–100. https://doi.org/10.1016/bs.acc.2022.11.002.

114. Zhao, Y.; Inayat, S.; Dikin, D. A.; Singer, J. H.; Ruoff, R. S.; Troy, J. B. Patch Clamp Technique: Review of the Current State of the Art and Potential Contributions from Nanoengineering. *Proceedings of the Institution of Mechanical Engineers, Part N: Journal of Nanoengineering and Nanosystems* **2008**, *222* (1), 1–11. https://doi.org/10.1243/17403499JNN149.

115. Vargas, J. N.; Seemann, R.; Fleury, J.-B. Fast Membrane Hemifusion via Dewetting between Lipid Bilayers. *Soft Matter* **2014**, *10* (46), 9293–9299. https://doi.org/10.1039/C4SM01577K.

116. Petelska, A. D.; Naumowicz, M.; Figaszewski, Z. A. The Interfacial Tension of the Lipid Membrane Formed from Lipid–Amino Acid Systems. *Cell Biochem Biophys* **2011**, *61* (2), 289–296. https://doi.org/10.1007/s12013-011-9207-3.

117. Petelska, A. D.; Naumowicz, M.; Figaszewski, Z. A. The Interfacial Tension of the Lipid Membrane Formed From Lipid–Cholesterol and Lipid–Lipid Systems. *CBB* **2006**, *44* (2), 205–212. https://doi.org/10.1385/CBB:44:2:205.

118. Petelska, A. Interfacial Tension of Bilayer Lipid Membranes. *Open Chemistry* **2012**, *10* (1), 16–26. https://doi.org/10.2478/s11532-011-0130-7.

119. Petelska, A. D.; Figaszewski, Z. A. Interfacial Tension of the Two-Component Bilayer Lipid Membrane Modelling of Cell Membrane. *Bioelectrochemistry and Bioenergetics* **1998**, *46* (2), 199–204. https://doi.org/10.1016/S0302-4598(98)00138-X.

120. Petelska, A. D.; Figaszewski, Z. A. Interfacial Tension of the Lipid Membrane Formed from Phosphatidylcholine–Decanoic Acid and Phosphatidylcholine–Decylamine Systems. *J Membrane Biol* **2011**, *241* (2), 103–108. https://doi.org/10.1007/s00232-011-9366-6.

121. Finkler, M.; Ott, A. Bead-Based Assay for Spatiotemporal Gene Expression Control in Cell-Free Transcription–Translation Systems. *BioTechniques* **2019**, *66* (1), 29–33. https://doi.org/10.2144/btn-2018-0097.

122. Parinot, C.; Rieu, Q.; Chatagnon, J.; Finnemann, S. C.; Nandrot, E. F. Large-Scale Purification of Porcine or Bovine Photoreceptor Outer Segments for Phagocytosis Assays on Retinal Pigment Epithelial Cells. *JoVE* **2014**, No. 94, 52100. https://doi.org/10.3791/52100.

123. Radzwill, N.; Gerwert, K.; Steinhoff, H.-J. Time-Resolved Detection of Transient Movement of Helices F and G in Doubly Spin-Labeled Bacteriorhodopsin. *Biophysical Journal* **2001**, *80* (6), 2856–2866. https://doi.org/10.1016/S0006-3495(01)76252-2.

124. Khangholi, N.; Seemann, R.; Fleury, J.-B. Simultaneous Measurement of Surface and Bilayer Tension in a Microfluidic Chip. *Biomicrofluidics* **2020**, *14* (2), 024117. https://doi.org/10.1063/1.5137810.

125. Khangholi, N.; Finkler, M.; Seemann, R.; Ott, A.; Fleury, J.-B. Photoactivation of Cell-Free Expressed Archaerhodopsin-3 in a Model Cell Membrane. *IJMS* **2021**, *22* (21), 11981. https://doi.org/10.3390/ijms222111981.

126. Griffo, A.; Sparn, C.; Lolicato, F.; Nolle, F.; Khangholi, N.; Seemann, R.; Fleury, J.-B.; Brinkmann, M.; Nickel, W.; Hähl, H. Mechanics of Biomimetic Free-Standing Lipid Membranes: Insights on Lipid Chemistry and Bilayer Elasticity. *Preprint; Biophysics*, **2023**. https://doi.org/10.1101/2023.08.21.554126.

7. List of publications

I) Navid Khangholi, Ralf Seemann, Jean-Baptiste Fleury. Simultaneous measurement of surface and bilayer tension in a microfluidic chip. Biomicrofluidics. **2020**, 14(2):024117.

II) Navid Khangholi, Marc Finkler, Ralf Seemann, Albrecht Ott, Jean-Baptiste Fleury. Photoactivation of Cell-Free Expressed Archaerhodopsin-3 in a Model Cell Membrane. Int J Mol Sci. **2021**, 22(21):11981

III) Alessandra Griffo, Carola Sparn, Fabio Lolicato, Friederike Nolle, Navid Khangholi, Ralf Seemann, Jean-Baptiste Fleury, Martin Brinkmann, Walter Nickel, Hendrik Hähl. Mechanics of biomimetic free-standing lipid membranes: Insights on lipid chemistry and bilayer elasticity. **(submitted)**

IV) Navid Khangholi, Marc Finkler, Sieun Sung, Mahsa Mohammadian, Jean-Baptiste Fleury, Albrecht Ott, Ralf Seemann. Photoactivation of GPCR from Porcine Outer Segment in lipid bilayer using microfluidics. (**pre-printed version)**

Appendices

Appendix (I) Simultaneous measurement of surface and bilayer tension in a microfluidic chip

Authors: Navid Khangholi, Ralf Seemann, Jean-Baptiste Fleury

Experimental Physics, Saarland University, 66123 Saarbrücken, Germany

DOI: 10.1063/1.5137810

Author contributions:

Fabrication of microfluidic device, running the experiments, and interpreting the analysis were conducted by N. Khangholi. The paper was written by N. Khangholi, R. Seemann, and J.B. Fleury. The research was directed by R. Seemann.

Abstract:

Freestanding lipid bilayers are one of the most used model systems to mimic biological cell membranes. To form an unsupported bilayer, we employ two aqueous fingers in a microfluidic chip surrounded by an oily phase that contains lipids. Upon pushing two aqueous fingers forward, their interface becomes decorated with a lipid monolayer and eventually zip to form a bilayer when the monolayers have nanoscopic contact with each other. Using this straightforward approach, the quick and easy bilayer formation is facilitated by oil draining into the microfluidic device material consisting of polydimethylsiloxane. However, the oil drainage limits the lifetime of a bilayer to about 1 h. We demonstrate that this drainage can be managed, resulting in superior bilayer stability and an increased lifetime of several hours when using a pressure-controlled system. Applying different pressures to the aqueous fingers in the microfluidic chip, the formed bilayer can even be bent to a desired curvature. Extracting the contact angle and the resulting curvature of the bilayer region, for a given applied pressure difference, both the bilayer tension and the surface tension of each lipid monolayer can be derived from a single experiment using the Young Laplace pressure equation.

Biomicrofluidics ARTICLE scitation.org/journal/bmf

Simultaneous measurement of surface and bilayer tension in a microfluidic chip

Cite as: Biomicrofluidics 14, 024117 (2020); doi: 10.1063/1.5137810
Submitted: 14 November 2019 · Accepted: 10 April 2020 ·
Published Online: 27 April 2020

Navid Khangholi, Ralf Seemann, and Jean-Baptiste Fleury[a)]

AFFILIATIONS

Experimental Physics and Center for Biophysics, Saarland University, 66123 Saarbrücken, Germany

[a)]**Author to whom correspondence should be addressed:** jean-baptiste.fleury@physik.uni-saarland.de

ABSTRACT

Freestanding lipid bilayers are one of the most used model systems to mimic biological cell membranes. To form an unsupported bilayer, we employ two aqueous fingers in a microfluidic chip surrounded by an oily phase that contains lipids. Upon pushing two aqueous fingers forward, their interface becomes decorated with a lipid monolayer and eventually zip to form a bilayer when the monolayers have nanoscopic contact with each other. Using this straightforward approach, the quick and easy bilayer formation is facilitated by oil draining into the microfluidic device material consisting of polydimethylsiloxane. However, the oil drainage limits the lifetime of a bilayer to about 1 h. We demonstrate that this drainage can be managed, resulting in superior bilayer stability and an increased lifetime of several hours when using a pressure-controlled system. Applying different pressures to the aqueous fingers in the microfluidic chip, the formed bilayer can even be bent to a desired curvature. Extracting the contact angle and the resulting curvature of the bilayer region, for a given applied pressure difference, both the bilayer tension and the surface tension of each lipid monolayer can be derived from a single experiment using the Young Laplace pressure equation.

I. INTRODUCTION

A cell membrane is a barrier to the external environment that is commonly mimicked in model systems by a simple phospholipid bilayer. Artificial lipid bilayers are simplified models that have been used as platforms to understand biological processes occurring at the cell membrane.[1,2] They are also used for biotechnological purposes such as DNA-chip fast sequencing,[3] drug delivery,[4,5] or artificial photosynthesis.[6,7]

There are two major platforms to explore the properties of lipid bilayers, which are either lipid vesicles or planar bilayers. Lipid vesicles are basically bilayers in a spherical shape, which are commonly used in biological and biochemical purposes because of their ease of synthesis and handling.[8] Instead, a planar lipid bilayer consisting of two separated lipid monolayers stabilized by a solvent is referred to as a Black Lipid Membrane (BLM). BLMs can be formed either on a supported solid substrate[9–11] or can be unsupported.[12–14] Advantages of the BLM methods over the lipid vesicle method are the possibility of electrophysiological measurements and the exchange of chemical reagents without the need of tedious vesicle handling and manipulation.[15–17] Moreover, a major issue for using supported lipid bilayers (SLBs) for biomembrane modeling is decoupling of the membrane from the substrate. Therefore, in this work, we would like to emphasize on studying the properties and features of an unsupported lipid bilayer.

One of the recent approaches with this technique, the droplet interface bilayer (DIB), has been specifically developed to produce a solvent-free lipid bilayer having a rich lipid composition. This method also enables a rapid membrane characterization, drug screening, and ion channel recordings, whereas the possibility of having a continuous flow surrounding the bilayer in the DIB technique is somehow limited.[18–22] Thus, many miniaturized apparatus have been developed, such as microfluidic devices, to overcome the drawbacks of all the previous techniques.[19,23–25] Moreover, the formation of lipid bilayers in microfluidic devices presents the advantage of changing the buffer around the bilayer[26,27] while enabling good optical and electrophysiological access without using an undesired solvent (typically oil), which is essential for various biotechnological purposes.[28] However, it is well-understood that in microfluidic devices made of PDMS (polydimethylsiloxane), the oil is absorbed by the PDMS with time, due to the drainage of the oil. This supports the formation of the bilayer and also affects its lifetime, which is essentially destroyed when too much of the oil is drained.[26,27] Nevertheless, despite the

large body of research in the literature on the freestanding bilayer in microfluidics, the stability and lifetime of the freestanding bilayers are, in general, barely discussed.[29,30]

In this article, it is shown how the oil that is draining into the PDMS can be restored and subsequently how the lifetime of the bilayer can be improved substantially, which enables new classes of experiments to explore bilayer properties. Taking advantage of the improved lifetime, we presented a new approach to measuring the bilayer tension of symmetric and asymmetric lipid bilayers in a microfluidic device.

II. EXPERIMENTAL SECTION

A. Lipid preparation

DOPC (1,2-dioleoyl-sn-glycero-3-phosphocholine), DPhPC (1,2-diphytanoyl-sn-glycero-3-phosphocholine), and Monoolein (1-Oleoyl-rac-glycerol) were used as test lipids. DOPC is one of the most common lipids in the human cell membrane. DPhPC is a less biological relevant lipid, but known to produce a very stable bilayer. DOPC and DPhPC lipids were purchased from Avanti Polar Lipids, and Monoolein was purchased from Sigma Aldrich. The surface tensions of lipid decorated interfaces between aqueous buffer solution and squalene (Table I) were determined using the standard pendant drop technique using a commercial device (OCA20, Data Physics). To prepare the oil lipid solution, 5 mg/ml of the lipids were dissolved in 1 ml of pure squalene oil at 45 °C during continuous stirring for 3 h.

B. Device fabrication and setup operation

The microfluidic geometry consisted of two channels side by side forming an *X* geometry, as can be seen in Fig. 1. The channels have a rectangular cross section of 300 μm width and 100 μm height. The two microchannels meet at an intersection with an extension of 150 μm. Microfluidic devices with this geometry were fabricated using standard soft lithography protocols.[31] The device was molded into Sylgard 184 (Dow Corning, USA) from a SU-8 photoresist structure on a silicon wafer. After removing the mold, the surface of the Sylgard 184 devices was exposed to nitrogen plasma (Diener electronic GmbH, Germany) and the device was sealed with a plasma-treated glass cover slide. The glass cover slide was also coated with a very thin layer of PDMS (approximately 100 μm). The sealed device was rendered hydrophobic again by heating it to 135 °C overnight.

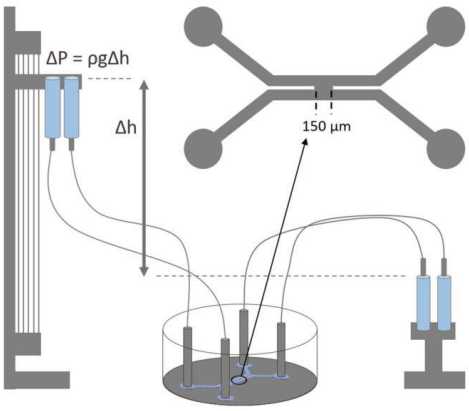

FIG. 1. Schematic of the microfluidic setup including the hydrostatic pressure control and the microfluidic mold structure. The inlets of the microfluidic device are connected to two syringes that are fixed on a motorized stage, and the outlets are connected to two reservoirs at a fixed height position.

The microfluidic device was connected to a hydrostatic pressure system that is presented in Fig. 1. The two inlets were connected to two 50 ml syringes via 50-cm-long Teflon tubes. The two outlets were connected to other reservoir vials with a fixed position. To guarantee a constant pressure at the outlets, the vials are open to the ambient air and are sufficiently large so that the liquid level does not rise remarkably during an experiment. The flows in the channels were controlled by adjusting the height of the inlet reservoirs, which were fixed on a motorized positioning stage with a resolution of 10 μm giving a pressure resolution of approximately 0.1 Pa. Depending on height of the inlet reservoirs, positive or negative pressures could be applied to the channels causing the liquid finger to move forward or backward (Fig. 1). The approximate pressure to induce 0.001 μl/s flow is about 0.5 Pa.

To produce a symmetric bilayer, the microfluidic chip is initially filled with squalene containing dissolved lipids. To form a bilayer, two buffer fingers containing 100 mM NaCl are injected into the channels applying the same pressure difference between inlets and outlets. Upon injection of the buffer solutions, their water–oil interfaces get decorated with lipids, until they gently meet at the intersection [cf. Fig. 2(a) (left) (Multimedia view)]. When the two lipid decorated water–oil interfaces come sufficiently close to each other, the lipids start to rearrange at their interface and form a bilayer, which can be observed by optical microscopy as seen in Fig. 2(a) (right) (Multimedia view).

To produce an asymmetric bilayer, different lipids are sonicated in the buffer solution leading to vesicles with a diameter of approximately 40 nm. In this case, initially, pure oil is flushed into the microfluidic chip, and two buffer fingers containing different vesicles are injected into the channels and meet at the intersection to form an asymmetric bilayer.[28]

The electrical properties of a bilayer can be analyzed by electrophysical measurements using a patch-clamp amplifier, EPC 10 USB (Heka Electronics). For that purpose Ag/AgCl electrodes were prepared by inserting a 5-cm-long silver wire in a borosilicate glass pipet containing a 100 mM NaCl electrolyte solution and applying 5 V for 30 min. The prepared electrodes were inserted into the circular inlet areas of the microfluidic device. The capacitance of the bilayer is measured using the lock-in function provided by the patch-clamp amplifier, while applying an 10 mV sinusoidal wave with a frequency of 10 kHz as an excitation signal.

III. RESULTS AND DISCUSSION

Figure 2(b) shows two capacitance measurements, which were recorded during the formation of the bilayer. At the beginning of

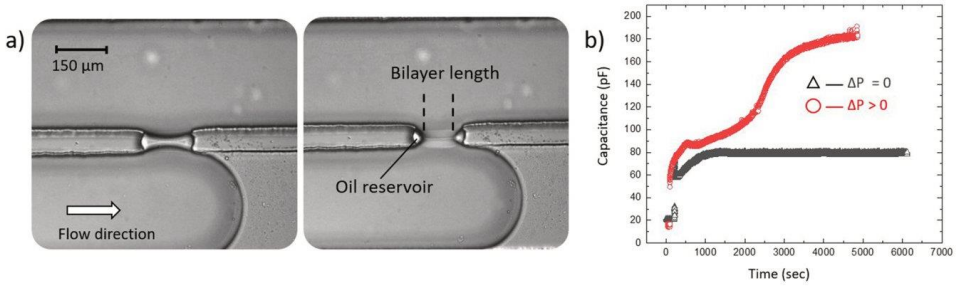

FIG. 2. (a) Top view of the intersection in the microfluidic device, where two phospholipid monolayers are gently brought into contact with each other (left) and form a lipid bilayer by *zipping* after a few seconds (right). (b) Electrophysiological measurements during the formation of the lipid bilayer. To record the red data, a constant pressure difference $\Delta P = P_{outlets} - P_{inlets} \approx 25$ mPa was applied to both aqueous fingers, resulting in a slow continuous forward movement of the aqueous finger and a continuously increasing bilayer length. To record the black data, the same initial pressure was applied, but reduced to zero within about 10 min after bilayer formation, resulting in a constant bilayer length, i.e., a constant capacitance signal. In order to increase the lifetime of the bilayer up to approximately 6 h, the drainage of the oil should be restored in the oil reservoir by applying slightly negative pressure difference. Multimedia view: https://doi.org/10.1063/1.5137810.1; https://doi.org/10.1063/1.5137810.2

the experiments, a pressure difference ΔP was applied to both liquid fingers in order to bring them into contact at the intersection and to form a bilayer. This pressure difference ΔP is defined as the difference of the applied pressure to the inlets and outlets $\Delta P = P_{outlets} - P_{inlets}$. In order to keep the bilayer flat, an equal pressure difference is applied to the upper and bottom channels, $\Delta P_{up} = \Delta P_{down}$. From an electrical point of view, a lipid bilayer can be considered as a capacitor and the formation of a lipid bilayer leads to a jump in the capacitance signal, which confirms that the two involved lipid monolayers become closer during the so-called *zipping* step. In Fig. 2(b), the first jump in both capacitance signals is related to the *zipping* of the bilayer, i.e., the bilayer formation. As for the red signal, the applied pressure remained constant ($\Delta P > 0$), and, therefore, both aqueous fingers continue to move forward at slow speed. During the shown time period, slightly more than 1 h the bilayer extended to the edge of the structure and finally ruptured, which can be seen by the increasing and then suddenly ending capacitance signal [cf. red curve in Fig. 2(b)]. For the black capacitance signal, the pressure applied to both aqueous fingers ($\Delta P_{up} = \Delta P_{Down}$) was slowly reduced to zero ($\Delta P = 0$), within about 10 min after the *zipping*. This eventually stopped the forward movement of the aqueous fingers and resulted in a steady value for the capacitance measurement and a superior bilayer stability of typically 6 h.

To understand the improved stability of the bilayer when reducing the applied pressure, we first have to understand what typically leads to the bilayer rupture. Initially, when two aqueous fingers are injected into the channels, they displace the oil in such a way that some of the oil wets the walls of the channels. It is well-known that liquids can penetrate through PDMS even if not noticeably swelling it,[28] and certainly our used oil (squalene) is drained into the PDMS chip. When the remaining oil on the wall of the channels is drained into the PDMS chip and not replenished, the bilayer ruptures after a long time. In general, the drainage time is a function of the oil viscosity. The more viscous the oil is, the longer the oil drainage takes. The oil drainage is visible by a reduced extension of the "oil reservoirs" to the left and right of the bilayer and a parallel extension of the bilayer [cf. Fig. 2(a) (right) (Multimedia view)]. However, to replenish the drained oil on the wall of the channels' oil reservoir [see Fig. 2(a) (right) (Multimedia view)], we need a source of oil enabling a flow through the wall of the channels. This source is the remaining oil surrounding the lipid bilayer. By applying a slightly negative pressure to the liquid finger, the remaining oil in the microfluidic channel can even restore the oil in the oil reservoir [see Fig. 2(a) (right) (Multimedia view)]. This effect would also allow us to change the bilayer area by applying positive and negative pressure difference [see Fig. 2(a) (right) (Multimedia view)]. Properly adjusting the applied pressure (ΔP) between inlet and outlet thus facilitates maintaining a bilayer with a superior lifetime of approximately 6 h (Multimedia view). The images collected for recording the bilayer lifetime of 6 h were 969 images with 22 Hz to frame per second (FPS). However, the lifetime is also limited in this case due to the mechanical fluctuation or flow fluctuation.

Taking advantage of the optimized control of the bilayer formation and increased lifetime, a new class of experiments is feasible. In the following, we will show how surface and bilayer tensions of symmetric and asymmetric bilayers can be simultaneously obtained, from a single experiment using this type of pressure control.

A. Simultaneous surface tension and bilayer tension measurements

When the pressure difference $\Delta P'$ between the upper channel and the lower channel is zero $\Delta P' = \Delta P_{Up} - \Delta P_{Down} = 0$, a bilayer remains flat, provided that the bilayer is symmetric, i.e., both leaflets consist of the same type of lipids. In case $\Delta P' \neq 0$, the pressure difference between the two fingers leads to a curvature of a symmetric bilayer. In other words, a bilayer bends away from the side where the pressure is larger. Of course, such a bent bilayer can be

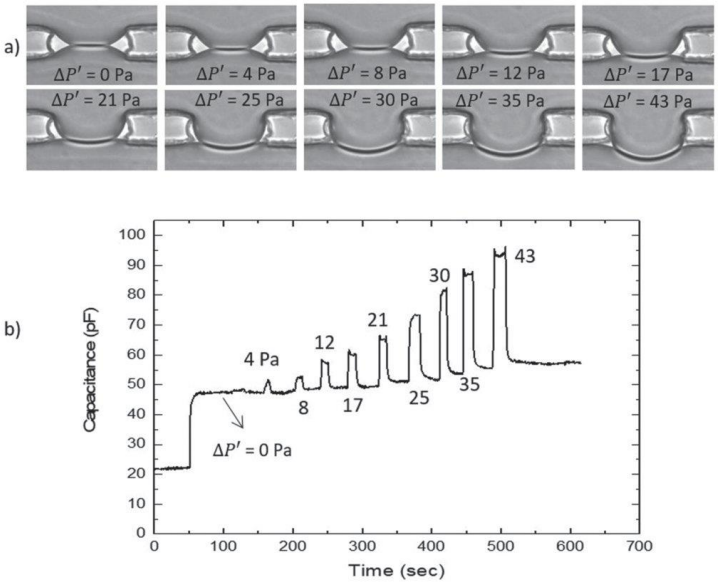

FIG. 3. (a) Optical micrographs of the symmetric bilayer with various pressure differences $\Delta P' = \Delta P_{Up} - \Delta P_{Down}$ applied to the aqueous fingers in the up and down channels. (b) Corresponding capacitance measurements of the bend bilayer; the bilayer area and thus the capacitance increase as the bilayer bends. Multimedia view: https://doi.org/10.1063/1.5137810.3

brought back to its flat shape, once the pressure difference between both sides become equal again.

Figure 3(a) shows image series of a bilayer at different pressure differences $|\Delta P'| = |\Delta P_{Up} - \Delta P_{Down}|$ that was applied between the upper and the lower aqueous finger for about 40 s each and given about 10 s time in between to relax [see Fig. 3 (Multimedia view)]. The corresponding capacitance measurements are shown in Fig. 3(b) and confirm that by bending the bilayer, the length of the bilayer (respectively, the bilayer area) increases, resulting in the increase of capacitance. It must be mentioned that the overall increase of the capacitance (respectively, the bilayer area) from $t \approx 100$ s to $t \approx 600$ s is due to the drainage of the oil into the PDMS as not enough relaxation time was given in between the various applied pressure steps.

The applied pressure differences $\Delta P'$ can be expressed also by the difference in Laplace pressures of the free interfaces of the upper monolayer $\Delta P_{Up} \approx \frac{\sigma_{Up}}{R_{Up}}$ and the lower monolayer $\Delta P_{Down} \approx \frac{\sigma_{Down}}{R_{Down}}$,

$$\Delta P' = \Delta P_{Up} - \Delta P_{Down} \approx \frac{\sigma_{Up}}{R_{Up}} - \frac{\sigma_{Down}}{R_{Down}}. \quad (1)$$

In Eq. (1), σ_{Up} and σ_{Down} are the surface tensions of the respective oil–water interfaces decorated with a lipid monolayer. In this case, only the principal curvatures in horizontal direction R_{Up} and R_{Down} are considered, whereas the principal curvatures in vertical direction (perpendicular to the image plane) are very small and can be safely neglected.

The externally applied pressure difference $\Delta P'$ between both liquid fingers is known and the radii of the curvature of the monolayer R_{Up} and R_{Down} can be obtained from the microscopic images by fitting circular arcs to the free lipid decorated oil–water interfaces, as indicated in Fig. 4. So, in the symmetric case where the surface tensions of the upper and lower water finger against oil are equal, it is straightforward to obtain $\sigma = \sigma_{Up} = \sigma_{Down}$ using the Young–Laplace equation (1).

In Fig. 5, those measurements are shown for six different applied pressure conditions, whereas the fitted slope provides the surface tension averaged over these six measurements for the oil–water interface decorated with a certain lipid. Using this protocol, the phospholipids DPhPC, DOPC, and Monoolein were tested separately to obtain their surface tensions and were compared to values obtained by standard surface tension measurements in Table I. The obtained values agree quite well within experimental error, while the experimental accuracy of our presented surface tension measurement is improved by a factor of 5–10 with respect to the standard pendant drop measurement. The errors in our case typically come from the precision of fitting the surface curvature via the software ImageJ and could be further decreased by increasing the image resolution. All the measurements for the surface tension and the bilayer tension have been done for the same badge of phospholipids. However, according to the literature, it could be possible that with different oil compositions, different results may be obtained.[26,27,32]

Besides the surface tension σ of the monolayer decorated oil–water interfaces, the bilayer tension Γ of both symmetric and

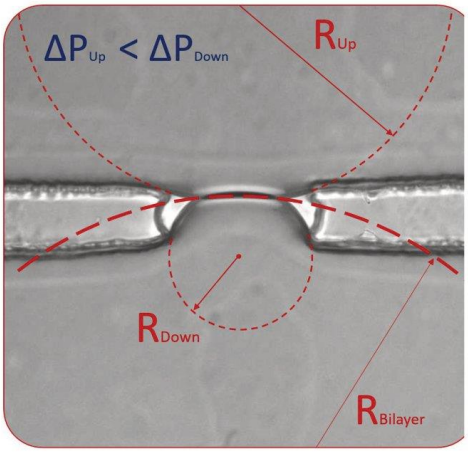

FIG. 4. Micrograph of a symmetric bilayer formed at the intersection of the microfluidic device with a negative pressure difference applied ($\Delta P' = \Delta P_{Up} - \Delta P_{Down} < 0$) bending the bilayer upward. The principal radii of the curvature of the free monolayer of the upper (R_{Up}) and lower aqueous finger (R_{Down}) at the "oil triangle" and the radius of the curvature of the bilayer ($R_{bilayer}$) are indicated.

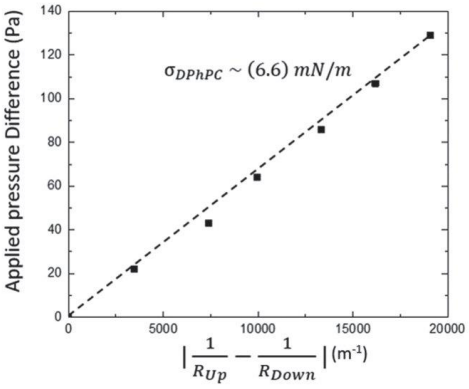

FIG. 5. The fitted slope provides the averaged surface tension, which is the pressure difference as a function of the increased curvature of the lipid monolayer on the both sides. The shown data are present for a DPhPC lipid monolayer.

TABLE I. Surface tension of the lipid monolayer σ obtained from (a) the radius of the curvature of the free interfaces with respect to pressure difference using the Young–Laplace equation (1) and (b) from the pendant droplet measurement. The bilayer tension Γ obtained from (c) the radius of the curvature of the bilayer using Eq. (2) and (d) obtained using Eq. (3).

	Lipid monolayer	DOPC (mN/m)	DPhPC (mN/m)	Monoolein (mN/m)
(a)	σ using Eq. (1)	8.2 ± 0.2	5.8 ± 0.2	2.5 ± 0.1
(b)	σ using pendant drop	7.3 ± 1.7	6.1 ± 1.6	1.9 ± 0.3
(c)	Γ using Eq. (2)	12.6 ± 0.7	10.3 ± 0.6	4.8 ± 0.4
(d)	Γ using Eq. (3)	12.4 ± 3	9.8 ± 2.6	4.2 ± 1.8

asymmetric bilayers can also be obtained from the same optical images when additionally fitting the radius of the curvature of the bilayer $R_{bilayer}$ (cf. Fig. 4) for a known applied pressure difference $\Delta P'$,

$$\Delta P' = \frac{\Gamma}{R_{bilayer}}. \tag{2}$$

In Fig. 6(a), the applied pressure difference $\Delta P'$ is shown as a function of the corresponding bilayer curvature $R_{bilayer}$ for an asymmetric DOPC/DPhPC bilayer. Fitting the slope provides an averaged value for the bilayer tension, leading to (12.4 ± 0.5) mN/m in this case. The values for the bilayer tension Γ obtained for symmetric DOPC, DPhPC, and Monoolein bilayer using this approach [Eq. (2)] are also given in Table I. These values are in agreement with those calculated from the surface tensions of symmetric leaflets ($\sigma_{Up} = \sigma_{Down} = \sigma$) and the corresponding contact angle $\theta = \theta_{Up} + \theta_{Down}$ in between them [cf. Fig. 6(b)], using

$$\Gamma = 2 \cdot \sigma \cdot \cos\left(\frac{\theta}{2}\right). \tag{3}$$

However, even though the results from both approaches are identical with respect to their experimental uncertainty, we find that experimental uncertainty is reduced by a factor of about four when using the approach of a bent bilayer, i.e., Eq. (2).

In the case of an asymmetric bilayer, we cannot use Eq. (3), and the bilayer tension is given by

$$\Gamma = \sigma_{Up} \cos\theta_{Up} + \sigma_{Down} \cos\theta_{Down}, \tag{4}$$

whereas θ_{Up} and θ_{Down} have to be measured with respect to the tangent to the bilayer at the three-phase contact point [see Fig. 6(b)]. However, measuring the contact angles with respect to the tangent is very hard to do and provides a large error. But based on our experimental finding for the tested combinations of lipids, both angles are very similar, $\theta_{Up} \approx \theta_{Down}$. Using this experimental finding in Eq. (4), the bilayer tension can be written as $\Gamma \approx (\sigma_{Up} + \sigma_{Down}) \cos\left(\frac{\theta}{2}\right)$. So, knowing Γ from Eq. (2), we can solve the equation for one of the surface tensions σ_{Up} or σ_{Down} and insert this in Eq. (1), respectively, to obtain both surface tensions and the bilayer tension from a single microscopy image. This has been done for the previous example of an

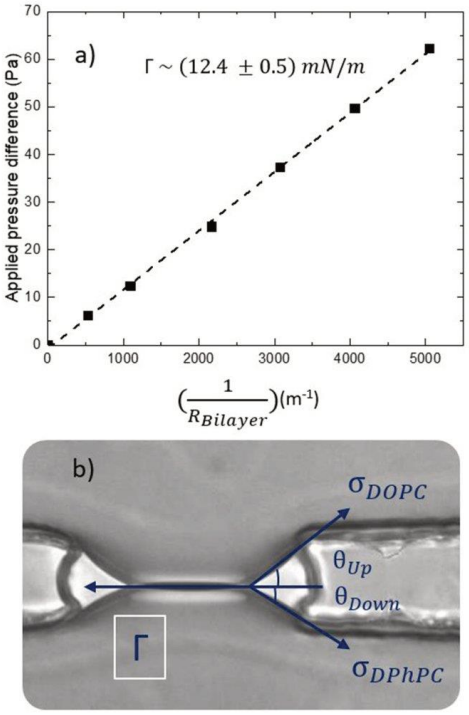

FIG. 6. (a) Applied pressure difference ΔP plotted against the corresponding bilayer curvature $1/R_{bilayer}$ for an asymmetric DOPC/DPhPC bilayer. The slope yields the bilayer tension Γ. (b) Optical micrograph of an asymmetric DOPC/DPhPC bilayer with indicated bilayer and surface tensions and the corresponding contact angle θ.

asymmetric DOPC/DPhPC bilayer and the obtained surface tensions of $\sigma_{DOPC} = (8.0 \pm 0.8)$ mN/m and $\sigma_{DPhPC} = (6.3 \pm 0.2)$ mN/m agree within experimental uncertainty and those obtained for the symmetric bilayers, which are listed in Table I.

IV. CONCLUSION

It was demonstrated that the freestanding fluid bilayer could be produced at a desired location in a microfluidic device. This microfluidic approach allows for good optical and electrophysiological accessibility, as well as precise monitoring of ongoing processes; thus, it combines several desired features in order to explore model membranes. In particular, we demonstrated that, by using a pressure-controlled system, the lifetime of a bilayer could be increased massively (to approximately 6 h) by balancing the oil drainage in a PDMS chip.

Applying controlled pressure differences across such a bilayer combined with the superior lifetime, we showed that this system can be used to measure simultaneously the surface tensions of lipid decorated oil–water interfaces, and the bilayer tension from a single experiment. The experimental error from this approach is clearly reduced with respect to known standard measurements as shown in Table I. Moreover, besides measuring the surface tension and membrane tensions for the symmetric bilayer, we extended this method to measure surface and bilayer tensions of the asymmetric lipid bilayer.

For the presented measurements, we restricted to the case of lipids in a fluid phase. However, we assume that the asymmetric lipid bilayer with a gel/fluid composition may also be formed and analyzed in the future with our method, provided they are sufficiently stable during bending. Additionally, the increased bilayer lifetime combined with the controlled bilayer curvature is opening new possibilities like the investigation of biological processes that require the extended experimental time scales or the protein–lipid interactions as functions of a well-defined bilayer curvature such as mechano-sensitive channels.

ACKNOWLEDGMENTS

All the authors acknowledge funding from the German Science Foundation within the SFB1027, "Physical modeling of non-equilibrium processes in biological systems" (Project B4).

REFERENCES

[1]T. Osaki and S. Takeuchi, "Artificial cell membrane systems for biosensing applications," Anal. Chem. **89**(1), 216–231 (2016).
[2]L. Liu, C. Yang, K. Zhao *et al.*, "Ultrashort single-walled carbon nanotubes in a lipid bilayer as a new nanopore sensor," Nat. Commun. **4**, 2989 (2013).
[3]G. F. Schneider and C. Dekker, "DNA sequencing with nanopores," Nat. Biotech. **30**, 326–328 (2012).
[4]C. E. Ashley, E. C. Carnes, G. K. Philips, D. Padilla, P. N. Durfee, P. A. Brown, T. N. Hanna, J. Liu, B. Philips, M. B. Carter, N. J. Carroll, X. Jiang, D. R. Dunphy, Ch. L. Willman, D. N. Petsev, D. G. Evans, A. N. Parikh, B. Chackerian, W. Wharton, D. S. Peabody, and C. J. Brinker, "The targeted delivery of multicomponent cargos to cancer cells by nanoporous particle-supported lipid bilayers," Nat. Mater. **10**, 389–397 (2011).
[5]T. Lian and R. H. Ho, "Trends and developments in liposome drug delivery systems," Pharm. Sci. **90**(6), 667–680 (2001).
[6]A. Sumino, T. Dewa, M. Kondo, T. Morii, H. Hashimoto, A. T. Gardiner, R. J. Cogdell, and M. Nango, "Selective assembly of photosynthetic antenna proteins into a domain-structured lipid bilayer for the construction of artificial photosynthetic antenna systems: Structural analysis of the assembly using surface plasmon resonance and atomic force microscopy active transport of Ca^{2+} by an artificial photosynthetic membrane," Langmuir **27**(3), 1092–1101 (2011).
[7]I. M. Bennett, H. M. V. Farfano, F. Bogani, A. Primak, P. A. Liddell, L. Otero, L. Sereno, J. J. Silber, A. L. Moore, Th. A. Moore, and D. Gust, "Active transport of Ca^{2+} by an artificial photosynthetic membrane," Nature **420**, 398–401 (2002).
[8]A. D. Miller, "Cationic liposomes for gene therapy," Angew. Chem. Int. Ed. **37**, 1768–1785 (1998).
[9]E. T. Castellana and P. S. Cremer, "Solid supported lipid bilayers: From biophysical studies to sensor design," Surf. Sci. **61**(10), 429–444 (2006).
[10]P. S. Cremer and S. G. Boxer, "Formation and spreading of lipid bilayers on planar glass supports," J. Phys. Chem. B **103**, 2554–2559 (1999).
[11]T. Ide and T. Ichikawa, "A novel method for artificial lipid bilayer formation," Biosens. Bioelectron. **21**(4), 672–677 (2005).

[12]R. S. Ries, H. Choi, R. Blunck, F. Bezanilla, and J. R. Health, "Black lipid membranes: Visualizing the structure, dynamics, and substrate dependence of membranes," J. Phys. Chem. B **108**, 16040–16049 (2004).
[13]R. Zeineldin, J. A. Last, A. L. Slade, L. K. Ista, P. Bisong, M. J. O'Brien, S. R. J. Brueck, D. Y. Sasaki, and G. P. Lopez, "Using bicellar mixtures to form supported and suspended lipid bilayers on silicon chips," Langmuir **22**, 8163–8168 (2006).
[14]M. Bally, K. Bailey, K. Sugihara, D. Grieshaber, J. Voeroes, and B. Staedler, "Liposome and lipid bilayer arrays towards biosensing applications," Small **6**(22), 2481–2497 (2010).
[15]X. Li, K. G. Klemic, M. A. Reed, and F. J. Sigworth, "Microfluidic system for planar patch clamp electrode arrays," Nano Lett. **6**(4), 815–819 (2006).
[16]K. Kamiya, T. Osaki, K. Nakao, R. Kawano, S. Fujii, N. Misawa, M. Hayakawa, and S. Takeuchi, "Electrophysiological measurement of ion channels on plasma/organelle membranes using an on-chip lipid bilayer system," Nature **8**, 17498 (2018).
[17]M. S. Khan, N. S. Dosoky, and J. D. Williams, "Engineering lipid bilayer membranes for protein studies," Mol. Sci. **14**(11), 21561–21597 (2013).
[18]C. E. Stanley, K. S. Elvira, X. Z. Niu, A. D. Gee, O. Ces, J. B. Edel, and A. J. deMello, "A microfluidic approach for high-throughput droplet interface bilayer (DIB) formation," Chem. Commun. **46**(10), 1565–1776 (2010).
[19]H. Bayley, B. Cronin, A. Heron, M. A. Holden, W. Hwang, R. Syeda, J. Thompson, and M. Wallace, "Droplet interface bilayers," Mol. Biosyst. **4**(12), 1191–1208 (2008).
[20]M. A. Nguyen, B. Srijanto, C. P. Collier, S. T. Retterer, and S. A. Sarles, "Hydrodynamic trapping for rapid assembly and *in situ* electrical characterization of droplet interface bilayer arrays," Lab Chip **16**(18), 3576–3588 (2016).
[21]N. E. Barlow, G. Bolognesi, S. Haylock, A. J. Flemming, N. J. Brooks, L. M. C. Barter, and O. Ces, "Rheological droplet interface bilayers (rheo-DIBs): Probing the unstirred water layer effect on membrane permeability via spinning disk induced shear stress," Nature **7**, 17551 (2017).
[22]J. R. Thompson, A. J. Heron, Y. Santoso, and M. I. Wallace, "Enhanced stability and fluidity in droplet on hydrogel bilayers for measuring membrane protein diffusion," Am. Chem. Soc. **7**(12), 3875–3878 (2007).
[23]J. B. Fleury, O. Claussen, S. Herminghaus, M. Brinkmann, and R. Seemann, "Mechanical stability of ordered droplet packings in microfluidic channel," Appl. Phys. Lett. **99**, 244104 (2011).
[24]U. D. Schiller, J. B. Fleury, R. Seemann, and G. Gompper, "Collective waves in dense and confined microfluidic droplet arrays," Soft Matter **11**, 5850–5861 (2015).
[25]N. Malmstadt, M. A. Nash, R. F. Purnell, and J. J. Schmidt, "Automated formation of lipid-bilayer membranes in a microfluidic device," Nano Lett. **6**(9), 1961–1965 (2006).
[26]J. N. Vargas, R. Seemann, and J. B. Fleury, "Fast membrane hemifusion via dewetting between lipid bilayers," Soft Matter **10**, 9293–9299 (2014).
[27]S. Thutupalli, J. B. Fleury, A. Steinberger, S. Herminghaus, and R. Seemann, "Why can artificial membranes be fabricated so rapidly in microfluidics," Chem. Commun. **49**, 1443–1445 (2013).
[28]P. Heo, S. Ramakrishnan, J. Coleman, J. E. Rothman, J. B. Fleury, and F. Pincet, "Highly reproducible physiological asymmetric membrane with freely diffusing embedded proteins in a 3D-printed microfluidic setup," Small **10**, 1900725 (2019).
[29]S. Kalsi, A. M. Powl, B. A. Wallace, H. Morgen, and M. R. R. de Planque, "Shaped apertures in photoresist films enhance the lifetime and mechanical stability of suspended lipid bilayers," Biophys. J. **106**(8), 1650–1659 (2014).
[30]A. Hirano-Iwata, A. Oshima, H. Mozumi, Y. Kimura, and M. Niwano, "Stable lipid bilayers based on micro- and nano-fabrication," Anal. Sci. **28**(11), 1049–1057 (2012).
[31]D. B. Weibel, W. R. DiLuzo, and G. M. Whitesides, "Microfabrication meets microbiology," Nat. Rev. Microbiol. **5**(3), 208–218 (2007).
[32]G. J. Taylor, G. A. Venkatesan, C. P. Collier, and S. A. Sarles, "Direct *in situ* measurement of specific capacitance, monolayer tension, and bilayer tension in a droplet interface bilayer," Soft Matter **11**, 7592–7605 (2015).

Appendix (II) Photoactivation of Cell-Free Expressed Archaerhodopsin-3 in a Model Cell Membrane

Authors: Navid Khangholi, Marc Finkler. Ralf Seemann, Albrecht Ott, Jean-Baptiste Fleury

Experimental Physics, Saarland University, 66123 Saarbrücken, Germany

DOI: 10.3390/ijms222111981

Author contributions:

Fabrication of microfluidic device, and running the experiments were conducted by N. Khangholi. The preparation of proteins, i.e. cell free expression of proteins, were conducted by M. Finkler. The interpretation of analysis were done by N. Khangholi, and M. Finkler. The paper was written by N. Khangholi, M. Finkler, R. Seemann, A. Ott, and J.B. Fleury. The research was directed by R. Seemann. And A. Ott.

N. Khangholi, and M. Finkler contributed equally.

Abstract:

Transmembrane receptor proteins are located in the plasma membranes of biological cells where they exert important functions. Archaerhodopsin (Arch) proteins belong to a class of transmembrane receptor proteins called photoreceptors that react to light. Although the light sensitivity of proteins has been intensely investigated in recent decades, the electrophysiological properties of pore-forming Archaerhodopsin (Arch), as studied in vitro, have remained largely unknown. Here, we formed unsupported bilayers between two channels of a microfluidic chip which enabled the simultaneous optical and electrical assessment of the bilayer in real time. Using a cell-free expression system, we recombinantly produced a GFP (green fluorescent protein) labelled as a variant of Arch-3. The label enabled us to follow the synthesis of Arch-3 and its incorporation into the bilayer by fluorescence microscopy when excited by blue light. Applying a green laser for excitation, we studied the electrophysiological properties of Arch-3 in the bilayer. The current signal obtained during excitation revealed distinct steps upwards and downwards, which we interpreted as the opening or closing of Arch-3 pores. From these steps, we estimated the pore radius to be 0.3 nm. In the cell-free extract, proteins can be modified simply by changing the DNA. In the future, this will enable us to study the photoelectrical properties of modified transmembrane protein constructs with ease. my work, thus, represents a first step in studying signalling cascades in conjunction with coupled receptor proteins.

International Journal of
Molecular Sciences

MDPI

Article

Photoactivation of Cell-Free Expressed Archaerhodopsin-3 in a Model Cell Membrane

Navid Khangholi †, Marc Finkler †, Ralf Seemann, Albrecht Ott * and Jean-Baptiste Fleury *

Experimental Physics and Center for Biophysics, Saarland University, 66123 Saarbrücken, Germany; navid.khangholi@physik.uni-saarland.de (N.K.); marc.finkler@uni-saarland.de (M.F.); r.seemann@physik.uni-saarland.de (R.S.)
* Correspondence: albrecht.ott@physik.uni-saarland.de (A.O.); jean-baptiste.fleury@physik.uni-saarland.de (J.-B.F.)
† Navid Khangholi and Marc Finkler contributed equally to this paper.

Abstract: Transmembrane receptor proteins are located in the plasma membranes of biological cells where they exert important functions. Archaerhodopsin (Arch) proteins belong to a class of transmembrane receptor proteins called photoreceptors that react to light. Although the light sensitivity of proteins has been intensely investigated in recent decades, the electrophysiological properties of pore-forming Archaerhodopsin (Arch), as studied in vitro, have remained largely unknown. Here, we formed unsupported bilayers between two channels of a microfluidic chip which enabled the simultaneous optical and electrical assessment of the bilayer in real time. Using a cell-free expression system, we recombinantly produced a GFP (green fluorescent protein) labelled as a variant of Arch-3. The label enabled us to follow the synthesis of Arch-3 and its incorporation into the bilayer by fluorescence microscopy when excited by blue light. Applying a green laser for excitation, we studied the electrophysiological properties of Arch-3 in the bilayer. The current signal obtained during excitation revealed distinct steps upwards and downwards, which we interpreted as the opening or closing of Arch-3 pores. From these steps, we estimated the pore radius to be 0.3 nm. In the cell-free extract, proteins can be modified simply by changing the DNA. In the future, this will enable us to study the photoelectrical properties of modified transmembrane protein constructs with ease. Our work, thus, represents a first step in studying signaling cascades in conjunction with coupled receptor proteins.

Keywords: Archaerhodopsin-3; lipid bilayer; microfluidics; cell-free gene expression

Citation: Khangholi, N.; Finkler, M.; Seemann, R.; Ott, A.; Fleury, J.-B. Photoactivation of Cell-Free Expressed Archaerhodopsin-3 in a Model Cell Membrane. *Int. J. Mol. Sci.* **2021**, *22*, 11981. https://doi.org/10.3390/ijms222111981

Academic Editor: Masoud Jelokhani-Niaraki

Received: 14 October 2021
Accepted: 3 November 2021
Published: 5 November 2021

1. Introduction

In biological cells, transmembrane proteins are embedded in the plasma membrane, composed of a lipid bilayer [1–3]. Certain transmembrane proteins act as receptors for external stimuli [4,5] such as light, mechanical stress, or the presence of specific molecular compounds [5–9]. Transmembrane receptor proteins transform the stimulus into signals that can be processed further downstream by the molecular machinery of the cell [2,4,10]. The stimulus produces structural or conformational changes in the transmembrane protein that will, for instance, result in an activation or deactivation of a specific ion channel, the release of a G protein (G protein-coupled receptors) or the activation of certain enzymes (enzyme-coupled receptors) [1,2,6,9,11–13].

Archaerhodopsin proteins (Arch) are among a class of transmembrane receptor proteins called photoreceptors that react to light [14,15]. Upon illumination with green light, Arch will undergo deprotonation of a Schiff base, resulting in proton pumping [16–19]. In this way, Arch actively transports protons through the membrane and out of the cell [14,18,19]. In vivo, the resulting proton gradient enables ATP synthases to produce ATP [18,20]. Photoreceptors typically consist of seven transmembrane helices and the chromophore retinal [16,18,21]. The structure of Arch corresponds to G protein-coupled

receptors that include rhodopsin. Because bacteriorhodopsin and Arch share similar structures and functions, their activation is assumed to be the same (see Figure 1c). Rhodopsin acts as a photoreceptor as well [1,15,22]. However, Arch acts as an ion channel, not as a G protein-coupled receptor. There are different kinds of Arch, which have slightly different properties [21]. Besides being photo active, Arch-3 fluorescence is also voltage sensitive [16,23], and it is often used in optogenetics as a voltage sensor [16,17]. To our knowledge, an electrophysiological characterization of Arch-3 has not yet been reported in the literature [18].

In this work, we present a new and simple microfluidic approach [24] to study the conducting properties of ion channels. We incorporated recombinantly produced Arch-3-EGFP into a free-standing lipid bilayer that mimics a biological membrane. A cell-free expression system was used for the production and reconstitution of Arch-3-EGFP. Such in vitro systems enable better control of various biochemical parameters and processes than in vivo systems [25–28]. They are regularly used to study gene circuits or reaction cascades [29–31]. In vitro, proteins, in the form of wild-type proteins or with modifications, can easily be produced recombinantly by the simple addition of the corresponding coding DNA [32–34]. Moreover, in vitro systems can mimic in vivo systems, allowing the transfer of results to the in vivo situation [35–37]. Using this approach, we report the first electrophysiological characterization of single Arch-3 channels in a model cell membrane. The method presented here (sketched in Figure 1) can be understood as a first step towards the further investigation of different signaling cascades.

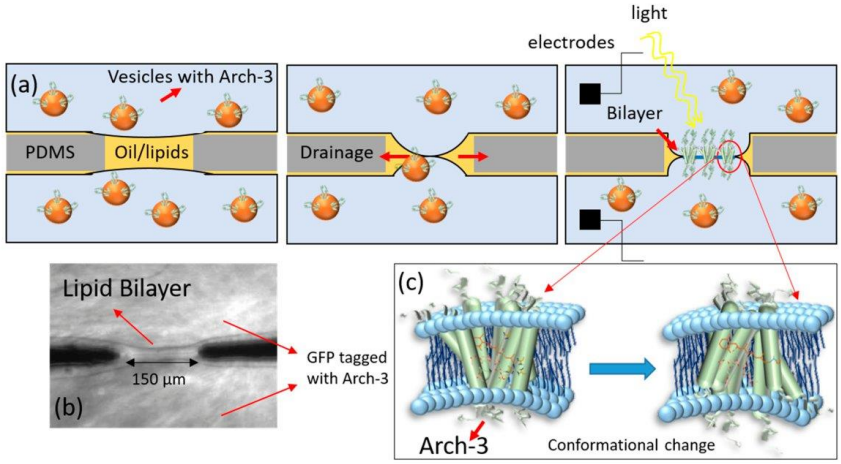

Figure 1. (**a**) A schematic of the formation of a lipid bilayer at the intersection of two microfluidic channels. First, the channel is filled with oil–lipid solution. Then, a cell-free expression reaction solution containing synthesized Arch-3-EGFP fused to the membrane of vesicles is injected into both channels. A remaining oil–filled lipid bilayer separates the two channels (left). Lipids from the oil phase and lipid vesicles with the inserted Arch-3-EGFP from the aqueous phase form a monolayer at both oil–water interfaces. As oil drains into the PDMS, the two interfaces gently meet to form a lipid bilayer containing Arch-3-EGFP (middle). The visualization of the inserted Arch-3-EGFP is achieved by exciting EGFP with blue light. AgCl electrodes inserted into the microfluidic device are used for electrical measurements (right). (**b**) The image shows the fluorescent signal of the EGFP tag from Arch-3 at the site of the suspended bilayer; PDMS elements remain dark. (**c**) The image shows the conformational changes of Arch-3 upon light exposure mediated by the deprotonation of retinal. This results in proton pumping which can be detected using electrophysiological measurements (scheme based on channel rhodopsin, adapted from [22]).

2. Results and Discussion

A DOPC/DPhPC bilayer containing Arch-3-EGFP was formed in a microfluidic device as described in the method section and as sketched in Figure 1. To verify the formation of a lipid bilayer, electrophysiological measurements were performed by applying a potential difference of 20 mV between both channels containing the reaction solution. The lipid bilayer separated the two ion-conducting water reservoirs, whereas the water–oil–water sandwich acted as a capacitor. Measuring the capacitance of such a sandwich in real time enabled the detection of bilayer formation; the graph in Figure 2a shows the related data from our experiments. The initial signal fluctuating around 10 pF corresponds to the situation with two monolayers separated by a macroscopic oil layer. The jump in the capacitance signal corresponds to the formation of a bilayer, a so-called zipping process. The following gradual increase in the capacitance demonstrates the growth of the bilayer area. This is due to the drainage of the oil to the PDMS at the plateau border.

Hydrostatic control of the flows enabled us to keep the bilayer area fairly constant for 1 h. The fluorescent image of EGFP tagged to Arch-3 under blue illumination, as shown in Figure 1b, confirmed the presence of Arch-3-EGFP in the vicinity of the lipid bilayer. After switching the laser illumination from blue to green, Arch-3 was activated, and an ion current was detected across the suspended lipid bilayer in real time upon light stimulation. The graph in Figure 2b shows the current intensity as a function of time, measured in the absence of light and after a short (~10 s) exposure to green laser light (532 nm) at ~40 s. Before light exposure, the current stayed almost constant. During the light pulse, the electrical current peaked, which means that ions were passing through the protein. After a few minutes, the signal decayed to its initial value. We interpret this observation as the signature of light-induced activation and subsequent deactivation of Arch-3. According to the literature, in any type of a rhodopsin photocycle, the deprotonation of the Schiff base after light excitation occurs within a range of picoseconds [38,39]. The deprotonation opens the channel; however, the subsequent recovery of the Schiff base requires milliseconds to several seconds [38–41]. Until recovery, the channel remains open for protons to pass through. Fitting an exponential decay to the curve from the time it begins to fall gives a recovery time τ of about 84 s.

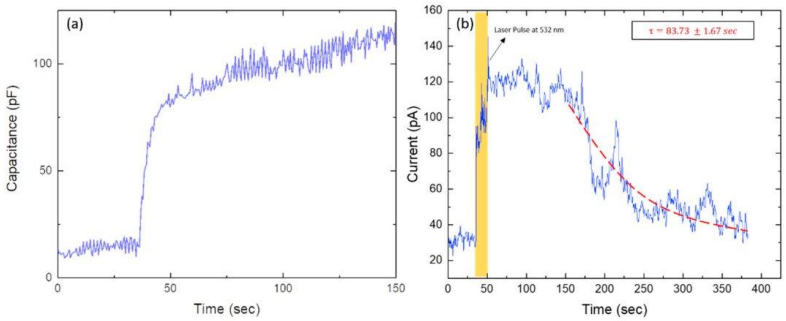

Figure 2. (**a**) Electrical capacitance as measured between the two microfluidic channels, separated by an oil phase (see Figure 1a) as a function of time. The signature of bilayer formation is the sudden increase in capacitance. (**b**) A real-time current recording of the bilayer containing Arch-3-EGFP. In the absence of light, we observe a current signal fluctuating around a constant value. The sudden jump in the current signal demonstrates the activation of Arch-3 caused by a green laser pulse applied to the bilayer at ~40 s $\leq$ t $\leq$ 50 s. The signal decays, with a time constant of ~84 s, to its initial dark value. The recovery time corresponds to the re-protonation of the Schiff base as reported in [38–40].

To characterize Arch-3 activation more deeply, we continuously exposed an Arch-3-containing bilayer to monochromatic light with a wavelength of 532 nm. During light exposure, we observed an overall increase in the conductance, which was composed of a

stepwise increase and decrease in the current signal, as shown in Figure 3a. This signal is caused by a combination of opening and closing channels and the simultaneous fusion of Arch-3-EGFP containing vesicles from the aqueous phase with the bilayer. If Arch-3-EGFP is added, the current recording will expose a positive jump. The individual current steps ΔI, as indicated by the red line in Figure 3a, were obtained using the "change point analysis" algorithm as part of the software Origin (Origin 2021b; OriginLab Corporation, Northampton, MA, USA). In total, over 300 steps were analyzed. The histogram shown in Figure 3b displays the frequency of certain current steps ΔI grouped within intervals of 2.5 pA. From the histogram, it can be seen that most of the jumps were in the range of (16.25 ± 6.25) pA, where the full width at half maximum was used to determine the experimental uncertainty. The obtained value is in excellent agreement with the value found in the literature for bacteriorhodopsin (BR) [42]. The large current steps ΔI causing the asymmetric distribution towards larger current steps in the histogram could be due to multiple channels in the bilayer simultaneously being activated or deactivated.

Although Arch-3 is a proton pump, protons can passively pass while the channel is open. Considering the current step with the highest probability, i.e., the maximum peak of the histogram at ΔI = 16.25 pA, and assuming that Arch-3 has a passive opening in the bilayer, we can determine the radius of a single Arch-3 channel from the relation [43]

$$r = \sqrt{\frac{l\Delta I}{\pi GCV}} \quad (1)$$

where $l \approx 3$ nm is the length of the protein assumed to be close to the thickness of the bilayer, ΔI = 16.25 pA is the amplitude of the typical current jump for one channel opening or closing, and $V = 20$ mV is the applied voltage. The molarity C of the reaction solution was converted from the osmolarity, which was measured as 1.02 osmol/kg. Because of the complexity of the reaction solution, the number of dissociable particles per molecule (n) was assumed to be two, as is the case for NaCl. Thus, the molarity was obtained as $C = 0.5$ M. Using this value, the molar conductivity results as G =18.4 S·M^{-1}·m^{-1}. The corresponding prediction of the pore radius of an Arch-3 channel, $r \approx (0.31 \pm 0.02)$ nm, is in excellent agreement with the radius of the pore of BR (0.4–1.1) nm [42] and of rhodopsin (0.45–0.7) nm [41], which also consist of seven transmembrane helices forming the same structure.

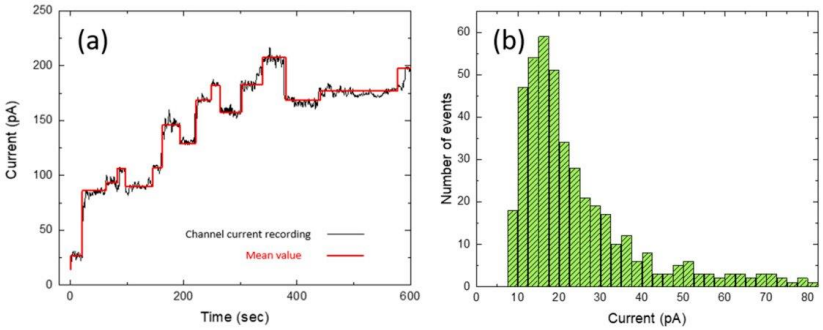

Figure 3. (**a**) Current signal as a function of time for an Arch-3-containing bilayer under continuous 532 nm laser illumination (black line). The red line was obtained by ''change point analysis" from the software Origin (Origin 2021b; OriginLab Corporation, Northampton, Massachusetts, USA). It shows the mean value of each current step. (**b**) The histogram shows the frequency of certain current steps grouped in intervals of 2.5 pA.

3. Conclusions

In this paper, we presented a simple and new microfluidic approach to investigate the electrophysiological properties of the recombinantly produced transmembrane protein Arch-3 inserted in a free-standing DOPC/DPhPC bilayer. By applying a voltage across such an Arch-3-containing DOPC/DPhPC bilayer, the light-induced opening of individual Arch-3 ion channels could be observed. The corresponding pore radius of the Arch-3 ion channel was determined to be (0.31 ± 0.02) nm, which is in excellent agreement with values found for similar protein pores.

The in vitro system described here presents the advantage of quick testing and prototyping of modified Arch-3, since only the DNA needs to be adapted. Moreover, even non-canonical amino acids can be incorporated [28,44,45]. Because G protein-coupled receptors involved in many signaling cascades exhibit a similar structure, we expect our work to be helpful for in vitro studies focusing on this kind of protein. This may pave the way for the creation of artificial signaling cascades.

4. Materials and Methods

4.1. Gene Expression

For gene expression, a commercially available cell-free expression system (*E. coli* T7 S30 Extract System for Circular DNA; Promega, Madison, Wisconsin, USA) was used. The plasmid in our experiments was VV020: WT Arch-3-EGFP in pET28b, a gift from Adam Cohen (Addgene plasmid # 58488; http://n2t.net/addgene:58488 (last accessed on 4 September 2021); RRID: Addgene_58488; Addgene, Watertown, Massachusetts, USA) [16]. The gene expression was performed in the presence of SUV (small unilamellar vesicles). For this, first a solution containing vesicles was prepared as follows: 400 µL of S30 Premix without Amino Acids, 50 µL of Amino Acid Mixture Minus Cysteine at 1 mM, 50 µL of Amino Acid Mixture Minus Leucine at 1 mM and 500 µL of ultrapure water were mixed. To this solution, 1 mg of DPhPC was added and sonicated three times, applying the continuous cycle of 4 s pulse, 4 s break for 4 min, and 2 min pause between each cycle. After that, the solution was put into the fridge to rest for 24 h.

Gene expression reactions were performed as follows: The components of the cell-free expression system were combined to obtain a "mastermix" containing 40 µL of S30 Premix without Amino Acids, 5 µL of Amino Acid Mixture Minus Cysteine at 1 mM, 5 µL of Amino Acid Mixture Minus Leucine at 1 mM and 30 µL of T7 S30 Extract System for Circular DNA. To this mastermix, 10 nM of plasmid DNA was added and filled up with vesicles solution to achieve a total reaction volume of 100 µL. The expression reaction was then incubated at 37 °C for 48 h. The synthesized Arch-3-EGFP was incorporated into the vesicles. Each reaction solution was directly injected into the microfluidic device after expression and could no longer be used after 24 h.

4.2. Lipid Preparation, and Device and Bilayer Fabrication

DOPC (1,2-dioleoyl-sn-glycero-3-phosphocholine), and DPhPC (1,2-diphytanoyl-sn-glycero-3-phosphocholine) were used for bilayer preparation. The lipids were from Avanti Polar Lipids (Avanti Polar Lipids, Birmingham, Alabama, USA). To prepare the oil–lipid solution, 5 mg of lipids (1:1 DOPC/DPhPC) were dissolved in 1 mL of pure squalene oil (Sigma-Aldrich, St. Louis, Missouri, USA) at 45 °C while undergoing continuous stirring for 3 h.

The microfluidic chip was produced by standard soft lithographic protocols and consisted of Sylgard 184 bonded to a glass slide, see e.g., ref. [24] for fabrication details. The chip was designed with two side-to-side rectangular channels with a width of 500 µm and height of 100 µm, forming an X geometry (see Figure 4).

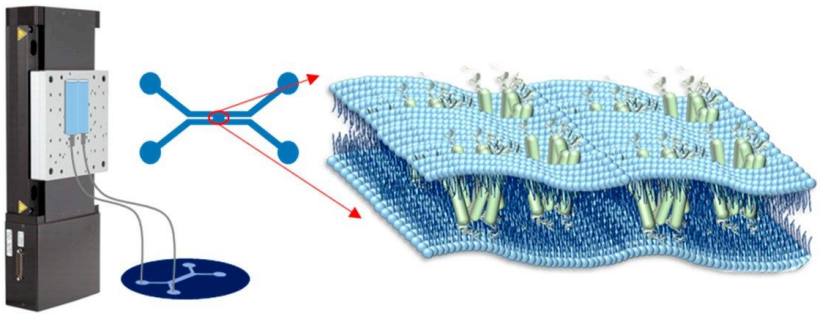

Figure 4. Design and structure of the microfluidic setup including the hydrostatic pressure system.

The membrane was formed across an orifice with a width of about 150 µm that connected the two parallel channels, as sketched in Figure 4. A hydrostatic pressure system was used to control the flow of the aqueous solution in the microfluidic chip [24]. The two inlets were connected to two syringes, which were fixed on a motorized stage, and the two outlets were left open. By adjusting the height of the motorized stage, positive or negative pressures could be applied to the channels causing the aqueous solution to move forward or backward.

For bilayer formation, the whole chip was first filled with the squalene oil containing dissolved lipids. Subsequently, the cell-free expression reaction solution containing synthesized Arch-3-EGFP proteins that were fused to vesicles was injected gently into both microfluidic channels, displacing the oil but leaving behind an oil inclusion at the orifice connecting the microfluidic channels. During this process the two oil–water interfaces were being decorated with a monolayer of lipids and Arch-3-EGFP. Due to the drainage of oil into the PDMS, the two lipid monolayers came into contact with each other, leading to the formation of a bilayer. While bilayer formation, the Arch-3-EGFP at the interface of the two monolayers fuses into the bilayer (sketched in Figure 1).

4.3. Microscope Setup and Electrical Measurements

An inverted epifluorescence microscope (Axio Observer Z1; Zeiss, Oberkochen, Germany) with 473 nm (blue) and 532 nm (green) laser illumination was used. As Arch-3 was tagged with enhanced green fluorescent protein (EGFP), we used the wavelength of 473 nm to excite the EGFP and monitor Arch-3 production (see Figure 2b). The electrical properties of the Arch-3-EGFP-containing bilayer were analyzed by electrophysiological measurements using a patch-clamp amplifier, EPC 10 USB (Heka Electronics, Reutlingen, Germany). For that purpose, Ag/AgCl electrodes were prepared by inserting a 5 cm-long silver wire into a borosilicate glass pipet containing 150 mM of NaCl electrolyte solution while applying 5 V for 30 min. The prepared electrodes were inserted into the inlets of the microfluidic device. The current passing through the bilayer was measured over time using an excitation signal with an amplitude of 20 mV and a time resolution of 100 ms.

Author Contributions: Conceptualization, N.K., M.F., R.S., A.O. and J.-B.F.; methodology, N.K., M.F. and J.-B.F.; software, N.K. and M.F.; validation, N.K. and M.F.; formal analysis, N.K. and M.F.; investigation, N.K. and M.F.; resources, R.S. and A.O.; data curation, N.K. and M.F.; writing—original draft preparation, N.K. and M.F. with help from A.O.; writing—review and editing, N.K., M.F., R.S., A.O. and J.-B.F.; visualization, N.K. and M.F.; supervision, R.S., A.O. and J.-B.F.; project administration, R.S., A.O. and J.-B.F.; funding acquisition, R.S., A.O. and J.-B.F. All authors have read and agreed to the published version of the manuscript.

Funding: This work was supported by the German Research Foundation (Projects B4, and C1 of CRC 1027) and, in part, by the Human Frontier Science Program (HFSP, RGP0037/2015).

Conflicts of Interest: The authors declare no conflict of interest.

References

1. Lefkowitz, R.J. Seven transmembrane receptors: Something old, something new. *Acta Physiol.* **2007**, *190*, 9–19. [CrossRef] [PubMed]
2. Gudermann, T.; Nürnberg, B.; Schultz, G. Receptors and G proteins as primary components of transmembrane signal transduction-Part 1. G-protein-coupled receptors: Structure and function. *J. Mol. Med.* **1995**, *73*, 51–63. [CrossRef] [PubMed]
3. Orwick-Rydmark, M.; Lovett, J.E.; Graziadei, A.; Lindholm, L.; Hicks, M.R.; Watts, A. Detergent-free incorporation of a seven-transmembrane receptor protein into nanosized bilayer lipodisq particles for functional and biophysical studies. *Nano Lett.* **2012**, *12*, 4687–4692. [CrossRef]
4. Zhulin, I.B.; Nikolskaya, A.N.; Galperin, M.Y. Common extracellular sensory domains in transmembrane receptors for diverse signal transduction pathways in Bacteria and Archaea. *J. Bacteriol.* **2013**, *185*, 285–294. [CrossRef] [PubMed]
5. Stock, J.B.; Stock, A.M.; Mottonen, J.M. Signal transduction in bacteria. *Nature* **1990**, *344*, 395–400. [CrossRef]
6. Árnadóttir, J.; Chalfie, M. Eukaryotic mechanosensitive channels. *Annu. Rev. Biophys.* **2010**, *39*, 111–137. [CrossRef]
7. Nagel, G.; Szellas, T.; Huhn, W.; Kateriya, S.; Adeishvili, N.; Berthold, P.; Ollig, D.; Hegemann, P.; Bamberg, E. Channelrhodopsin-2, a directly light-gated Cation-Selective Membrane Channel. *Proc. Natl. Acad. Sci. USA* **2003**, *100*, 13940–13945. [CrossRef]
8. Sandoval, P.J.; Santiago, J. In Vitro Analytical Approaches to Study Plant Ligand-Receptor Interactions. *Plant Physiol.* **2020**, *182*, 1697–1712. [CrossRef]
9. Stora, T.; Lakey, J.H.; Vogel, H. Ion-channel gating in transmembrane receptor proteins: Functional activity in tethered lipid membranes. *Angew. Chem. Int. Ed.* **1999**, *38*, 389–392. [CrossRef]
10. Simon, M.I.; Strathmann, M.P.; Gautam, N. Diversity of G proteins in Signal Transduction. *Science* **1991**, *252*, 802–808. [CrossRef]
11. Pierce, K.L.; Premont, R.T.; Lefkowitz, R.J. Seven-transmembrane receptors. *Nat. Rev. Mol. Cell Biol.* **2002**, *3*, 639–650. [CrossRef] [PubMed]
12. Bethani, I.; Skånland, S.S.; Dikic, I.; Acker-Palmer, A. Spatial organization of transmembrane receptor signalling. *EMBO J.* **2010**, *9*, 2677–2688. [CrossRef]
13. Haswell, E.S.; Phillips, R.; Rees, D.C. Mechanosensitive channels: What can they do and how do they do it? *Structure* **2011**, *19*, 1356–1369. [CrossRef] [PubMed]
14. Mukohata, Y.; Sugiyama, Y.; Ihara, K.; Yoshida, M. An Australian Halobacterium contains a novel Proton Pump Retinal Protein: Archaerhodopsin. *Biochem. Biophys. Res. Commun.* **1988**, *151*, 1339–1345. [CrossRef]
15. Ganapathy, S.; Kratz, S.; Chen, Q.; Hellingwerf, K.J.; de Groot, H.J.; Rothschild, K.J.; de Grip, W.J. Redshifted and Near-infrared Active Analog Pigments Based upon Archaerhodopsin-3. *Photochem. Photobiol.* **2019**, *95*, 959–968. [CrossRef]
16. Maclaurin, D.; Venkatachalam, V.; Lee, H.; Cohen, A.E. Mechanism of voltage-sensitive fluorescence in a microbial rhodopsin. *Proc. Natl. Acad. Sci. USA* **2013**, *110*, 5939–5944. [CrossRef]
17. Flytzanis, N.C.; Bedbrook, C.N.; Chiu, H.; Engqvist, M.K.; Xiao, C.; Chan, K.Y.; Sternberg, P.W.; Arnold, F.H.; Gradinaru, V. Archaerhodopsin variants with enhanced voltage-sensitive fluorescence in mammalian and *Caenorhabditis elegans* neurons. *Nat. Commun.* **2014**, *5*, 4894. [CrossRef] [PubMed]
18. Juarez, J.F.B.; Judge, P.J.; Adam, S.; Axford, D.; Vinals, J.; Birch, J.; Kwan, T.O.; Hoi, K.K.; Yen, H.-Y.; Vial, A. Structures of the archaerhodopsin-3 transporter reveal that disordering of internal water networks underpins receptor sensitization. *Nat. Commun.* **2021**, *12*, 629. [CrossRef]
19. El-Gaby, M.; Zhang, Y.; Wolf, K.; Schwiening, C.J.; Paulsen, O.; Shipton, O.A. Archaerhodopsin Selectively and Reversibly Silences Synaptic Transmission through Altered pH. *Cell Rep.* **2016**, *16*, 2259–2268. [CrossRef]
20. Mukohata, Y.; Sugiyama, Y.; Ihara, K. Photophosphorylation Elements in Halobacteria: An A-type ATP Synthase and Bacterial Rhodopsins. *J. Bioenerg. Biomembr.* **1992**, *24*, 547–553. [CrossRef]
21. Cao, Z.; Ding, X.; Peng, B.; Zhao, Y.; Ding, J.; Watts, A.; Zhao, X. Novel expression and characterization of a light driven proton pump archaerhodopsin 4 in a *Halobacterium salinarum* strain. *Biochim. Biophys. Acta* **2015**, *1847*, 390–398. [CrossRef]
22. Deisseroth, K.; Hegemann, P. The form and function of channelrhodopsin. *Science* **2017**, *357*, eaan5544. [CrossRef] [PubMed]
23. Gong, Y.; Li, J.Z.; Schnitzer, M.J. Enhanced Archaerhodopsin Fluorescent Protein Voltage Indicators. *PLoS ONE* **2013**, *8*, e66959. [CrossRef]
24. Khangholi, N.; Seemann, R.; Fleury, J.-B. Simultaneous measurement of surface and bilayer tension in a microfluidic chip. *Biomicrofluidics* **2020**, *14*, 024117. [CrossRef] [PubMed]
25. Shin, J.; Noireaux, V. An *E. coli* Cell-Free Expression Toolbox: Application to Synthetic Gene Circuits and Artificial Cells. *ACS Synth. Biol.* **2012**, *1*, 29–41. [CrossRef]
26. Finkler, M.; Ott, A. Bead-based assay for spatiotemporal gene expression control in cell-free transcription–translation systems. *Biotechniques* **2019**, *66*, 29–33. [CrossRef] [PubMed]
27. Finkler, M.; Kurt, Ö.; Grimm, F.; Hartz, P.; Ott, A. A bead-based method for the removal of the amino acid lysine from cell-free transcription-translation systems. *J. Biotechnol.* **2020**, *324S*, 100024. [CrossRef]
28. Finkler, M.; Ravanbodshirazi, S.; Grimm, F.; Hartz, P.; Ott, A. Full incorporation of the noncanonical amino acid hydroxylysine as a surrogate for lysine in green fluorescent protein. *Bioorg. Med. Chem.* **2021**, *41*, 116207. [CrossRef]
29. Sunami, T.; Hosoda, K.; Suzuki, H.; Matsuura, T.; Yomo, T. Cellular compartment model for exploring the effect of the lipidic membrane on the kinetics of encapsulated biochemical reactions. *Langmuir* **2010**, *26*, 8544–8551. [CrossRef]

30. Izri, Z.; Garenne, D.; Noireaux, V.; Maeda, Y.T. Gene Expression in on-Chip Membrane-Bound Artificial Cells. *ACS Synth. Biol.* **2019**, *8*, 1705–1712. [CrossRef]
31. Nevenzal, H.; Noach-Hirsh, M.; Skornik-Bustan, O.; Brio, L.; Barbiro-Michaely, E.; Glick, Y.; Avrahami, D.; Lahmi, R.; Tzur, A.; Gerber, D. A high-throughput integrated microfluidics method enables tyrosine autophosphorylation discovery. *Commun. Biol.* **2019**, *2*, 42. [CrossRef]
32. Silverman, A.D.; Karim, A.S.; Jewett, M.C. Cell-free gene expression: An expanded repertoire of applications. *Nat. Rev. Genet.* **2020**, *21*, 151–170. [CrossRef] [PubMed]
33. Katzen, F.; Chang, G.; Kudlicki, W. The past, present and future of cell-free protein synthesis. *Trends Biotechnol.* **2005**, *23*, 150–156. [CrossRef] [PubMed]
34. Shin, J.; Noireaux, V. Efficient cell-free expression with the endogenous *E. Coli* RNA polymerase and sigma factor 70. *J. Biol. Eng.* **2010**, *4*, 8. [CrossRef]
35. McSweeney, M.A.; Styczynski, M.P. Effective Use of Linear DNA in Cell-Free Expression Systems. *Front. Bioeng. Biotechnol.* **2021**, *9*, 715328. [CrossRef] [PubMed]
36. Senoussi, A.; Lee Tin Wah, J.; Shimizu, Y.; Robert, J.; Jaramillo, A.; Findeiss, S.; Axmann, I.M.; Estevez-Torres, A. Quantitative Characterization of Translational Riboregulators Using an in Vitro Transcription-Translation System. *ACS Synth. Biol.* **2018**, *7*, 1269–1278. [CrossRef] [PubMed]
37. Damiati, S.; Mhanna, R.; Kodzius, R.; Ehmoser, E.-K. Cell-Free Approaches in Synthetic Biology Utilizing Microfluidics. *Genes* **2018**, *9*, 144. [CrossRef]
38. Koch, M.; Dencher, N.; Oesterhelt, D.; Plöhn, H.; Rapp, G.; Büldt, G. Time-resolved X-ray diffraction study of structural changes associated with the photocycle of bacteriorhodopsin. *EMBO J.* **1991**, *10*, 521–526. [CrossRef]
39. Nakasako, M.; Kataoka, M.; Amemiya, Y.; Tokunaga, F. Crystallographic characterization by X-ray diffraction of the M-intermediate from the photo-cycle of bacteriorhodopsin at room temperature. *FEBS Lett.* **1991**, *292*, 73–75.
40. Dencher, N.A.; Dresselhaus, D.; Zaccai, G.; Büldt, G. Structural changes in bacteriorhodopsin during proton translocation revealed by neutron diffraction. *Proc. Natl. Acad. Sci. USA* **1989**, *86*, 7876–7879. [CrossRef]
41. Montal, M.; Darszon, A.; Trissl, H.W. Transmembrane channel formation in rhodopsin-containing bilayer membranes. *Nature* **1977**, *267*, 221–225. [CrossRef] [PubMed]
42. Radzwill, N.; Gerwert, K.; Steinhoff, H.J. Time-resolved detection of transient movement of helices F and G in doubly spin-labeled bacteriorhodopsin. *Biophys. J.* **2001**, *80*, 2856–2866. [CrossRef]
43. Heo, P.; Ramakrishnan, S.; Coleman, J.; Rothman, J.E.; Fleury, J.B.; Pincet, F. Highly Reproducible Physiological Asymmetric Membrane with Freely Diffusing Embedded Proteins in a 3D-Printed Microfluidic Setup. *Small* **2019**, *15*, 1900725. [CrossRef] [PubMed]
44. Worst, E.G.; Exner, M.P.; De Simone, A.; Schenkelberger, M.; Noireaux, V.; Budisa, N.; Ott, A. Cell-free expression with the toxic amino acid canavanine. *Bioorg. Med. Chem. Lett.* **2015**, *25*, 3658–3660. [CrossRef] [PubMed]
45. Worst, E.G.; Exner, M.P.; De Simone, A.; Schenkelberger, M.; Noireaux, V.; Budisa, N.; Ott, A. Residue-specific Incorporation of Noncanonical Amino Acids into Model Proteins Using an *Escherichia coli* Cell-free Transcription-translation System. *J. Vis. Exp.* **2016**, *114*, 54273. [CrossRef]

Appendix (III) An in vitro microfluidic assay for studying G-protein coupled photoreceptor signalling as derived from the retinal photo activated outer segment

Authors: Navid Khangholi, Marc Finkler, Sieun Sung, Mahsa Mohammadian, Albrecht Ott, Ralf Seemann

Experimental Physics, Saarland University, 66123 Saarbrücken, Germany

Author contributions:

Fabrication of microfluidic device, and running the experiments were conducted by N. Khangholi. The preparation of porcine outer segment from pig eyes were done by N. Khangholi, and M. Finkler. The interpretation of analysis was done by N. Khangholi, M. Finkler, and M. Mohammadian. The paper was written by N. Khangholi, M. Finkler, S. Sung, M. Mohammadian, A. Ott, and R. Seemann. The research was directed by A. Ott, and R. Seemann.

Abstract:

G-protein-coupled receptors (GPCRs) constitute the largest family of cross membrane signalling cell surface receptors. The photoreceptive GPCR Rhodopsin is present in rod cells from the retina of vertebrates. Upon excitation, the membrane-spanning GPCR changes its conformation to activate a certain number of G-proteins on the cytoplasmic side, stimulating enzymatic cGMP degradation causing cGMP gated channels to close and the cell membrane to electrically polarize. G-protein activation leads to enzymatic cGMP degradation causing cGMP gated channels to close and the cell membrane to electrically polarize. The polarization eventually leads to a neuronal response. Here we show that, within a microfluidic device, extracts from porcine photoreceptor outer segment cells incorporated into a synthetic, free standing lipid bilayer, reproduce the expected behaviour of the GPCR signalling network. The recorded electric current across the membrane demonstrates closure or opening of gated channels as a function of illumination. GMP analogues acting as inhibitors or activators cause the channels to remain in a closed or open state regardless of light exposure. Our work represents a first step towards in vitro studies and realizations of GPCR signalling in synthetic membranes bringing GPCR-based functional modules for synthetic biology within reach.

An in vitro microfluidic assay for studying G-protein coupled photoreceptor signalling as derived from the retinal photo activated outer segment

Navid Khangholi, Marc Finkler, Sieun Sung, Mahsa Mohammadian, Albrecht Ott, Ralf Seemann.

Experimental Physics and Center for Biophysics, Saarland University, 66123 Saarbrücken, Germany.

Navid.Khangholi@physik.uni-saarland.de (N.K.), Ralf.Seemann@physik.uni-saarland.de (R.S.)

Correspondence: Albrecht.ott@physik.uni-saarland.de (A.O.)

Abstract

G-protein-coupled receptors (GPCRs) constitute the largest family of cross membrane signalling cell surface receptors. The photoreceptive GPCR Rhodopsin is present in rod cells from the retina of vertebrates. Upon excitation, the membrane-spanning GPCR changes its conformation to activate a certain number of G-proteins on the cytoplasmic side, stimulating enzymatic cGMP degradation causing cGMP gated channels to close and the cell membrane to electrically polarize. G-protein activation leads to enzymatic cGMP degradation causing cGMP gated channels to close and the cell membrane to electrically polarize. The polarization eventually leads to a neuronal response. Here we show that, within a microfluidic device, extracts from porcine photoreceptor outer segment cells incorporated into a synthetic, free standing lipid bilayer, reproduce the expected behaviour of the GPCR signalling network. The recorded electric current across the membrane demonstrates closure or opening of gated channels as a function of illumination. GMP analogues acting as inhibitors or activators cause the channels to remain in a closed or open state regardless of light exposure. Our work represents a first step towards *in vitro* studies and realizations of GPCR signalling in synthetic membranes bringing GPCR-based functional modules for synthetic biology within reach.

Introduction

Transmembrane proteins are essential components of the cell. They span the entire width of the cell plasma membrane, enabling essential cellular functions such as signal transduction, transport of ions and molecules [1,2], sometimes acting as dynamic gatekeepers. G-Protein coupled receptors (GPCRs) represent the most diverse group of transmembrane receptors in eukaryotes. GPCRs play a critical role in signalling

Rhodopsin conformational change causing the G-protein transducin to become active, entailing closure of the gated channels via the canonical signalling pathway.

In a second experiment, the lipid bilayer with the POS stock solution was established in the dark. In these start conditions, we observed that the current intensity started to decrease as soon as the light was switched on. We attribute this, again, to the closure of the gated channel resulting from cGMP degradation. After a duration of about 500 s, the light was turned off again, and there was an increase in current (Figure 1b). We propose that GMP diffused from the bulk solution towards the membrane, thereby causing the channels to open again.

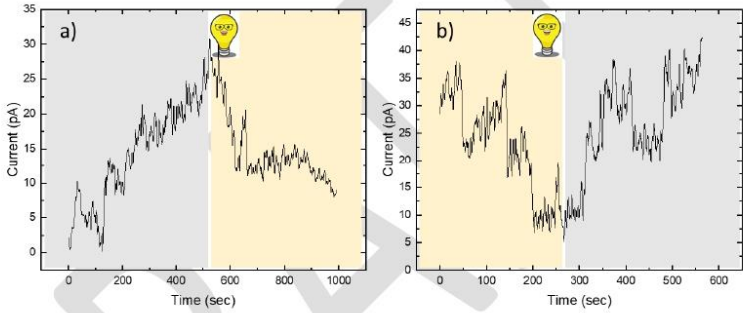

Figure 1. The current intensity across the bilayer as a function of time. a) The lipid bilayer is formed and exposed to the POS extract in the presence of light. The recording of electric current across the membrane starts once the light is switched off. After about 500 s, the light is switched on again. b) The lipid bilayer is formed in the absence of light. Current recording starts once the light is switched on to monitor the deactivation of the gated channels. After about 400 s, the light is switched off again. In both cases, a) and b), the channels are closing during illumination while they are opening in the dark.

To test for cGMP activity, we provided cGMP analogues by simply adding them to the POS stock. Otherwise, we conducted the same experiments as above. The analogues acted as inhibitors/activators that maintain the gated channels in a closed/open state. Figure 2 illustrates the impact of these analogues. The black line in the graph corresponds to the inhibitory cGMP analogue, resulting in no recorded current signal. Conversely, the red line in the graph represents activating cGMP analogues. The gated channels remain open for ion passage. This observation was independent of

pathways that regulate a wide range of cellular processes including hormone and neurotransmitter signalling [3-5].

Rhodopsin [6] is a GPCR that is present in rod cells of the retina. The corresponding GPCR pathway is crucial for visual information processing. Rhodopsin is activated by absorbing a photon causing a structural change that initiates a signalling process on the cytoplasmic side. There, the G-protein transducin binds to activated rhodopsin. This will entail an exchange of GDP for GTP in the transducin subunits (alpha, beta, and gamma). The alpha subunit then separates to activate the phosphodiesterase (PDE) to break down cyclic GMP (cGMP) to GMP. This reduction in cGMP level causes cGMP-dependent ion channels to close, increasing the cell membrane potential and eventually generating a neural signal [7-12].

In our study, we developed a model cell membrane using a microfluidic system to study the GPCR signalling pathway in vitro, under light exposure [13,14]. The experiments in this study were designed to observe how light-induced activation of GPCRs influences the level of cGMP and consequently the behaviour of gated ion channels in the lipid bilayer [15-18].

We observed changes in electrical activity across the model membrane that align well with the activation and deactivation of cGMP-gated ion channels. To our knowledge, these electrical analyses resulting from rhodopsin photoactivation has not been studied in vitro so far. Our work thus represents a pioneering achievement, providing a functional in vitro model of the entire GPCR cascade. We believe that the microfluidic, in vitro, functional realization of the entire GPCR cascade to be a first, important milestone for new, extended, and detailed in vitro studies of GPCR signalling.

Results and Discussion

In a first experiment, a lipid bilayer was formed and a small amount of a stock solution of an extract from the Porcine Outer Segment (POS) (see materials and methods) was injected into the microfluidic channels in the presence of light. The intensity of electric current across the bilayer was recorded simultaneously. When the light was switched off, we observed an increase in the current signal over time (Figure 1a). We interpret these changes as resulting from ions passing through cGMP-gated channels. After switching the light on, the current began to decrease. This can be easily interpreted by a

dark place. Tissues were collected under low-intensity red light. When handling an eye, delicately incise the front using the edge of a razor blade while maintaining a distance. Use the razor blade to bisect the anterior eyeball, allowing for the extraction of the lens and inversion of the eyecup to expose the retina. Hold the eyecup over a fingertip while gently scraping off the retina from the tapetum surface with the angled razor blade. Carefully cut the detached retina, identified by its pinkish layer, at the optic nerve head. Finally, store all collected retinas in two 50 ml tubes, each containing 15 ml of homogenization solution on ice.

Cyclic GMP analogues

For the analysis of the effect of cGMP level on the photoactivation, two cGMP analogues were purchased from Biolog life science institute. Rp-8-Br-cGMPS as inhibitor analogue and 8-pCPT-cGMP as activator analogue.

Experimental setup for lipid bilayer formation

The microfluidic device was manufactured using standard soft lithography protocols, whereby Sylgard 184 was moulded against a SU-8 master and bonded to a glass substrate. The protocol for fabricating the microfluidic device is explained elsewhere [13]. The microfluidic geometry consisted of two adjacent channels having a rectangular cross section, 500 µm wide and 100 µm high (Figure 3). The fluids were controlled by hydrostatic pressure [13,14], and the lipid bilayer was formed at the junction between the two channels with a width of 150 µm. Using the hydrostatic pressure control of the microfluidic device, the aqueous phase surrounding the lipid bilayer was replaced by the stock solution of the porcine outer segment (POS) after the formation of the bilayer.

Microscope setup and electrical measurement

UV-light exposure was conducted using an inverted microscope (Axio Observer Z1; Zeiss, Oberkochen, Germany). Analysis of electrical properties was performed using the patch-clamp technique with EPC 10 USB equipment (Heka Electronics, Reutlingen, Germany). Monitoring of the current passing through the bilayer was

illumination. We conclude that GPCR photoactivation depends on the cGMP in the POS extract.

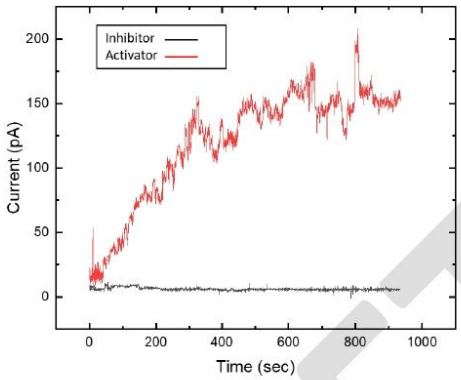

Figure 2. Current signal through a lipid bilayer with POS extract containing a cGMP analogue as a function of time. The black line shows the current signal in the presence of an inhibitory cGMP analogue; the current is constant, i.e. the cGMP gated channels remain closed. With activating cGMP analogues (red line), however, we observe an increase in the current signal; gated channels are opened. This is independent of the presence of light.

Materials and Methods

Lipid preparation

DOPC (1,2-dioleoyl-sn-glycero-3-phosphocholine), and DPhPC (1,2-diphytanoyl-sn-glycero-3-phosphocholine) were purchased from Avanti Polar Lipids. To prepare the mixture of lipid/oil solution, 5 mg of the lipids (1:2 DOPC/DPhPC) were dissolved in 1 mL of pure squalene oil (Sigma-Aldrich). The mixture was stirred at 45 °C for 3 h.

Porcine outer segment (POS) purification

The process of POS isolation demands a continuous working period of at least 12 hours. Here we give a short overview on the process, details can be found in Ref. [19]. After slaughtering, 80 fresh pig eyes were procured and stored immediately in a cool,

carried out over time using an excitation signal set at an amplitude of 20 mV and a time resolution of 100 ms.

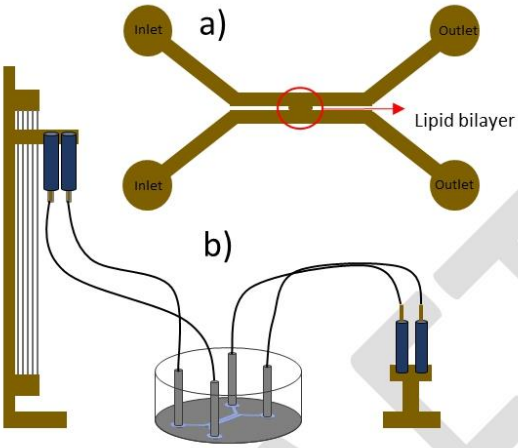

Figure 3. Schematic of microfluidic setup and lipid bilayer formation. a) Microfluidic device consisting of two side-to-side channels with a 150 µm gap in between where the lipid bilayer forms. b) Hydrostatic pressure setup for controlling the pressure inside the microfluidic device.

Conclusion

We applied a straightforward microfluidic approach to study Rhodopsin GPCR based photoactivation of transmembrane channels as observed by an electrical current across an artificially created free standing lipid membrane. By switching UV-light, the opening and closing of the cGMP gated ion channels from the photoactivated outer segment (POS) became clearly visible in the electric currents across the membrane. Using cGMP analogues, we showed that the observed photoactivation was most likely caused by cGMP degradation, as expected from the molecular workings of Rhodopsin G-protein coupled receptor (GPCR) photoactivation. We believe that our work represents an initial stride towards recreating the signalling cascade as GPCR cell signalling in biomimetic bilayers within a precisely controlled microfluidic setup.

13. N. Khangholi, R. Seemann, and J.-B. Fleury, 'Simultaneous measurement of surface and bilayer tension in a microfluidic chip', Biomicrofluidics, vol. 14, no. 2, p. 024117, Mar. 2020, doi: 10.1063/1.5137810.

14. N. Khangholi, M. Finkler, R. Seemann, A. Ott, and J.-B. Fleury, 'Photoactivation of Cell-Free Expressed Archaerhodopsin-3 in a Model Cell Membrane', IJMS, vol. 22, no. 21, p. 11981, Nov. 2021, doi: 10.3390/ijms222111981.

15. S. Beck et al., 'Synthetic Light-Activated Ion Channels for Optogenetic Activation and Inhibition', Front. Neurosci., vol. 12, p. 643, Oct. 2018, doi: 10.3389/fnins.2018.00643.

16. U. B. Kaupp and R. Seifert, 'Cyclic Nucleotide-Gated Ion Channels', Physiological Reviews, vol. 82, no. 3, pp. 769-824, Jan. 2002, doi: 10.1152/physrev.00008.2002.

17. G. Nagel et al., 'Channelrhodopsin-2, a directly light-gated cation-selective membrane channel', Proc. Natl. Acad. Sci. U.S.A., vol. 100, no. 24, pp. 13940-13945, Nov. 2003, doi: 10.1073/pnas.1936192100.

18. R. H. Kramer and E. Molokanova, 'Modulation of cyclic-nucleotide-gated channels and regulation of vertebrate phototransduction', Journal of Experimental Biology, vol. 204, no. 17, pp. 2921-2931, Sep. 2001, doi: 10.1242/jeb.204.17.2921.

19. C. Parinot, Q. Rieu, J. Chatagnon, S. C. Finnemann, and E. F. Nandrot, 'Large-Scale Purification of Porcine or Bovine Photoreceptor Outer Segments for Phagocytosis Assays on Retinal Pigment Epithelial Cells', JOVE, no. 94, p. 52100, Dec. 2014, doi: 10.3791/52100.

13. N. Khangholi, R. Seemann, and J.-B. Fleury, 'Simultaneous measurement of surface and bilayer tension in a microfluidic chip', Biomicrofluidics, vol. 14, no. 2, p. 024117, Mar. 2020, doi: 10.1063/1.5137810.

14. N. Khangholi, M. Finkler, R. Seemann, A. Ott, and J.-B. Fleury, 'Photoactivation of Cell-Free Expressed Archaerhodopsin-3 in a Model Cell Membrane', IJMS, vol. 22, no. 21, p. 11981, Nov. 2021, doi: 10.3390/ijms222111981.

15. S. Beck et al., 'Synthetic Light-Activated Ion Channels for Optogenetic Activation and Inhibition', Front. Neurosci., vol. 12, p. 643, Oct. 2018, doi: 10.3389/fnins.2018.00643.

16. U. B. Kaupp and R. Seifert, 'Cyclic Nucleotide-Gated Ion Channels', Physiological Reviews, vol. 82, no. 3, pp. 769-824, Jan. 2002, doi: 10.1152/physrev.00008.2002.

17. G. Nagel et al., 'Channelrhodopsin-2, a directly light-gated cation-selective membrane channel', Proc. Natl. Acad. Sci. U.S.A., vol. 100, no. 24, pp. 13940-13945, Nov. 2003, doi: 10.1073/pnas.1936192100.

18. R. H. Kramer and E. Molokanova, 'Modulation of cyclic-nucleotide-gated channels and regulation of vertebrate phototransduction', Journal of Experimental Biology, vol. 204, no. 17, pp. 2921-2931, Sep. 2001, doi: 10.1242/jeb.204.17.2921.

19. C. Parinot, Q. Rieu, J. Chatagnon, S. C. Finnemann, and E. F. Nandrot, 'Large-Scale Purification of Porcine or Bovine Photoreceptor Outer Segments for Phagocytosis Assays on Retinal Pigment Epithelial Cells', JOVE, no. 94, p. 52100, Dec. 2014, doi: 10.3791/52100.

Appendix (IV) Mechanics of biomimetic free-standing lipid membranes: Insights on lipid chemistry and bilayer elasticity

Authors: Alessandra Griffo, Carola Sparn, Fabio Lolicato, Friederike Nolle, Navid Khangholi, Ralf Seemann, Jean-Baptiste Fleury, Martin Brinkmann, Walter Nickel, Hendrik Hähl

Department of Experimental Physics, Saarland University, Saarbrücken, Germany

Center for Biophysics, Experimental Physics, Saarland University, Saarbrücken, Germany

Biophysical Engineering Group, Max Planck Institute for Medical Research, Heidelberg, Germany

Heidelberg University Biochemistry Center, Heidelberg, Germany

DOI: 10.1101/2023.08.21.554126

Author contributions:

The experiments were designed and conducted by A. Griffo. The microfluidic experiments were assisted by F. Nolle, N. Khangholi, and J.B. Fleury. The vesicle production were done by C. Sparn. The scientific discussion and planning the project was done by W. Nickel. Mathematical model was chosen by M. Brinkmann. The design of the work, and data analysis were done by H. Hähl. The paper is written by all authors.

Abstract:

The creation of free-standing lipid membranes has been so far of remarkable interest to investigate processes occurring in the cell membrane since its unsupported part enables studies in which it is important to maintain cell-like physicochemical properties of the lipid bilayer, that nonetheless depend on its molecular composition. In this study, we prepare pore-spanning membranes that mimic the composition of plasma membranes and perform force spectroscopy indentation measurements to unravel mechanistic insights depending on lipid composition. We show that this approach is highly effective for studying the mechanical properties of such membranes. Furthermore, we identify a direct influence of cholesterol and sphingomyelin on the elasticity of the bilayer and adhesion between the two leaflets. Eventually, we explore the possibilities of imaging in the unsupported membrane regions. For this purpose, we investigate the adsorption and movement of a peripheral protein, the fibroblast growth factor 2, on the complex membrane.

Mechanics of biomimetic free-standing lipid membranes: Insights on lipid chemistry and bilayer elasticity

Alessandra Griffo [ψ†Δ], Carola Sparn [⌂], Fabio Lolicato [⌂], Friederike Nolle [ψ†], Navid Khangholi [ψ†], Ralf Seemann [ψ], Jean-Baptiste Fleury [ψ†], Martin Brinkmann [†], Walter Nickel [⌂], Hendrik Hähl [ψ†]**

[†]*Department of Experimental Physics, Saarland University, Saarbrücken, Germany*

[ψ]*Center for Biophysics, Experimental Physics, Saarland University, Saarbrücken, Germany*

[Δ]*Biophysical Engineering Group, Max Planck Institute for Medical Research, Heidelberg, Germany*

[⌂]*Heidelberg University Biochemistry Center, Heidelberg, Germany*

**Corresponding authors (Alessandra.griffo@mr.mpg.de; h.haehl@physik.uni-saarland.de)*

Abstract

The creation of free-standing lipid membranes has been so far of remarkable interest to investigate processes occurring in the cell membrane since its unsupported part enables studies in which it is important to maintain cell-like physicochemical properties of the lipid bilayer, that nonetheless depend on its molecular composition. In this study, we prepare pore-spanning membranes that mimic the composition of plasma membranes and perform force spectroscopy indentation measurements to unravel mechanistic insights depending on lipid composition. We show that this approach is highly effective for studying the mechanical properties of such membranes. Furthermore, we identify a direct influence of cholesterol and sphingomyelin on the elasticity of the bilayer and adhesion between the two leaflets. Eventually, we explore the possibilities of imaging in the unsupported membrane regions. For this purpose, we investigate the adsorption and movement of a peripheral protein, the fibroblast growth factor 2, on the complex membrane.

1.0 Introduction

Lipid membranes form the cell membrane of almost all living organisms, such as eukaryotic cells, some prokaryotes, and several viruses. The membrane's ability to separate intracellular and extracellular ionic media makes it a functional capacitor that confines cells and organelles and regulates multiple translocation mechanisms[1]. Together with the capacitive function, a set of physical properties of lipid membranes, including elasticity, tension, and curvature[2], strongly affects many of the processes that are involved across the membrane. Examples are endocytosis, exocytosis, or conformational reshaping

of proteins embedded in membranes[3]. Also phenomena occurring at the protein-lipid interface as protein binding[4], oligomerization and insertion depend on the physical properties of lipid membranes and on their dynamic nature, which comprises processes, as e.g., curvature fluctuations and diffusion. Supported lipid bilayers (SLBs) have been, so far, for their stability, a versatile and demanded setup to easily assess a wide range of information[5]. The presence of the supporting substrate sacrifices, however, their dynamic nature and thus alters the reliability of observed processes occurring in and across the membrane[6,7]. Liposomes, as an alternative system to SLBs, allow to explore bilayer properties without disturbing these dynamic processes, yet suffer from limited experimental access[8].

Moreover, membrane properties and functions depend also on chemical composition and polydispersity of the lipids present in the cell membrane[9–12]. Biomimetic membranes should therefore be heterogeneous and polydisperse in lipid composition and resembling the mimicked living systems[2] as much as possible. Each lipid contributes to complex regulation mechanisms across the cell. Charged lipids, such as phosphatidylserine (PS) and Phosphatidylinositol 4,5-Bisphosphate $PI(4,5)P_2$, can regulate the binding affinity of proteins by electrostatic interactions [13,14]. Sterols and sphingolipids are in particular known to influence the arrangement of lipids[12,15] affecting both mechanical and chemical properties of lipid membranes and the resulting interactions with the surrounding environment. Also, cholesterol (CL) has been shown to significantly affect the bilayer stiffness. In addition, CL laterally segregates in domains in the outer leaflet of the membrane together with sphingomyelin, causing a considerable impact on the mechanics of the bilayer. Sphingomyelin (SM) has, due to its features, such as a high degree of saturation, asymmetric molecular structure, and extensive hydrogen-bonding properties, a very important role as a structural parameter in biological membranes. Furthermore, due to its tendency to interact with sterols, sphingomyelin largely regulates the cholesterol distribution within cellular membranes. More importantly, the tendency to form strong hydrogen bonds between sphingosine backbones of adjacent SM molecules is associated with an increase in compactness affecting the bilayer rigidiy[16,17].

In the current work, we prepared biomimetic membranes on substrates about 1 µm diameter circular holes. The pore-spanning membrane parts are a system between liposomes and SLBs featuring a better nanoscale observation than liposomes and a higher similarity to the natural situation than SLBs due to the absence of the solid support. These bilayer-model systems show water compartmentalization and bending rigidity similarly to liposomes[18], but are still accessible to atomic force microscopy (AFM) investigation, allowing to study a wider range of phenomena, e.g., monitoring the kinetics of protein activity on top of membranes[9,19 20]. In order to design a system close to the cell membrane situation, we used a complex plasma membrane-like composition (PMC) of PC:PE:PS:PI:CL:SM:$PI(4,5)P_2$ with ratios 33:10:5:5:30:15:2 for this study. Additionally, lipids from natural origin with a higher distribution

of the fatty acid chain lengths compared to otherwise mostly employed synthetic ones were chosen for our biomimetic membranes (**Figure 1**).

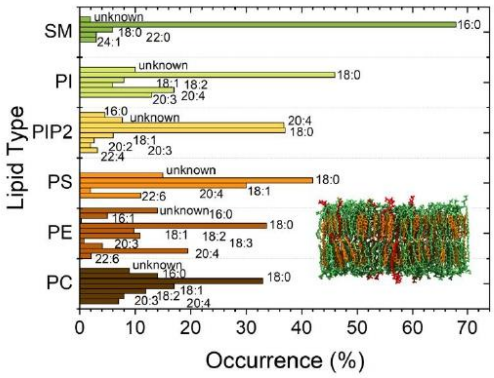

Figure 1. *Fatty acid distribution of each of the natural lipids employed in the current study. The bars marked with X:Y show for a certain lipid type the fraction with chain length (number of C atoms) of the fatty acids X and number of unsaturated bonds Y. Lipid types are sphingomyelin (SM), phosphatidylinositol (PI), phosphatidylinositol bisphosphate (PIP_2), phosphatidylserine (PS), phosphatidylethanolamine (PE), and phosphatidylcholine (PC). Data are adapted from Avanti Polar.*

We investigated the effect of cholesterol and sphingomyelin on the membrane mechanics with the methods described below. In detail, we determined bilayer pre-stress and stretching elasticity for these heterogeneous membranes via AFM indentation and by analysis of optical micrographs of membrane standing in a microfluidic channel, while tuning the cholesterol and sphingomyelin content.

2.0 Materials and Methods

2.1 Preparation of Giant Unilamellar Vesicles

Unsupported membranes have been produced by bursting giant unilamellar vesicles (GUVs) on top of mercapto-1-undecanol functionalized gold TEM grids (Plano GmbH, pore diameter of 0.8 and 1.2 µm), by adapting the methods described in the literature (**Figure 2A**)[21–24]. Gold-coated TEM grids were functionalized with thiol self-assembled monolayers (SAMs). For that, they were first cleaned and made more hydrophilic via UV-Ozone treatment and then left overnight in a 1 mM solution of mercapto-1-undecanol in ethanol. After that, they were rinsed with ethanol to remove the unbound molecules and let dry. The functionalization was tested by water contact angle (WCA) measurements.

For creating the GUVs, a plasma membrane-like lipid composition (PMC) consisting of 30 mol% cholesterol (CL), 15 mol% sphingomyelin (SM), 33 mol% phosphatidylcholine (PC), 10 mol%

phosphatidylethanolamine (PE), 5 mol% phosphatidylserine (PS), 5 mol% phosphatidylinositol (PI) and 2 mol % PI(4,5)P_2 (Avanti Polar Lipids, Alabaster, AL) and a PMC lacking of CL and SF (PMC-) were prepared in chloroform with 1.5 mM concentration. All membrane lipids were purchased from Avanti Polar Lipids. They have been purified from natural extracts [bovine liver (PC, PE, PI), egg chicken (SM), porcine brain (PS, PI(4,5)P_2), and ovine wool (CL)] and are therefore not uniform in alkyl chain length and unsaturated bond content (see **Figure 1**). The GUVs were generated by electroformation, according to the protocol of Steringer et al [22]. In detail, 5 µL of the lipids dissolved in chloroform solution was casted on platinum (Pt) wires, dried and immersed in sucrose solution (0.3 M). An AC-voltage of 1.5 V and a frequency of 10 Hz were applied for 40 min. After that, the frequency was reduced to 2 Hz for 20 minutes to allow the detachment of the GUVs from the Pt wires. The vesicles produced in this way (**Figure 2B**) were collected, stored at 4˚C, and used no longer than two days after production. Unsupported membranes were formed by diluting the stored GUV suspension in a ratio 1:50 in HEPES buffer.

2.2 Unsupported Membranes for AFM

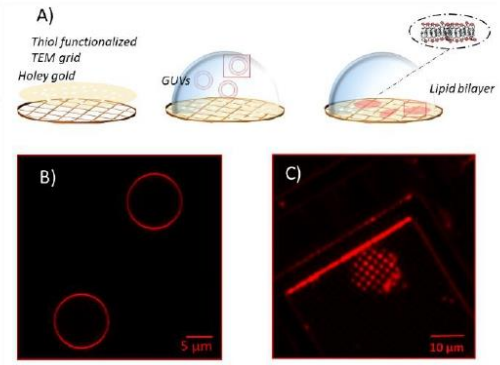

Figure 2. *A) Sketch of the process of GUVs bursting on top of hydrophilic functionalized TEM grids and corresponding fluorescence microscope images of GUVs B) before and C) after bursting on TEM grid. Lipids are stained with Rhod-PE.*

Unsupported membranes were formed by diluting the GUVs suspension in HEPES buffer 20 mM, 300 mM NaCl, 25 mM $MgCl_2$ and letting them burst, due to the difference in osmolarity between the sucrose inside the vesicle and the outer buffer, on the top of hydrophilic TEM grids mounted on a petri dish. Bursting of GUVs was checked by fluorescence microscopy in the presence of Rhod-PE, as reported in **Figure 2**. Eventually, for the AFM imaging and indentation experiments the solution was exchanged with imaging buffer [HEPES buffer 20 mM, 100 mM NaCl, 1 mM Ethylenediaminetetraacetic acid (EDTA)].

2.3 AFM imaging, force spectroscopy and data analysis

Atomic Force Microscopy (AFM) images and indentation experiments were acquired using a Dimension FastScanBio AFM (Bruker-Nano, Santa Barbara, CA, USA). MSNL-D probes (spring constant 0.03 N/m, resonance frequency 15 kHz, nominal tip radius 2 nm) were used for indentation experiments, while MSNL-D, SNL-D and PEAKFORCE-HIRS-F-B cantilevers (spring constant 0.03 N/m, 0.06 N/m and 0.12 N/m and resonance frequency 15 kHz, 18 kHz and 100 kHz, respectively, all probes purchased from Bruker AFM Probes, USA) were used for imaging. For each cantilever, the spring constant was calibrated by the thermal tune method. Peak Force Tapping® is used for imaging. During imaging, scan sizes varied from 500 nm to 20 µm. In the force curve measurements, the approaching and retracting curves were recorded with zero surface delay and a ramp size of 100–200 nm. For each indentation experiment, hundreds of force distance curves, (F-δ), were recorded on membrane standing holes; for these measurements, the homogenously coated holes were selected. All experiments were performed at room temperature (controlled at ca. 20 °C).

The data obtained from AFM indentation experiments were processed using custom-made MATLAB scripts for baseline correction and contact point determination, and the breakthrough force of the first rupture event was extracted. Pre-stress and elasticity of the membrane were determined by fitting a model to the data that was derived by Jin et al.[25]. The model is an analytical exact solution of the Föppl-von Karman approximation for the 'circular clamped elastic membrane under point load with pre-stress'. It can thus describe situations with any pre-stress value within the two limiting cases with negligible pre-stress, which is characterized by a cubic dependency of the indentation force F on the indentation depth δ, and very large pre-stress, where the force is a linear function of the indentation depth. It is, however, not possible to write the general (F-δ) dependency in explicit form. Fitting the model to the data was therefore done using a custom-made MATLAB script (see SI for details).

2.4 Free-standing membranes in microfluidic channel

We employed an H-junction geometry previously tested as a platform to produce stable membranes to form unsupported lipid membranes in microfluidics [26,27], cf. **Figure 3A** and **B**. To guarantee a good wettability for the continuous oily phase in the microfluidic device, PDMS is used as material. The microfluidic devices are fabricated from a silicon elastomer base and curing agent (PDMS, Sylgard 184, Dow Corning, USA) mixed in a ratio 10:1 and are casted on a silicon wafer, having structures produced by photolithography with a SU-8 photoresist, and cured for 6 h at 65 °C. After curing the PDMS elastomer, it is peeled off from the mold and exposed to nitrogen plasma (Diener electronic GmbH, Germany) together with an also PDMS coated glass slide. The treated PDMS device is sealed with the

glass slide and heated at 125 °C for 1–2 h to restore the hydrophobic properties of the PDMS. At the start of the experiment, this microfluidic device is filled with a continuous phase of squalene containing the lipids (5 mg/mL). Subsequently, two fingers of aqueous imaging buffer solution are injected into both channels of the device. Due to the wettability conditions, a thin squalene film remains between the buffer and the device walls, and the lipids contained in the squalene solution will decorate the oil-buffer interface forming a monolayer. A slow flow is created by hydrostatic pressure such that the lipid decorated oil-buffer interfaces are pushed through both channels and are brought in close vicinity at the junction. When the two monolayers touch each other, a zipping phenomenon driven by the intermolecular forces between the hydrophobic tails will occur, forming a bilayer (**Figure 3A, C-D**). Optical images of the bilayer formation occurring in the chip were acquired with Fluorescence Microscopy at 10x magnification. The angle θ between the two leaflets of the bilayer can be obtained by analyzing the optical micrographs.

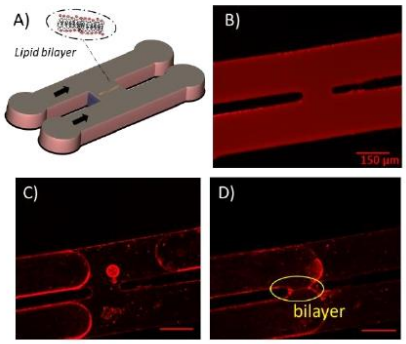

Figure 3. *A) Sketch of the design of the microfluidic setup featuring a H-junction. B–D) Fluorescence microscope images (Lipids are stained with Rhod-PE) monitoring the process of lipid bilayer formation from (B) initial flooding of the device with lipid-squalene solution, (C) slow injection of the buffer phase and (D) contacting the oil-buffer interfaces coated now with a lipid monolayer forming a bilayer at the contact.*

2.5 Interfacial tension γ and bilayer Tension Γ

Interfacial tension γ of a water/oil interface decorated with a monolayer of the lipid mixture is measured via the standard pendant drop method using a WCA goniometer (OCA 20, DataPhysics Instruments GmbH, Filderstadt, Germany). Briefly, a 1 mg/mL solution of lipid in squalene (0.858 g/cm^3) is transferred in an optical glass cuvette. A drop of imaging buffer solution (ca. 1 g/cm^3) is introduced from a needle that is dipped into the solution and the change of drop shape was observed over time, i.e. as a monolayer is formed at the interface. The droplet contour was fitted according to the Young-Laplace equation to obtain the interfacial tension γ. The decrease of γ due to the adsorption

of lipids to the newly created interface is recorded over 20–30 minutes until a plateau is reached, denoting the interfacial tension of the monolayer decorated interface.

From the values of the interfacial tension γ and the bilayer contact angle θ, the bilayer tension Γ can be calculated using Young's equation[28,29] :

$$\Gamma = 2\gamma\, cos\theta \quad (1)$$

Although the bilayer tension Γ and the pre-stress in the spanned bilayer σ are, in principle, the same quantity, namely the in-plane stress in the bilayer, they are named differently here to clarify their different origin: as the preparation conditions are different, it is not expected to measure the same in-plane stress in both experimental setups. Particularly, the bilayer tension Γ in the microfluidic setup results from the interfacial tension γ and the adhesion energy ΔW between the two bilayer leaflets as $\Delta W = 2\gamma - \Gamma = 2\gamma(1 - \cos\theta)$. (2)

3.0 Results

Unsupported lipid membranes with PM-like composition (PMC) or with a PM-like composition without CL and SM molecules (PMC⁻) spanning hydrophilic coated TEM grids (pore diameter 1.2 µm and 0.8 µm) were formed. AFM scans (**Figure 4**) revealed the presence of membranes over the selected spots. The AFM cross sections (**Figure 4b** and **4c**) show that the membrane covers the rim around the hole, which has a height of ca. 20 nm, and is recessed inside the hole below the actual substrate's surface to a depth of ca. 70–100 nm.

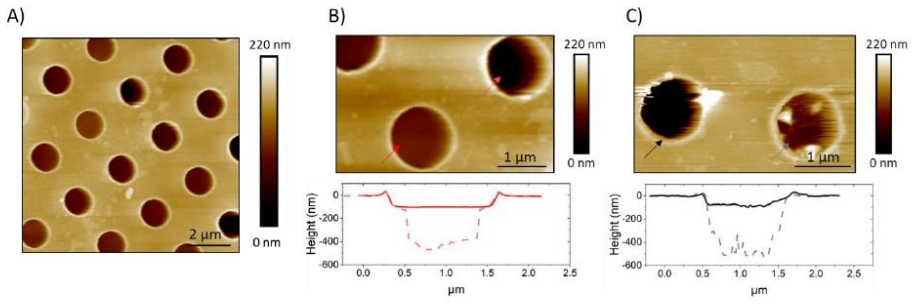

Figure 4. *AFM images showing PMC (A, B) and PMC⁻ (C) lipid membranes spanning holes in a functionalized Au-grid. Section analysis in B and C show intact (red and black) and broken (light red and gray dashes) membranes respectively for PMC and PMC⁻. Images were recorded at a PeakForce Setpoint of 280 pN. Additional images of PMC and PMC⁻ are reported in* ***Figure SI1****.*

We performed AFM force-indentation (F-δ) measurements in the center of membrane-covered holes (**Figure 5A**). From these data, we extracted the three parameters of breakthrough force (BF), elastic modulus (E), and bilayer pre-stress (σ) in order to unraveled the effect of CL and SM on the mechanical properties of the PMC membranes. BF is defined as the maximum force the membrane can withstand before it ruptures, indicated by an abrupt decrease in force. It can be correlated to the packing density of lipids in the membrane[30]. The F-δ curves reported in **Figure 5A** show a nonlinear response in the region between the *snap in/contact point*, which is due to tip-surface interactions like capillary forces, and the BF point. This region was fitted (green dashed lines) with a model from non-linear elastic theory of membranes[25,25] (**see SI**) enabling an estimation of both the elastic modulus E of the bilayer and its pre-stress σ.

The histograms shown in **Figure 5B** are a collection of BFs from PMC and PMC$^-$ membranes. They exhibit peaks that are fitted by Gaussian functions centered at (366 ± 7) pN for PMC and at (146 ± 9) pN for PMC$^-$.

In **Figure 5C**, E values obtained from the fitting procedure are plotted. Since no dependency on the hole radius was observed, we combined data from membranes spanning holes of 0.8 µm and 1.2 µm diameter. The maximum indentation depth reached in the experiment affects, however, the accuracy of the estimation of the Young's modulus. Since the stretching of the bilayer is more pronounced for larger indentations, the elastic modulus will be more important for the force response of the bilayer and thus, the estimation of E is improved. From a plot of the obtained E-values vs. the scaled maximum indentation depth on hole radius δ/R we decided for a threshold of δ/R = 0.03. Only values above this threshold were used for the estimation of the mean value of E. In **Figure 5C**, histograms of the E-value distributions are presented where the disregarded values with δ/R < 0.03 are displayed as lighter shaded bars showing that they are mainly high value outliers in the distributions. Values above this threshold (red and black bars of **Figure 5C**) are fitted with a Gaussian distribution with a peak value for the elasticity modulus E at (513 ± 19) MPa and (21.4 ± 0.5) MPa for the PMC (red squares) and PMC$^-$ (black squares) compositions, respectively.

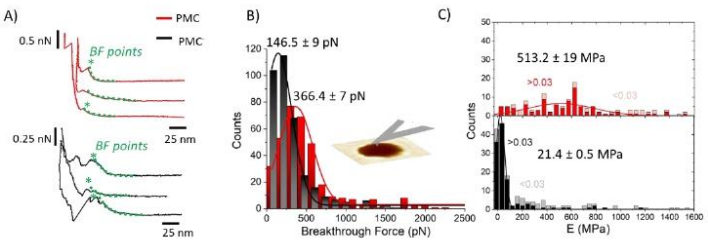

Figure 5. *A) F-δ curves on PMC (red) and PMC⁻ (black) membranes. B) Histograms of the breakthrough force values (BF) for PMC (red) and PMC⁻composition (black) fitted using a Gaussian function. C) Stacked histograms reporting the Young's modulus E for PMC (red squares for δ > 0.03 and pink for δ < 0.03) and PMC⁻ (black squares for δ > 0.03 and gray for δ < 0.03). Additional F-δ curves are reported in* ***Figure SI2****.*

Pre-stress values σ extracted from F-δ measurements that are shown in **Figure 5A** are reported in **Figure 6A**. We find that the value for σ is reduced from (5.2 ± 0.8) mN/m for the PMC membrane to (2.0 ± 0.2) mN/m for the PMC⁻ membrane. For qualitative comparison, the tension in the bilayer for both compositions was also determined from the contact angle θ of two contacted lipid monolayers in a microfluidic setup. Together with the interfacial tension γ of the monolayer, which was measured using the drop shape analysis of a pendant drop, and employing the Young Laplace equation (eq. 1)[26], bilayer tension values Γ of (13 ± 4) mN/m and (10 ± 1) mN/m (**Figure 6B**) were obtained for PMC and PMC⁻ membranes, respectively. These values relate via eq. (2) to adhesion energies ΔW between the sheets of (2.3 ± 0.2) mJ/m^2 and (1.4 ± 0.3) mJ/m^2.

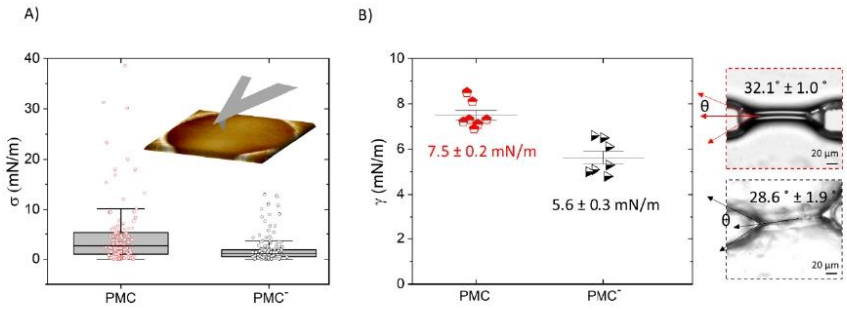

Figure 6. *A) Box plots of pre-stress σ (± SE) values recorded via AFM indentation measurements for PMC and PMC⁻ compositions. B) plots of interfacial tensions recorded via pendant drop measurements and optical micrographs of the membranes formed in a microfluidic (µFlu) chip showing respectively the interfacial tension γ and the bilayer angle θ for PMC and PMC⁻ compositions. θ and γ are used to calculate the bilayer tension Γ with the Young Laplace equation.*

In addition to the mechanistic insights, we used the imaging capabilities of the AFM to resolve the bilayer surface. Our choice to employ unsupported membranes for AFM investigation is guided by the need to construct platforms for protein observation and detection of its related processes, i.e., diffusion, kinetics assembly, pore forming mechanisms. **Figure 7** shows a series of AFM images of the free-standing part of the bilayer recorded while the protein fibroblast grow factor 2 (FGF2-GFP) was added to the solution above the bilayer, using a fluid cell setup. These AFM time-lapse frames show the adsorption of this peripheral protein across the bilayer. However, due to the fluidity of lipid

membranes and the difficulty of imaging standing portions of lipid membranes, it is hard to picture a clear statement from the reported images.

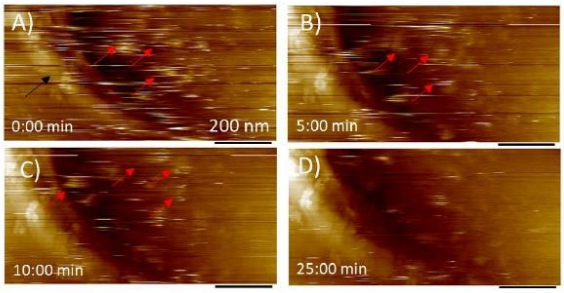

Figure 7. A-D) *Height AFM time-lapse frames recorded under flow while FGF2-GFP proteins are injected. FGF2-GFP proteins are observed overtime on the free-standing portion of the membrane. Scale bar is 200 nm and z height 80 nm. The black arrow points to the rim of the membrane spanned hole and red arrows point some of the proteins.*

4.0 Discussion

The described characterization allowed us to gain insight to the mechanics of membranes. The *BF* values of (366 ± 7) pN and at (146 ± 9) pN recorded by AFM for both unsupported PMC and PMC$^-$ membranes imply a difference in the compactness of the two membranes. The PMC membranes exhibit a higher breakthrough force, meaning that the membrane can resist the applied force more strongly. This observation matches quite well with the condensing effect of cholesterol[31], which is well known to regulate the membrane fluidity and produce an ordering of the lipids, leading to a decrease in its permeability[31–33]. Such insights have been suggested already by studies of SLBs[34–36] where information about the chemical composition of the membrane, its lipid packing, and the surrounding environment were gained from the *BF*. Sullan et al.[37] found that an increase of the *BF* was observed in the SM/Chol-enriched liquid-ordered domains (Lo) compared with the DOPC-enriched fluid-disordered phase (Ld). While the *BF* values they reported for SLBs were in the nN-range, our results for free-standing membranes fall, however, in the pN-range. Such differences are reasonably explained by the absence of a solid support. In our setup, the applied stress from the AFM cantilever causes a stretching of the membrane that, in turn, causes a reduction of the packing density until the inter-molecular distances are large enough to let the bilayer rupture at the *BF* point. In the SLB, the AFM tip has to push the molecules in order to punch through the bilayer, inducing an even higher packing density in the surrounding.

A closer insight into the mechanics of PMC lipid membranes and into the interplay of cholesterol and sphingomyelin can be obtained by extracting the stretching elasticity of the bilayer from the F-δ curves. Therefore, a theoretical description derived from the von the Karman Föppel model of elastic membranes was used. For a clamped elastic membrane under a central point load, a linear relation between force and indentation is predicted if the indentation is small and the pre-stress is not negligible. For higher indentations and small or negligible pre-stress, stretching of the membrane dominates and leads to a cubic relation depending on the elasticity for the membrane[38], $F \propto E\,\delta^3$. As an approximation, a linear superposition of those limiting behavior descriptions is used in similar studies[39–41]

$$F = \sigma\pi\delta + \frac{\pi E h}{3R^2}\delta^3 \tag{3}$$

where h is the bilayer thickness, here assumed as 6.7 nm for PMC membranes and as 6.0 nm for PMC$^-$ membranes[42,43], R the hole radius, E the elastic modulus and σ the pre-strain of the membrane. Note, however, that in this setup the membrane is stretched laterally and thus only its lateral 2D elasticity E^{2D} is probed. E^{2D} is related to E as $E^{2D} = E \cdot h$ under the assumption of an isotropic material, which is not strictly valid in this case. We nevertheless state the values for E for a better comparability.

In the data of this study (**Figure SI3 and SI4**), both behaviors can be observed: a constant slope for low indentations and a deviation from the linear dependency for higher indentations of $\delta/R \gtrsim 0.03$. Therefore, the accuracy with which E is determined increases with higher δ. Physically, this reflects the notion that the more the membrane is indented, the more it is stretched, and the more important Young's modulus becomes.

Since the data of this study fall, however, mostly in the transition region between linear and cubic behavior, where the inaccuracy of the simple model is highest, we chose a slightly more complicated, yet analytically exact solution of the theoretical model by Jin et al.[25,44] (see SI for details). Data shown in **Figure 5C** and **6A** were obtained by fitting this model to the experimental F-δ curves. Compared to the approximation of eq (1), we obtained slightly lower values for E and σ as well as a lower scattering (a comparison between the approximate and exact solution of the model is reported in **Figure SI3**). The obtained elasticity values recorded upon membrane indentation vary from 10 to 1000 MPa. Thereby, lower elasticity values are found for higher maximum indentation depths, with the smallest near 100 and 30 MPa for PMC and PMC$^-$ membranes, respectively (**Figure SI3**). The latter values correspond to the maximum achievable membrane stretching.

The obtained results on membrane mechanics match with many works reported in literature[15,45] where the role of SM and CL is attributed to an increase in stiffness. Yet, in most of the studies elasticity of

membranes has been extensively probed for supported lipid bilayers and vesicles, but rarely for unsupported membranes. To enable a comparison with elasticity measurements from vesicle indentation[46,47], where normally the bending rigidity is probed, we calculated this property from our measurements via

$$Kc = \frac{Eh^3}{12\,(1-\nu^2)} \tag{4}$$

where ν is the Poisson ratio kept as 0.485[48], E the elastic modulus and h the membrane thickness. We find values of about $200*10^{-19}$ J and $9*10^{-19}$J at maximum indentation depths for PMC and PMC^- membranes, respectively. Such values are slightly above those typically reported in the literature for membranes not containing rigid molecules such as SM and CL [9,20,49] and could be attributed to the presence of rigid-like lipids such as SM and CL that increase the membrane rigidity. Our results report a remarkable membrane rigidity, which is even larger compared to cholesterol enriched membranes [15,50]. Sphingomyelin, in fact, increases the packing density of the membrane due to its hydrogen bond forming capacity with neighboring lipids[17]. Also, the $PI(4,5)P_2$ may cause, due to its conical shape, a stiffening of the membrane[15] and an increase of the lateral pressure in the acyl chain region[51].

Studies on tension and pre-stress instead have been carried out more extensively also for monodisperse and unsaturated lipids on unsupported membranes[21,23,52]. In the work of Kocun et al.[21], site specific force indentation experiments on porous substrates were performed to determine membrane tension as a function of lipid composition. Although they used a similar setup, their pure POPC or DOPC membranes showed only a linear force-indentation behavior, which did not allow for a determination of the bilayer's elasticity. They obtained, however, an apparent spring constant, which depends on the preparation-imposed pre-tension of the bilayer and is comparable to ($\sigma\pi$) in our analysis. They observed an increase in the apparent spring constant for DOPC membranes from about 1.0 mN/m to 3.5 mN/m after the addition of cholesterol, which matches well with our findings, where the addition of the two rigid-like components cholesterol and sphingomyelin led to a shift from 2 mN/m to about 5 mN/m. In the case of the spanned membrane, the tension of the membrane is influenced by the adhesion to the substrate surrounding the hole, where a higher adhesion should lead to a higher tension[53]. For the membranes in the microfluidic setup, the tension is directly given by the adhesion between the sheets via eq. (2). For both situations, a higher tension thus means an increase in adhesion; in one case, to the substrate and, in the other case, between the leaflets. It is interesting to note that the addition of CL and SM in the membrane leads, in both cases, to an increased adhesion. However, the ratio of this increase seems too large to be attributed solely to an increased molecular density in the bilayer.

Our observations shed light on the function of sterols and sphingolipids on more complex compositions presenting larger lipid heterogeneity and fatty acid distribution as the degree of unsaturation, and polydispersity can tune the properties usually attributed to CL and SM[45]. Previous studies showed that for certain proteins, i.e. the FGF2 used in our experiments, both binding and translocation are highly enhanced when cholesterol and sphingomyelin are present[54]. The underlying mechanism remains not entirely elucidated, but it's probable that variations in tension and the lipids' inherent properties play significant roles in this phenomenon.

5.0 Conclusions

The technology of membrane biomechanics is continuously in evolution and currently many systems are studied, from in vitro constructed liposomes[55], pore spanning membranes[35], synthetic cells[56] to entire cells[57], using a variety of techniques, including AFM, fluctuation spectroscopy and micropipette aspiration. In our study, we employed Atomic Force Microscopy, Atomic Force Indentation and less extensively also microfluidics, to achieve insights into mechanical properties, such as bilayer tension and elasticity, morphological features, and protein-membrane interaction studies on unsupported membranes. Starting from the pore spanning technology we used biomimetic lipid membranes for which we chose a plasma membrane-like composition from natural lipids, to shed light on the properties of complex membranes, which feature lipid heterogeneity and polydispersity. The focus was mainly on the role of cholesterol and sphingomyelin, for which there is still a lack of information. The shift in the values of elastic modulus, of the breakthrough force as well as in the adhesion energies between PMC and PMC^{-} shows how the combination of different bilayer components affects the compactness and the mechanics of the membranes. This led us to the conclusion that cholesterol and sphingomyelin increase membrane tension and rigidity even in more complex PMC compositions. Eventually, we propose the described unsupported membranes as an alternative to supported ones as model for systematic studies with more natural dynamics.

Author Contributions

A.G. performed the experiments and designed the work, F.N., N.K., J.-B. F. helped for the microfluidic experiments, C.S., F.L. helped in vesicle productions and W.N. supported the scientific discussion and in planning the project, M.B. helped in choosing the mathematical model, H.H. helped in the data analysis and designed the work. All the authors contributed to the manuscript writing. A.G. and H.H are shared corresponding authors.

Acknowledgements

This study was supported by the German Research Foundation in the framework of the CRC1027 (B2, B4), DFG Ni 423/10-1; WN, DFG LO 2821/1-1; FL, and Saarland University within the funding program Open Access Publishing and was conducted within the Max Planck School Matter to Life supported by the German Federal Ministry of Education and Research (BMBF) in collaboration with the Max Planck Society.

References

1. Golowasch, J. & Nadim, F. Capacitance, Membrane. in *Encyclopedia of Computational Neuroscience* (eds. Jaeger, D. & Jung, R.) 1–5 (Springer, 2013).
2. Kozlov, M. M. & Chernomordik, L. V. Membrane tension and membrane fusion. *Curr. Opin. Struct. Biol.* **33**, 61–67 (2015).
3. Anishkin, A., Loukin, S. H., Teng, J. & Kung, C. Feeling the hidden mechanical forces in lipid bilayer is an original sense. *Proc. Natl. Acad. Sci.* **111**, 7898–7905 (2014).
4. Hutchison, J. B., Mudiyanselage, A. P. K. K. K., Weis, R. M. & Dinsmore, A. D. Osmotically-induced tension and the binding of N-BAR protein to lipid vesicles. *Soft Matter* **12**, 2465–2472 (2016).
5. Hardy, G. J., Nayak, R. & Zauscher, S. Model cell membranes: Techniques to form complex biomimetic supported lipid bilayers via vesicle fusion. *Curr. Opin. Colloid Interface Sci.* **18**, 448–458 (2013).
6. Tero, R. Substrate Effects on the Formation Process, Structure and Physicochemical Properties of Supported Lipid Bilayers. *Materials* **5**, 2658–2680 (2012).
7. Yang, J. & Appleyard, J. The Main Phase Transition of Mica-Supported Phosphatidylcholine Membranes. *J. Phys. Chem. B* **104**, 8097–8100 (2000).
8. Berti, D., Caminati, G. & Baglioni, P. Functional liposomes and supported lipid bilayers: towards the complexity of biological archetypes. *Phys. Chem. Chem. Phys.* **13**, 8769–8782 (2011).

9. Faizi, H. A., Frey, S. L., Steinkühler, J., Dimova, R. & Vlahovska, P. M. Bending rigidity of charged lipid bilayer membranes. *Soft Matter* **15**, 6006–6013 (2019).

10. Seu, K. J., Cambrea, L. R., Everly, R. M. & Hovis, J. S. Influence of Lipid Chemistry on Membrane Fluidity: Tail and Headgroup Interactions. *Biophys. J.* **91**, 3727–3735 (2006).

11. Tiberti, M. L., Antonny, B. & Gautier, R. The transbilayer distribution of polyunsaturated phospholipids determines their facilitating effect on membrane deformation. *Soft Matter* **16**, 1722–1730 (2020).

12. Serral Gracià, R., Bezlyepkina, N., L. Knorr, R., Lipowsky, R. & Dimova, R. Effect of cholesterol on the rigidity of saturated and unsaturated membranes : fluctuation and electrodeformation analysis of giant vesicles. *Soft Matter* **6**, 1472–1482 (2010).

13. Steringer, J. P. *et al.* Key steps in unconventional secretion of fibroblast growth factor 2 reconstituted with purified components. *eLife* **6**, e28985 (2017).

14. Vorobyov, I. & Allen, T. W. On the role of anionic lipids in charged protein interactions with membranes. *Biochim. Biophys. Acta BBA - Biomembr.* **1808**, 1673–1683 (2011).

15. Steinkühler, J., Sezgin, E., Urbančič, I., Eggeling, C. & Dimova, R. Mechanical properties of plasma membrane vesicles correlate with lipid order, viscosity and cell density. *Commun. Biol.* **2**, 337 (2019).

16. Sullan, R. M. A., Li, J. K. & Zou, S. Direct Correlation of Structures and Nanomechanical Properties of Multicomponent Lipid Bilayers. 7 (2009).

17. Slotte, J. P. The importance of hydrogen bonding in sphingomyelin's membrane interactions with co-lipids. *Biochim. Biophys. Acta BBA - Biomembr.* **1858**, 304–310 (2016).

18. Delorme, N. & Fery, A. Direct method to study membrane rigidity of small vesicles based on atomic force microscope force spectroscopy. *Phys. Rev. E* **74**, 030901 (2006).

19. Faizi, H. A., Reeves, C. J., Georgiev, V. N., Vlahovska, P. M. & Dimova, R. Fluctuation spectroscopy of giant unilamellar vesicles using confocal and phase contrast microscopy. *Soft Matter* **16**, 8996–9001 (2020).

20. Dimova, R. Recent developments in the field of bending rigidity measurements on membranes. *Adv. Colloid Interface Sci.* **208**, 225–234 (2014).

21. Kocun, M., Lazzara, T. D., Steinem, C. & Janshoff, A. Preparation of Solvent-Free, Pore-Spanning Lipid Bilayers: Modeling the Low Tension of Plasma Membranes. *Langmuir* **27**, 7672–7680 (2011).

22. Steringer, J. P. *et al.* Phosphatidylinositol 4,5-Bisphosphate (PI(4,5)P2)-dependent Oligomerization of Fibroblast Growth Factor 2 (FGF2) Triggers the Formation of a Lipidic Membrane Pore Implicated in Unconventional Secretion. *J. Biol. Chem.* **287**, 27659–27669 (2012).

23. Heinemann, F. & Schwille, P. Preparation of Micrometer-Sized Free-Standing Membranes. *ChemPhysChem* **12**, 2568–2571 (2011).

24. Som, A. *et al.* Strong and Elastic Membranes via Hydrogen Bonding Directed Self-Assembly of Atomically Precise Nanoclusters. *Small* **18**, 2201707 (2022).

25. Jin, C., Davoodabadi, A., Li, J., Wang, Y. & Singler, T. Spherical indentation of a freestanding circular membrane revisited: Analytical solutions and experiments. *J. Mech. Phys. Solids* **100**, 85–102 (2017).

26. Khangholi, N., Seemann, R. & Fleury, J.-B. Simultaneous measurement of surface and bilayer tension in a microfluidic chip. *Biomicrofluidics* **14**, 024117 (2020).

27. Guo, Y., Werner, M., Seemann, R., Baulin, V. A. & Fleury, J.-B. Tension-Induced Translocation of an Ultrashort Carbon Nanotube through a Phospholipid Bilayer. *ACS Nano* **12**, 12042–12049 (2018).

28. Bibette, J., Calderon, F. L. & Poulin, P. Emulsions: basic principles. *Rep. Prog. Phys.* **62**, 969–1033 (1999).

29. Needham, D. & Haydon, D. A. Tensions and free energies of formation of 'solventless' lipid bilayers. Measurement of high contact angles. *Biophys. J.* **41**, 251–257 (1983).

30. Gumí-Audenis, B., Sanz, F. & Giannotti, M. I. Impact of galactosylceramides on the nanomechanical properties of lipid bilayer models: an AFM-force spectroscopy study. *Soft Matter* **11**, 5447–5454 (2015).

31. Hung, W.-C., Lee, M.-T., Chen, F.-Y. & Huang, H. W. The Condensing Effect of Cholesterol in Lipid Bilayers. *Biophys. J.* **92**, 3960–3967 (2007).

32. Róg, T., Pasenkiewicz-Gierula, M., Vattulainen, I. & Karttunen, M. Ordering effects of cholesterol and its analogues. *Biochim. Biophys. Acta BBA - Biomembr.* **1788**, 97–121 (2009).

33. Gumí-Audenis, B. *et al.* Structure and Nanomechanics of Model Membranes by Atomic Force Microscopy and Spectroscopy: Insights into the Role of Cholesterol and Sphingolipids. *Membranes* **6**, 58 (2016).

34. Garcia-Manyes, S. & Sanz, F. Nanomechanics of lipid bilayers by force spectroscopy with AFM: A perspective. *Biochim. Biophys. Acta BBA - Biomembr.* **1798**, 741–749 (2010).

35. Janshoff, A. & Steinem, C. Mechanics of lipid bilayers: What do we learn from pore-spanning membranes? *Biochim. Biophys. Acta BBA - Mol. Cell Res.* **1853**, 2977–2983 (2015).

36. Chiantia, S., Ries, J., Kahya, N. & Schwille, P. Combined AFM and Two-Focus SFCS Study of Raft-Exhibiting Model Membranes. *ChemPhysChem* **7**, 2409–2418 (2006).

37. Sullan, R. M. A., Li, J. K., Hao, C., Walker, G. C. & Zou, S. Cholesterol-Dependent Nanomechanical Stability of Phase-Segregated Multicomponent Lipid Bilayers. *Biophys. J.* **99**, 507–516 (2010).

38. Komaragiri, U., Begley, M. R. & Simmonds, J. G. The Mechanical Response of Freestanding Circular Elastic Films Under Point and Pressure Loads. *J. Appl. Mech.* **72**, 203–212 (2005).

39. Kocun, M. *et al.* Viscoelasticity of pore -spanning polymer membranes derived from giant polymersomes. *Soft Matter* **6**, 2508–2516 (2010).

40. Zhang, R., Koutsos, V. & Cheung, R. Elastic properties of suspended multilayer WSe2. *Appl. Phys. Lett.* **108**, 042104 (2016).

41. Wang, Y. *et al.* Thermomechanical Response of Self-Assembled Nanoparticle Membranes. *ACS Nano* **11**, 8026–8033 (2017).

42. Konarev, P. V., Gruzinov, A. Yu., Mertens, H. D. T. & Svergun, D. I. Restoring structural parameters of lipid mixtures from small-angle X-ray scattering data. *J. Appl. Crystallogr.* **54**, 169–179 (2021).

43. Lolicato, F. *et al.* Cholesterol promotes clustering of PI(4,5)P2 driving unconventional secretion of FGF2. *J. Cell Biol.* **221**, e202106123 (2022).

44. Wan, K.-T., Guo, S. & Dillard, D. A. A theoretical and numerical study of a thin clamped circular film under an external load in the presence of a tensile residual stress. *Thin Solid Films* **425**, 150–162 (2003).

45. Saeedimasine, M., Montanino, A., Kleiven, S. & Villa, A. Role of lipid composition on the structural and mechanical features of axonal membranes: a molecular simulation study. *Sci. Rep.* **9**, 8000 (2019).

46. Schäfer, E., Vache, M., Kliesch, T.-T. & Janshoff, A. Mechanical response of adherent giant liposomes to indentation with a conical AFM-tip. *Soft Matter* **11**, 4487–4495 (2015).

47. Piontek, M. C., Lira, R. B. & Roos, W. H. Active probing of the mechanical properties of biological and synthetic vesicles. *Biochim. Biophys. Acta BBA - Gen. Subj.* **1865**, 129486 (2021).

48. Terzi, M. M., Deserno, M. & Nagle, J. F. Mechanical properties of lipid bilayers: a note on the Poisson ratio. *Soft Matter* **15**, 9085–9092 (2019).

49. Et-Thakafy, O. *et al.* Mechanical Properties of Membranes Composed of Gel-Phase or Fluid-Phase Phospholipids Probed on Liposomes by Atomic Force Spectroscopy. *Langmuir* **33**, 5117–5126 (2017).

50. Takei, T. *et al.* Measurement of membrane tension of free standing lipid bilayers via laser-induced surface deformation spectroscopy. *Soft Matter* **11**, 8641–8647 (2015).

51. van den Brink-van der Laan, E., Antoinette Killian, J. & de Kruijff, B. Nonbilayer lipids affect peripheral and integral membrane proteins via changes in the lateral pressure profile. *Biochim. Biophys. Acta BBA - Biomembr.* **1666**, 275–288 (2004).

52. Kuhlmann, J. W., Mey, I. P. & Steinem, C. Modulating the Lateral Tension of Solvent-Free Pore-Spanning Membranes. *Langmuir* **30**, 8186–8192 (2014).

53. Lipowsky, R. *et al.* Droplets, bubbles, and vesicles at chemically structured surfaces. *J. Phys. Condens. Matter* **17**, S537 (2005).

54. Temmerman, K. *et al.* A Direct Role for Phosphatidylinositol-4,5-bisphosphate in Unconventional Secretion of Fibroblast Growth Factor 2. *Traffic* **9**, 1204–1217 (2008).

55. Mechanical Properties of Giant Liposomes Compressed between Two Parallel Plates: Impact of Artificial Actin Shells | Langmuir. https://pubs.acs.org/doi/10.1021/la401969t.

56. Weiss, M. *et al.* Sequential bottom-up assembly of mechanically stabilized synthetic cells by microfluidics. *Nat. Mater.* **17**, 89–96 (2018).

57. Gonçalves, R. P. *et al.* Two-chamber AFM: probing membrane proteins separating two aqueous compartments. *Nat. Methods* **3**, 1007–1012 (2006).